DEVELOPMENT OF AN INTELLIGENT LI-ION BATTERY MANAGEMENT SYSTEM FOR ELECTRIC VEHICLES

DU JIANI

School of Electrical and Electronic Engineering

A thesis submitted to the Nanyang Technological University
in partial fulfilment of the requirement for the degree of
Doctor of Philosophy

2016

Acknowledgments

First and foremost, I would like to express my deepest appreciation to my supervisor, Prof. Wang Youyi for his constant guidance and invaluable advice on my research. Throughout my Ph.D. work, he always provided insightful thought that contributed a lot to this work. He always gave me encouragement when I encountered difficulties. I am really grateful to all his directions and encouragement.

I would also like to thank my co-supervisor, Prof. Wen Changyun for his invaluable directions, discussions and encouragement. His advice, collaboration and encouragement also contributed a lot to this work.

I would like to thank School of Electrical and Electronic Engineering, Nanyang Technological University for the supports on my Ph.D. project. I also want to thank the staff of Electric Power Research Lab and Power Electronics Research lab for their kind support.

I greatly appreciate Dr. Liu Zhitao for his advice and discussions, which contributed a lot to the development of this work. I would like to thank Xian Liang for his advice and help. I would also like to thank Dr. Wu Si for his encouragement and suggestions on my work.

I am grateful to all the colleagues in Electric Power Research Lab. Many thanks to Xia Nan, Li Mengting, Tang Difei, Jiang Hao and many other friends for their friendship, support and kind help to me during my Ph.D. candidature.

Finally, I would like to express my deepest love and appreciation to my family. I am so grateful to my parents, Du Binsheng and Wang Shaomin, and my grandmother, Fan Miao, for their constant encouragement and deep love to me. I would also like to thank my other family members for their support.

Table of Contents

Summary

To improve electric vehicle (EV)'s operation performance and reliability, an energy management system (EMS) should be designed to supervise and control the power sources including lithium-ion (Li-ion) batteries. In this thesis, some topics relevant to implementation of a new intelligent EMS for EVs and focusing on Li-ion battery's operation and performance are researched. The intelligent EMS is based on some novel methods for modeling and estimation of Li-ion batteries, cell equalization in battery pack and power management strategy design for the power sources in EVs.

The first part of this thesis focuses on Li-ion battery modeling. Various types of equivalent circuit model are established and compared. It is verified that the series circuit model with two resistor-capacitor (RC) networks has good performance. The model using fuzzy logic to describe the temperature effect based on experiments is proposed. Then, another new type of battery model trained by the extreme learning machine (ELM) algorithm is proposed in experimental condition with simple current patterns. The ELM model performs simpler modeling process and better accuracy comparing with existing radial basis function (RBF) neural network (NN) battery model.

Based on existing and proposed models, Li-ion battery state of charge (SOC) estimation is researched and improved in this thesis. The Kalman filter (KF)-based methods including extended Kalman filter (EKF), unscented Kalman filter (UKF), adaptive EKF (AEKF) and adaptive UKF (AUKF) are applied on the ELM model. Experimental results and comparisons indicate that the AUKF algorithm achieves improved SOC estimation performance with better accuracy and faster convergence rate. The estimation results also verify that the ELM model is more suitable for SOC estimation than the conventional RBF NN model.

Considering the battery model's flexibility, accuracy and practical operation conditions, the particle filter (PF) methods are applied on an accurate nonlinear Li-ion battery equivalent circuit model. The model represents the circuit parameters' variation according to SOC by nonlinear functions and achieves better accuracy than constant parameter circuit models. The algorithms of PF and unscented particle filter (UPF) for nonlinear systems are executed to estimate Li-ion battery SOC. The estimation results reveal that

UPF has better accuracy and faster convergence rate than PF. However, the computational load for the PF methods is heavier, bringing limitations in EMS's applications.

Then, the accurate nonlinear equivalent circuit model is simplified to a constant circuit parameter model with system uncertainties to achieve simpler modeling and estimation process. The sliding mode observer with high accuracy and light computation is applied. The adaptive gain technique is used in the observer and SOC estimation with good performance is provided by this proposed adaptive observer. The adaptive observer based on sliding mode scheme is also applied to estimate Li-ion battery SOC and state of health (SOH) simultaneously. The estimation results verify that the proposed observer scheme has accurate and robust performance on battery SOC and SOH estimation.

Another part in this thesis is about cell equalization in Li-ion battery packs. Since cell imbalance brings damage to Li-ion batteries in the pack, considering circuit size, system implementation and cost, the equalization method using switched capacitors is applied and improved for series battery strings in battery pack in this thesis. The proposed modularized cell equalization schematic using chain structure switched capacitors achieves fast equalizing speed and small voltage across the switches. Another modularized double switched capacitor equalization schematic considering battery SOC and SOH is also proposed to improve the equalizing efficiency and reliability. The trade-off between equalization speed and system simplicity should be considered to select the appropriate equalization schematic in applications.

The last part of this thesis designs the power management strategy in EMS for EVs. Fuzzy logic control strategy is proposed and Li-ion battery's aging levels represented by SOH is considered in the control system. By designing fuzzy rules, the fuzzy control strategy realizes the functions of EV power distribution and power sources operation supervision for various EV driving actions. Specifically, Li-ion battery life is extended by the designed fuzzy control strategy considering SOH. To summarize, the proposed power management strategy in EMS for EVs achieves good performance on EV power sources operation, supervision and Li-ion battery service life extension.

List of Figures

List of Tables

Nomenclature

AEKF	adaptive extended Kalman filter
AUKF	adaptive unscented Kalman filter
BOL	beginning-of-life
BP	back propagation
DOD	depth of discharge
EKF	extended Kalman filter
ELM	extreme learning machine
EMS	energy management system
EOL	end-of-life
EV	electric vehicle
KF	Kalman filter
Li-ion	lithium-ion
NN	neural network
OCV	open circuit voltage
OS-ELM	online sequential extreme learning machine
PF	particle filter
RBF NN	radial basis function neural network
RC	resistor-capacitor
RMSE	root mean squared error
SOC	state of charge
SOH	state of health
UDDS	urban dynamometer driving schedule
UKF	unscented Kalman filter
UPF	unscented particle filter

Chapter 1 Introduction and Literature Review

1.1 Motivation

With the world's energy crisis and heavier environmental pollution of greenhouse gas emission from traditional fossil-fuel vehicles, the development for vehicles with electrical energy is considered as a possible solution [1]. Electric vehicle (EV) has the advantages of no pollution and high energy efficiency, which meets today's demand for vehicles. Thus, EV attracts more and more attention and is developing rapidly. However, there are still some problems unsolved in EVs. One of the most important issues is to realize and improve the EV power supply's status supervision, prediction, operation control and protection. EV would encounter its bottleneck if the power sources operation status are not supervised and controlled appropriately. Improving the power source's reliability and safety is also the focal point to be researched. Thus, to implement an intelligent energy management system (EMS) in EVs is necessary. EMS performs the functions of supervising and controlling energy storage and power distribution for all the sources in EVs. An intelligent EMS can achieve the objectives of obtaining maximum energy efficiency, providing required power for different vehicle driving conditions, supervising and predicting the sources operation status by estimating the power source's inner states, and extending the source's life by protection measures. EMS's performance is important because it influences EV's performance significantly [1]. A well-designed EMS improves EV's reliability and practicability.

As the device converts stored chemical energy into electric energy, battery has been adopted as the power supply for EVs. Since a lithium-ion (Li-ion) battery has the advantages of high energy density, light weight, low self-discharging rate and long cycle life [2, 3], it outperforms other types of batteries and has been widely used in EVs. A Li-ion battery meets the specific operational and environmental demands for EV's power devices. However, there are still some limitations in Li-ion battery development in EV applications, which is one of the motivations in this research. Exploration of enhancements for Li-ion battery performance supervision based on battery inner state estimation and battery use life extension in EVs is still needed in EMS. Besides, as a power supply, Li-ion batteries constitute battery pack by series and parallel connecting

structures and the batteries in the pack should be controlled for reliable and efficient operations [4]. In general, EV's performance and EMS implementation have resulted in the development of Li-ion battery estimation and battery behavior control, including the key functions of state of charge (SOC) and state of health (SOH) estimation [5] and cell equalization in the battery pack.

The issues on Li-ion battery SOC and SOH estimation have been attracting researchers' attention recently. As an EV's power device, each battery needs accurate SOC and SOH knowledge to avoid the phenomenon of over-charging, over-discharging and over-rapid aging. However, Li-ion battery has nonlinear characteristics and complex dynamic behavior, bringing difficulty to the estimation process. On the other hand, various existing cell equalization methods carried out in the Li-ion battery pack have led to complex circuit topology, high component voltage and high cost, which also need more research and enhancement.

A Li-ion battery pack plays a major part in the EV's power supply system. Besides, EVs also need some assistant power devices to compensate high-frequency fluctuating variation of the required power during EV driving. Then, to design a power management strategy to realize power distribution between supply sources and source operation status supervision is another significant topic in EMS. Especially, Li-ion battery life extension could be realized by designing intelligent control strategies.

The motivation of this research is to design an intelligent EMS in EVs. The designed EMS will be able to improve EV's power supply system operation performance and reliability by supervising, predicting, controlling the Li-ion battery and pack operation and distributing and controlling the EV power between the Li-ion battery pack and other power sources.

1.2 Literature Review

A comprehensive review on relevant topics in EMS studied in this research is done in this section.

1.2.1 Li-ion Battery Modeling

Since EMS needs accurate Li-ion battery status as the basis to supervision, Li-ion battery modeling is the fundamental step when acquiring battery knowledge. For any closed-loop online estimation algorithm to obtain battery state, it is necessary to establish the battery model at first. With an accurate and proper battery model, the battery operation performance including charging and discharging behaviors can be simulated and predicted. Usually, a single battery is taken to obtain the model since such a model can reflect the battery's dynamics accurately. The Li-ion battery's inner electrochemical reaction is very complex and it is a complicated system with nonlinear behavior. So the process of battery modeling would not be simple. There are mainly three kinds of models for Li-ion battery: electrochemical model, equivalent circuit model, and black box model [6-9].

The electrochemical model [10-12] focuses on the battery's inner chemical reaction and predicts the spatially distributed behavior of the essential states of the battery [13]. This kind of model is the most accurate for Li-ion battery. However, the electrochemical model is described by partial differential equations, which is difficult for calculation and estimation. It may even be not applicable in real-time application [14]. This kind of model is mostly used to optimize physical design process and test the battery's chemical characteristics.

The equivalent circuit model for Li-ion batteries is commonly used for control and prediction [6, 9, 15, 16]. Impedance testing has verified that equivalent circuit models have a meaningful description for Li-ion batteries. When providing battery knowledge to EMS, the equivalent circuit model is much easier than electrochemical model. The equivalent circuit model simulates Li-ion battery characteristics by using particular circuit's behavior. The equivalent circuit model is easy to comprehend and appropriate for different current patterns. Represented by mathematical equations derived from electric circuit theory, this kind of model can reduce computation load and needs simpler estimation algorithm compared with the electrochemical model. In [9], different Li-ion battery equivalent circuit models are proposed, analyzed and compared.

The equivalent circuit models are established by external reflection of the battery directly, using the battery's measured voltage and current. Such kind of models can be very

accurate to describe Li-ion battery's dynamics. The circuit model components are changing to some affecting factors, such as SOC and SOH. If the circuit parameters are obtained at different conditions and represented by nonlinear functions, the model accuracy will be improved significantly, whereas complicated equations and strong nonlinearity will be brought to the model expressions. In [17], the parameters are set as functions of SOC determined by curve fitting, resulting in a model with complex equations. If the estimation process's simplicity is considered, some changes may be executed on the Li-ion battery model, sacrificing its accuracy to some extent. In [18], the parameter variations influenced by affecting factors are represented by bounded uncertainties, making the model equations simple although the accuracy is reduced.

Most Li-ion battery equivalent circuit models are discussed at specific temperature. However, the ambient temperature also has obvious effect on Li-ion battery's characteristics [19-21]. Recently, some researchers begin to describe this effect on the Li-ion battery's equivalent circuit model. In [19], the temperature effect on model parameters is tested and described by simple interpolation algorithm. In [20], the model parameters are represented by nonlinear functions of SOC and temperature. However, the model parameters are complex with the functions of two variables.

In experimental condition with simple current pattern, neural networks (NNs) can be applied to model Li-ion batteries with a higher accuracy. Recently, NNs have also been widely applied to battery modeling. NNs can approximate complex nonlinear mappings directly from the system input-output samples without knowledge of the inner structure. Thus, the NN battery model provides a black-box model without the need to know the battery's inner structure and electrochemical reactions. The application of NNs brings significant convenience and accuracy improvement to the battery modeling process. No manual step is needed after network initialization. The pre-designed NN learning algorithm will provide the mapping results with its highest accuracy. The battery model trained by NN describes the relationships between battery current, voltage and other variables. Reference [22] uses typical back propagation (BP) NN to approximate the relationships between battery variables. In [23-26], the Li-ion battery model is trained by radial basis function (RBF) NN and the relationships between battery state variables are approximated. As the proposed model based on BP network, RBF NN has better learning

ability, convergence property and mapping rate compared with the traditional BP NN [27]. In [28], a battery model using fuzzy logic combining NN is established, although the model has a complex structure and the parameters are adjusted during learning. The NN model has simpler modeling steps than the equivalent circuit model for Li-ion batteries. However, traditional NNs still have the flaws of heavy computation and inefficient learning process. The extreme learning machine (ELM) algorithm is proposed to overcome these flaws. ELM is firstly introduced in [29] and it gives a fast learning process. This new kind of learning algorithm could be applied to train the model for Li-ion batteries.

For different types of Li-ion battery models, the acceptable accuracy is around 1% to 5% error [17]. Since the SOC range for Li-ion battery operation in EVs is commonly larger than 20%, the model error in low SOC range could be less focused. When establishing and selecting the suitable model for Li-ion batteries, the model simplicity should also be considered because a complex model is difficult to control and estimate. Thus, the modeling process for Li-ion battery will be a trade-off between the battery model's accuracy and simplicity.

1.2.2 SOC Estimation

Since over-charging and over-discharging bring inevitable damage to Li-ion battery, the battery's inner charge must be estimated accurately to avoid such a phenomenon and ensure safe operation. An important variable describing the Li-ion battery's status is SOC [3]. SOC indicates the battery's available energy. Therefore, EMS's control and supervision on Li-ion batteries is based on the SOC knowledge. Accurate SOC estimation should be provided by EMS [30].

SOC is defined the ratio of the battery's remaining capacity to the nominal capacity [15]. It indicates the battery's storage charge. By the definition of SOC, its equation is given by:

$$SOC(t) = SOC(t_0) - \int_{t_0}^{t} \frac{I(\tau)}{C_n} d\tau \tag{1.1}$$

where $SOC(t_0)$ represents the battery initial SOC; C_n represents the battery nominal capacity; and I is the battery current defined positive for discharging and negative for

charging. For the discharging process, a constant discharging efficiency factor is often applied in the integral part. Here, this factor is assumed as 1. Sometimes, the equation is transformed to the discrete form as:

$$SOC(k+1) = SOC(k) - \frac{\Delta t}{C_n} I(k) \tag{1.2}$$

where k is the sampling point; and Δt is the sampling interval. When doing estimation on battery, SOC is often taken as one state variable for the system state-space equations of the battery model with above descriptions.

To obtain accurate SOC estimation for Li-ion battery, various methods have been proposed. Reference [31] summarizes these SOC estimation methods. The most widely used technique for SOC estimation is Coulomb counting [32]. The principle of Coulomb counting is to treat the battery as a capacitor and obtain its storage energy by current integration directly. Nevertheless, estimation error may be accumulated for this open-loop algorithm, resulting in the estimate drifting away from the true value. Any initial SOC error also causes a bias in the estimation. Another commonly used technique is the open-circuit-voltage (OCV) method. This method computes SOC from Li-ion battery's OCV-SOC relationship represented by the OCV curve [33]. However, accurate OCV measurement requires the battery to be in the equilibrium state, whereas the batteries in EVs are mostly at work during driving. Therefore, the OCV method is not suitable for real-time SOC estimation [31]. The above methods have simple theories and are easy to implement. Big errors may be caused by noise or improper measuring condition.

The impedance spectroscopy technique measures the battery's impedance by testing the voltage response with a small AC current applied to the battery [34]. A spectroscopy is composed of the impedance data extracted from different frequency currents. This method can provide accurate SOC values. But it needs specific measurement and is not appropriate in EVs. In [35], the intelligent method of fuzzy logic is combined with impedance spectroscopy to achieve better SOC estimation results. This method provides good estimation results, but it needs specific experiments so it is not suitable for applications in EVs.

State estimation can lead to filtering algorithms. Kalman filter (KF) is a mathematical technique that provides an efficient recursive means for estimating the states of a process by minimizing the mean of the squared error [36, 37]. It is a powerful method to use measurements containing noise to do online state estimation. This technique is based on existing battery models. The KF-based algorithms are widely applied for SOC estimation [32, 38, 39]. Since the Li-ion battery SOC has a nonlinear relationship with other variables [40], in [28, 41, 42], some improved nonlinear KF versions are applied to estimate SOC with accuracy and robustness. The most commonly-used nonlinear version of KF, extended Kalman filter (EKF), is applied to estimate the battery SOC in [19, 39, 43-46]. The essence of EKF is to linearize the system at each time step to approximate the nonlinear system with a linear time varying system. Reference [47] proposes a series of EKF with linear combination based on linear local model networks (LMNs) whereas it is difficult for LMNs to contain all the working conditions. However, EKF is only applicable when the model is precise or has a suitable form. For the system with more obvious nonlinearity, EKF's linearization step would bring large estimation error or even divergence. In this way, the unscented Kalman filter (UKF) which is more suitable for nonlinear systems is also applied to do SOC estimation in [36, 48]. UKF does not linearize the system and achieves a higher order of accuracy in estimating the mean and error covariance of the state vector [36, 48]. Based on EKF and UKF, adaptive Kalman filter has been applied in battery estimation to achieve better results [49, 50]. Compared with EKF, adaptive EKF (AEKF) has better performance [51]. A much better estimation performance can be achieved for nonlinear systems by adjusting the noise covariance matrices by adaptive Kalman filter [52, 53].

However, the estimation performance of KF variants is still dependent on the model's nonlinearity and accuracy. To estimate the system with severe nonlinearity remains a problem. Sometimes EMS demands the battery model to be accurate, resulting in strong system nonlinearity. Then the KF-based methods may not supply satisfying estimation results. In addition, KF variants' statistical property demand for the system noises may also be in conflict with practical EV driving conditions. In [54], an adaptive Luenberger observer is used to do estimation on a linear battery model without any assumption about the system noise characteristics, but the Li-ion battery's nonlinearity is not reflected for

this method. An H_∞ observer is applied to estimate battery SOC despite the system noise statistical property in [55] under the working condition with unknown errors. However, the H_∞ observer is based on linear matrix inequality (LMI) solving and may be not applicable in practice for the need of sufficient condition. Moreover, both methods in [54] and [55] calculate SOC from OCV estimation, which may lack reliability because a small OCV error leads to a large SOC error.

As another strategy for filtering other than KF variants, particle filter (PF) has been applied in navigation, object tracking and communication. PF is based on sequential Monte Carlo methods and it can deal with any nonlinearities or distributions [56], including system with severe nonlinearity and non-Gaussian distribution noises. Thus, PF could compensate the KF methods' defects. In [57], PF is applied on nonlinear battery models for SOC estimation. The performance of PF can be improved by including new observation information when generating proposal distribution. The unscented particle filter (UPF) which uses UKF to update each particle with new measurement is applied on high-power Li-ion batteries using simple voltage expression in [58].

Recently, the sliding mode observer is also applied as a reliable and robust tool for battery SOC estimation on the models representing the nonlinear part as uncertainties [18, 59-61]. The sliding mode observer has robust tracking performance to the *a priori* knowledge of the system noise and simple structure with light computation load [62], which is suitable to Li-ion battery systems with presence of modeling errors, measurement noises and uncertainties [59]. The sliding mode technique is a robust method for handling uncertainty in system [63-65]. The system will be forced to move along a predefined manifold named sliding surface and remain on it thereafter. The observer based on sliding mode concepts is firstly proposed in [63]. This kind of observers has high accuracy, simplicity and robustness to handle system uncertainty and noise efficiently during estimation. By compensating the model uncertainties, the demand for model precision can be reduced. The sliding mode observer using equivalent control method is proposed and developed in [63, 66]. When the sliding surface is reached, the equivalent control method can obtain some unknown system quantities [63, 66]. Since to determine the appropriate switching gain for the system may be not easy, an adaptive gain scheme is applied in the sliding

mode observer recently. The switching gain is adjusted by adaptive laws according to the tracking errors. In [67], an adaptive gain observer combined with the sliding mode method is proposed.

1.2.3 SOH Estimation

In EVs, the Li-ion battery is charged and discharged for multiple cycles. The phenomenon of battery aging occurs and deepens gradually with battery usage because of the reactions and material consumption inside it. The lifespan of the Li-ion battery is a limitation for EVs. In [68, 69], Li-ion battery's aging mechanism is studied and the affecting factors on battery degradation are proposed and tested. Both the calendar and cycle effect on the Li-ion battery life is studied in [70]. Li-ion battery's degradation performance expressed by capacity fade modeling is also studied in [71-74]. Some studies emphasize battery inner reactions or design complex testing process in experiments, obtaining a complex degradation model that is hard to understand and not applicable. In [75-78], Li-ion battery degradation mechanism considering practical vehicle utilization is constructed. A new concept of total Ah-throughput is proposed and the aging effect from any cycle is transformed to the nominal cycle with a predefined factor that describes the battery aging progress. This battery aging model is easy to comprehend and applicable in practice.

The Li-ion battery's aging level could be represented by SOH. SOH is defined as the performance of the battery compared to its past and expected future. Hence, it reflects Li-ion battery's performance relative to its fresh condition and could predict the battery's future operations [79]. Li-ion battery's operation status is relevant to its SOH and its life time can be indicated from SOH.

As the important variable indicating Li-ion battery status, SOH also needs estimation like SOC. Although battery aging models have been proposed in various studies stated above, they are relevant to many factors with complex relationships, which is difficult to estimate. In this way, SOH is often indicated by Li-ion battery parameter variation, including capacity reduction and an inner resistance increase.

The internal resistance is used to compute the Li-ion battery SOH as proposed in [59, 79-82]. Reference [83] identifies Li-ion battery's aging parameters in the electrochemical model, which provides the theory basis for using resistance to compute SOH. Estimating

SOH by impedance measurement combining with fuzzy logic is proposed in [84, 85]. NNs are also taken to train the battery aging mechanism by the data from battery life cycle tests and SOH is estimated from the trained model in [86]. However, these intelligent techniques depend on numerous long-time experiments and large data training sets. An enhanced method based on the Coulomb counting technique is proposed to estimate Li-ion battery SOC and SOH in [87]. The charging and discharging efficiencies are considered and SOH is determined by the maximum releasable capacity, whereas this method is not suitable for online work. Reference [79] applies the adaptive control approach to estimate battery OCV and internal resistance to compute SOC and SOH, whereas the convergence performance is not satisfying. In [59], the adaptive law for SOH estimation is established based on a battery model with uncertainty and nonlinearity. The estimation error converges to zero. However, the resistance variation is not considered in this method.

The KF methods are also executed to estimate SOH. In [37], AEKF is used to estimate SOC and the battery parameters as a joint estimation approach. However, the system state vector is augmented by the parameters with high dimension [88]. Large matrix operation is taken and the computation load is increased. The dual Kalman filter method using separate filters for state and parameter estimation is a better approach applied to Li-ion battery estimation. In [42-44, 80, 89, 90], dual nonlinear Kalman filters are operated to estimate battery SOC and SOH simultaneously in real time. In [80], the dual EKF algorithm is combined with pattern recognition whereas it is difficult for the testing conditions to include all kinds of electrochemical characteristics in the battery.

Although widely used and easy to implement, dual nonlinear KF methods still encounter the problems of model error, model nonlinearity and system noise as conventional KF variants do. In [91], a dual sliding mode observer scheme is applied on a simple circuit model to estimate battery SOC and SOH simultaneously. The proposed observer deals with system's nonlinearity and modeling error by the function of the sliding mode observer. Meanwhile, the dual estimator scheme's simplicity and usability is retained.

1.2.4 Cell Equalization

To provide sufficient power and energy to EVs, Li-ion batteries must make up a battery pack by connecting batteries in series and parallel. In battery pack, each single battery is named a cell. In a series-connected battery stack, the charging and discharging currents are the same for cells. However, individual cells may have manufacturing variance in the internal resistance, capacity or other parameters, leading to different voltages and SOC during operation. Specifically, individual cell voltages will drift apart overtime [92]. If the differences grow bigger, the capacity of the total pack would be decreased, or even cell damage would occur. So the cell imbalance phenomenon must be avoided in a battery pack. Some equalization measures should be taken.

To achieve cell equalization, there are mainly two ways: passive and active equalization schematics [93-96]. The passive equalization schematic uses resistors connected with cells in parallel and discharges a higher-energy cell onto corresponding resistor. Such a method is not efficient because of energy waste. The active cell equalization schematic uses unconsuming energy elements such as capacitor or inductor as the energy storage and transfer devices. So energy will be transferred from a higher-energy cell to a lower-energy cell and the energy efficiency will be improved [97].

In [94], a review on Li-ion battery cell equalization using switched capacitors, inductors and transformers in EV applications is proposed. In [92], various cell equalization methods are established and compared via Matlab simulation. In [98], the topology using switched inductors is implemented. To improve the equalization speed, single-winding transformers and multi-winding transformers are used in [99, 100]. However, the application of transformer leads to high cost and magnetic loss.

Another widely-used method for cell equalization is the application of equalization converter. In [101, 102], a buck-boost converter is used as the equalization circuit with higher energy efficiency and less circuit losses. In [93], a bidirectional DC/DC converter with an energy transferring capacitor based on fuzzy logic control is proposed. However, the equalization converter significantly increases the circuit size, complexity, and implementation cost. The control strategy in the converter also increases the computation load of the whole system.

In [103], the equalization schematic using switched capacitors is proposed. Both the equalization circuit and control method are simple. To overcome conventional switched capacitor's slow equalization speed, the switched capacitor circuits with chain structure [104], and double layer structure [105] are proposed to achieve faster equalization recently. Reference [106] interprets the topology combined double-tiered switched capacitors with chain structure, which has the advantages of the two schematics and achieves a short equalization time. Nevertheless, more capacitors and switches are designed in the circuit, which improves the cost and circuit complexity. A shortcoming for switched capacitor is that the current flow is driven under cell voltage difference during the equalization process. In this way, researchers add SOC estimation into switched capacitor equalization system to select the right cells to be charged or discharged. In [107], a single switched capacitor equalization schematic is applied based on cell SOC estimation results from EKF. However, the capacitor is in parallel with the whole string or single cell, which leads to large voltage difference during equalization steps and it may cause large current impulse to individual cells.

Battery modularization is often applied in battery packs. With the modularization concept, the battery pack is divided into several modules so that each module could be treated with a separate equalization schematic [92, 108, 109]. Then, another higher-level equalization topology can be constructed to realize module equalization. The modularized equalization schematic improves the equalization speed inside one module and reduces the equalizing components' voltage and current stress [92].

1.2.5 Power Management Strategy

Although designed as the major energy source, the Li-ion battery pack could not supply all the required power during EV driving. The Li-ion battery is not suitable for drastically varying current applications for some driving actions. For example, EV's acceleration may bring an abrupt large current pulse that is harmful to the Li-ion battery. Besides, when achieving EV regenerative braking, the instantaneous regenerative braking current will be injected into the batteries and may cause the battery voltage to increase suddenly, even exceeding the electrolyte breakdown threshold voltage [94]. Thus, to protect the Li-ion battery pack and improve energy efficiency, some other power sources enduring the

drastic power variation are needed in the EV's power supply system. Mostly, the ultracapacitor is designed as the source for abrupt varying power in EVs.

With the Li-ion battery pack and ultracapacitors designed as the power sources, the method to determine the contributed power of each source is needed. Besides, to improve the power supply system's performance and protect the devices, both the Li-ion battery pack and ultracapacitors should operate in their optimal operation regions. Hence, the power management strategy that distributes the source's contribution power and supervises the source's operation points is indispensable for EMS in EVs.

The optimal control method is used to do energy management in [110]. Considering battery operation constraints, the control system optimizes the usage of battery. However, the *a priori* knowledge of the power profile is required for this optimization-based technique [111].

Intelligent control strategy can achieve the objectives of power management for their intuition and comprehensiveness. According to the nonlinear behavior of the Li-ion battery pack and the complexity for the whole system, a fuzzy logic control strategy is suitable to achieve the functions of power distribution and source supervision. In [112], an EMS in EVs using fuzzy logic supervisory strategy is proposed and tested. The fuzzy rules adjusting system power allocation are designed according to the power source's characteristics and experience. High dynamic performance is achieved for each source with the proposed strategy, although the battery aging phenomenon is not considered. Reference [113] applies similar fuzzy control structure and strategy with different rules for EV's practical driving cycles. Considering the power exchange between power sources in system, a multi-mode power allocator using fuzzy logic in an energy storage system is proposed in [114]. The control strategy determines power allocation as well as the power exchange between the Li-ion battery pack and ultracapacitor pack. Thus, the power sources not only supply or absorb power from external system, but also transfer power to each other according to their status. The Li-ion battery aging phenomenon is considered in [114]. However, it is not considered in the fuzzy control strategy.

1.3 Objectives and Contributions of This Thesis

In this thesis, an intelligent EMS in EVs is developed by implementing and improving the research on topics focusing on the Li-ion battery. In EMS, it is necessary to propose simpler and more accurate battery model. Moreover, innovations should be taken to obtain better battery estimation. The estimation algorithm should be designed to have good accuracy and robustness, but not with heavy computation. The EMS also needs efficient cell equalization schematic with a simple circuit and control method. At last, considering the Li-ion battery's aging phenomenon, it is necessary to design and improve the power management strategy in EMS that not only making the power sources operate with good performance but also extending Li-ion battery's service life in EVs.

The major contributions of this research are as follows:

(1) The new Li-ion battery model considering temperature effect is developed. An innovative method using fuzzy logic to consider the affecting factors of Li-ion battery model is proposed. A new Li-ion battery model is trained by the ELM algorithm for a simple current type in experimental condition, achieving intuitive and faster modeling process.

(2) Li-ion battery SOC estimation performance is improved with better accuracy and robustness by applying the adaptive UKF (AUKF) algorithm based on the ELM model.

(3) Apply the UPF algorithm to estimate Li-ion battery SOC estimation for an accurate nonlinear equivalent circuit model, overcoming the KF method's defect.

(4) Li-ion battery SOC and SOH estimation is realized simultaneously using an adaptive observer based on the sliding mode scheme for a battery equivalent circuit model with uncertainties. The proposed estimation algorithm achieves a simpler model, a simpler estimator design process and lighter computation with good estimation accuracy and robustness.

(5) A simple cell equalization topology and a control method using switched capacitors by modules are designed. Compared with conventional techniques, Li-ion battery SOC and SOH are considered and the equalization schematic efficiency and reliability is improved.

(6) An intelligent power management strategy using fuzzy control is proposed. The power management strategy performs the EMS's supervision and control function for EV's power sources and realizes Li-ion battery life extension by considering the Li-ion battery aging phenomenon.

1.4 Organization of This Thesis

In Chapter 1, the motivation of this research is proposed and literatures in relevant areas are reviewed. The objectives and contributions of this thesis are also introduced.

Chapter 2 describes Li-ion battery models and proposes new battery models. The equivalent circuit model is investigated. The equivalent circuit model with two RC networks is established based on battery experiments. An equivalent circuit model describing temperature effect by fuzzy rules is also proposed from experiments. Then, the model trained by specific learning algorithms for simple current pattern is researched. The model trained by ELM with a simpler training process and a higher accuracy is proposed. Experimental verification indicates that the ELM model outperforms the model trained by RBF NN. Li-ion battery modeling is the basis for state estimation and system dynamic behavior simulation in later chapters.

In Chapter 3, the SOC estimation is done based on the proposed ELM model in experimental condition and good estimation results are given by AUKF. The estimation algorithms including EKF, UKF, AEKF and AUKF are applied to estimate SOC. With better performance in nonlinear system and noise adjustment techniques, AUKF performs the best estimation tool including both good accuracy and robustness. Estimation results from the RBF NN model are also described as a comparison, which verifies that the proposed ELM model with the AUKF estimation technique improves the SOC estimation performance.

In Chapter 4, an accurate Li-ion battery equivalent circuit model suitable for complex current pattern considering SOC effect on model parameters is established. The PF algorithm that adapts to nonlinear system and non Gaussian distribution noise is applied on the accurate model. The improved form of PF, i.e. the algorithm of UPF, is also applied to estimate SOC. The estimation results show that UPF gives accurate and convergent estimation for the nonlinear model with heavy computational load.

In Chapter 5, a novel adaptive observer based on sliding mode scheme is proposed to estimate the Li-ion battery SOC and SOH simultaneously. The battery equivalent circuit model is described by a simpler form with uncertainties. The sliding mode observer with adaptive gain is applied to estimate the Li-ion battery SOC, showing better accuracy than that of the sliding mode observer with constant gain. Then, the adaptive observer based on the sliding mode scheme is applied to do battery SOC and SOH estimation. Good SOC and SOH estimation results are provided, verifying the proposed estimation algorithm's performance.

Chapter 6 presents cell equalization schematics in battery packs. The switched capacitor method with simple circuit and control signal is studied and improved. A modularized chain structure switched capacitor equalization method is proposed. The equalization speed is effectively improved and the voltage across the equalization components is reduced. The modularized double switched capacitor equalization method is also proposed. Cell SOC and SOH are considered for this method, improving the equalization system's reliability.

Chapter 7 establishes a novel power management strategy using fuzzy logic control. The system applies the Li-ion battery model with description of the Li-ion battery's aging mechanism. The Li-ion battery aging progress is modeled and represented by SOH in the control strategy. The designed fuzzy logic control strategy distributes the system power and supervises power source's operation points using the controller inputs of Li-ion battery SOC, SOH and ultracapacitor SOC. Li-ion battery aging is considered directly in the system and the battery use life can be extended by the proposed strategy.

Chapter 8 gives the conclusions of this thesis. Some future works based on this research are recommended.

Chapter 2 Li-ion Battery Modeling

For lithium-ion (Li-ion) batteries, the equivalent circuit model and neural network (NN) model are commonly applied for estimation. In this chapter, the two kinds of Li-ion battery models are presented. Section 2.1 introduces the content of this chapter. In Section 2.2, various types of the equivalent circuit model for Li-ion batteries are established and compared. In Section 2.3, a fuzzy logic based model considering battery temperature effect is established. In Section 2.4, the extreme learning machine (ELM) algorithm is described and the ELM model is proposed. An online ELM model is also trained in this section. Section 2.5 gives the conclusion of this chapter.

2.1 Introduction

The knowledge of the battery model is important and indispensable in energy management system (EMS) for electric vehicles (EVs). Li-ion battery modeling is the elementary step to employ estimation algorithms and operation rules. As a nonlinear system with complex inner electrochemical reactions, a Li-ion battery needs a model that simulates its dynamic characteristics accurately.

In this chapter, various types of models for Li-ion batteries are investigated and established. First, the equivalent circuit model is studied. Both the series circuit model and parallel circuit model using constant circuit parameters are established from experiments and comparisons on these two kinds of models are done. The temperature effect on Li-ion battery characteristics is also considered and combined with the SOC effect in an equivalent circuit model to form a fuzzy logic based model. The temperature effect on model parameters is represented by fuzzy rules clearly and efficiently. From simulations and experiments it is verified that this new model has good accuracy and flexibility in the entire temperature range. Then, the temperature effect on Li-ion batteries is excluded in later chapters according to the experimental results on battery surface temperature. To achieve simpler and faster modeling process, the mathematical model for the Li-ion battery trained by NN learning algorithms is also researched and improved in this chapter. The ELM algorithm is applied to train the battery model. Compared with the existing RBF NN model, the ELM model gives better performance for Li-ion batteries. Besides, an

online trained battery model is provided to EMS by the algorithm of online sequential ELM (OS-ELM).

2.2 The Equivalent Circuit Model for Li-ion Batteries

As the commonly-used battery model, the equivalent circuit model is easy to comprehend and with good accuracy for different current patterns. The equivalent circuit model represents the battery characteristics by a circuit composed of a voltage source, resistors and capacitors. This kind of model can be represented by mathematical equations derived from electric circuit theory when doing control and estimation. There are various types of equivalent circuit models for Li-ion batteries [15]. In this section, several representative Li-ion battery models are established and compared.

2.2.1 Parallel Circuit Model

The parallel circuit model is proposed and applied to do state of charge (SOC) estimation in [18] and [54]. This kind of model is designed using the software of Advisor for simulating EVs. The model circuit has a parallel structure as shown in Fig. 2.1.

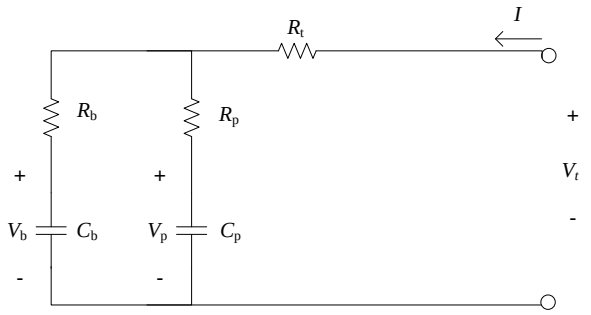

Fig. 2.1. The parallel circuit model for Li-ion batteries [54].

In Fig. 2.1, V_t represents the battery terminal voltage and I represents the current entering the battery. The capacitor C_b with large capacitance is the bulk capacitor that represents the battery capacity. All the other RC components are with small values and they describe the battery dynamic behaviors. Denote the voltage across the two capacitors as V_b and V_p. The model equations are derived as (2.1)-(2.3):

$$\dot{V}_b = -\frac{1}{C_b(R_b + R_p)}V_b + \frac{1}{C_b(R_b + R_p)}V_p + \frac{R_b}{C_b(R_b + R_p)}I \tag{2.1}$$

$$\dot{V}_p = \frac{1}{C_p(R_b + R_p)} V_b - \frac{1}{C_p(R_b + R_p)} V_p + \frac{R_b}{C_p(R_b + R_p)} I \tag{2.2}$$

$$\dot{V}_t = \frac{R_p}{(R_b + R_p)} V_b + \frac{R_b}{(R_b + R_p)} V_p + R_t I + \frac{R_b R_p}{(R_b + R_p)} I \tag{2.3}$$

The parallel circuit model has linear model equations. The model is simple to control and estimate. However, this kind of model does not perform good accuracy. In [54], the dynamic behavior of the parallel circuit model is not ideal compared with the battery's actual terminal voltage. A large model error occurs when current changes or SOC is small. To improve the model's dynamic behavior, the bulk capacitor C_b is replaced by a nonlinear voltage source dependent on SOC in [18], bringing nonlinearity to the model.

2.2.2 Series Circuit Model

Compared with the parallel circuit model, the series circuit model for Li-ion battery is more widely used for its better accuracy. A simple series circuit model is shown in Fig. 2.2. The voltage source simulates the open circuit voltage (OCV) that describes battery terminal voltage at the equilibrium state. For Li-ion batteries, OCV has a monotonic nonlinear relationship with SOC. R_s represents the battery's inner resistance. The model equation for the simple series circuit model is:

$$V_t = OCV + R_s I \tag{2.4}$$

Based on the simple model, parallel resistor-capacitor (RC) networks are added to simulate Li-ion battery's dynamic behavior. The series circuit model with one RC circuit network is shown in Fig. 2.3.

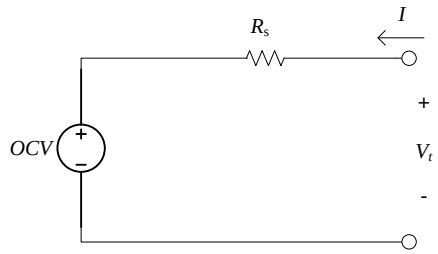

Fig. 2.2. The simple series circuit model for Li-ion batteries [115].

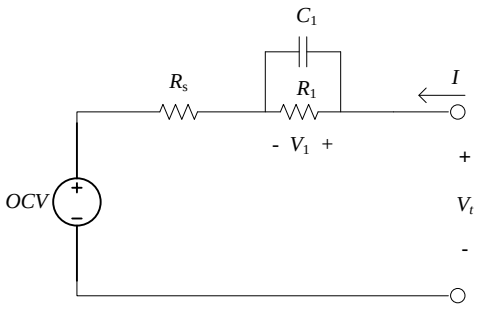

Fig. 2.3. The series circuit model with one RC network for Li-ion batteries [115].

The model equations are derived as (2.5) and (2.6):

$$\dot{V}_1 = -\frac{1}{R_1 C_1} V_1 + \frac{1}{C_1} I \tag{2.5}$$

$$V_t = OCV + V_1 + R_s I \tag{2.6}$$

With one RC network describing battery's dynamic characteristics, the series circuit model's accuracy is improved. It can be used for both the single battery and battery packs. More RC networks can be included to improve the model, whereas more RC circuits make the model more complicated. The model with appropriate trade-off between accuracy and simplicity is the series circuit model with two RC networks [6, 17]. The model circuit is depicted in Fig. 2.4. Here, V_t represents the terminal voltage. The battery's OCV is also represented by a voltage source and the battery's behavior is described by resistors and capacitors in the circuit. The series resistance R_s describes the battery's instant dynamics when the current changes. The RC network parameters include R_1, C_1, R_2, C_2. R_1 and C_1 describe the RC circuit representing the effects of the double-layer capacity [46] with short time constant. R_2 and C_2 describe the RC circuit representing the diffusion phenomenon in the electrolyte [46] with long time constant. The voltages across the RC networks are represented by V_1 and V_2. The model equations describing the model circuit are deduced as (2.7)-(2.9):

$$\dot{V}_1 = -\frac{1}{R_1 C_1} V_1 + \frac{1}{C_1} I \tag{2.7}$$

$$\dot{V}_2 = -\frac{1}{R_2 C_2} V_2 + \frac{1}{C_2} I \tag{2.8}$$

$$V_t = OCV + V_1 + V_2 + R_s I \tag{2.9}$$

All the circuit parameters are changing to SOC, temperature and battery aging level. Such effects will be considered and discussed in later chapters.

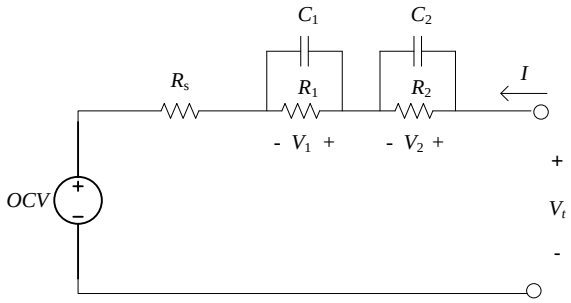

Fig. 2.4. The series circuit model with two RC networks for Li-ion batteries [6].

2.2.3 Experiment and Model Comparison

To establish and compare the models described in the above sections, one Li-ion battery is tested by an experiment. A constant pulse current test [17] is applied to a fully charged Sanyo 18650 Li-ion battery. The battery's nominal capacity C_n is 2.6 Ah. The definition of the nominal capacity is the capacity in Amp-hour of the charge stored in the battery [17]. Thus, for the tested battery,

$$C_{capacity} = C_n \cdot 3600 = 2.6 \cdot 3600 = 9360 \; coulomb \,. \tag{2.10}$$

Each current pulse that consumes the capacity of $0.1C_n$ and reduces SOC by 0.1 is set by 0.3C. Here, the symbol C represents C-rate, which is defined as the ratio of the applied charging or discharging current to the battery nominal capacity [75]: $I[C] = I[A] / C_n[Ah]$. After each pulse, a resting period of 20 mins is taken to make the battery achieve the equilibrium state. An existing battery testing system, Arbin BT2000, is used to control the battery current and record the measurements. This tester provides charging and discharging current in the range of 0~5 A, which is the same range to the tested battery's operating current. The data sampling interval is 1s. When the battery reaches the cut-off voltage, the experiment is stopped by the testing system automatically. The experiment lasts 21920 s. The temperature range for operations of the tested battery is -20 ℃ to 60 ℃. The temperature effect on Li-ion battery model is excluded by maintaining the environmental temperature around room temperature of 25 ℃. From the manufacturer's

instruction, the tested battery has a limited range for the terminal voltage as: V_{full} = 4.2 V, $V_{cut\text{-}off}$ = 3 V. The nominal voltage is 3.7 V.

The experimental platform is shown in Fig. 2.5. As the unmeasurable variable, the battery SOC is calculated by a Coulomb counting method using the testing current and sampling time recorded by the testing system. The initial SOC is set as 1 because the battery is fully charged before testing. The battery current, terminal voltage measured by the system and the calculated SOC are shown in Figs. 2.6-2.8. In Fig. 2.6, the discharging current is set negative.

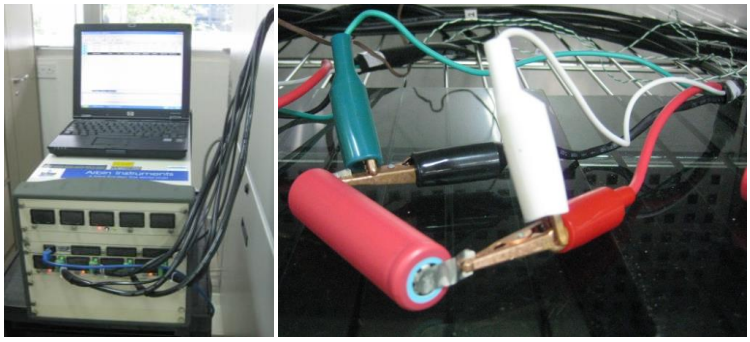

Fig. 2.5. The battery testing system.

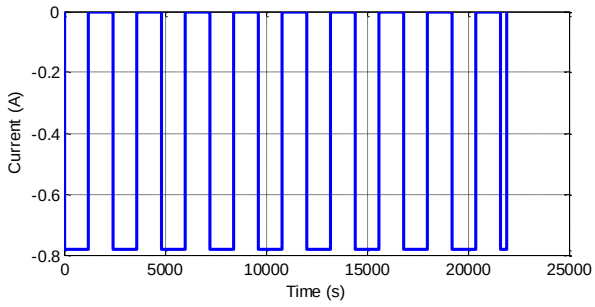

Fig. 2.6. The constant pulse testing current.

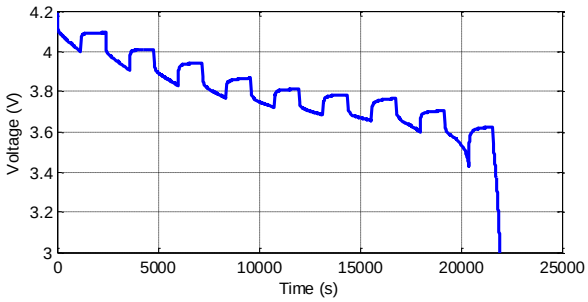

Fig. 2.7. Battery terminal voltage.

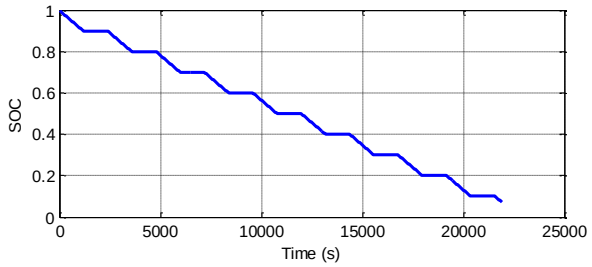

Fig. 2.8. Battery SOC.

It is assumed that a current resting period of 20 mins can make the battery achieve the steady state. Hence, the OCV at every 0.1 SOC is obtained by the measured terminal voltage at the end of each resting period. The nonlinear relationship between OCV and SOC is approximated by the curve fitting tool box in Matlab. The OCV-SOC relationship is described as (2.11):

$$OCV(SOC) = 3.695 + 0.1166SOC + 0.1732SOC^2 + 0.2102SOC^3 - 0.6944e^{-20.88SOC} \quad . \tag{2.11}$$

The measured battery OCV compared with the approximated OCV curve versus SOC is shown in Fig. 2.9. It is verified that the curving fitting results approximate the actual OCV accurately.

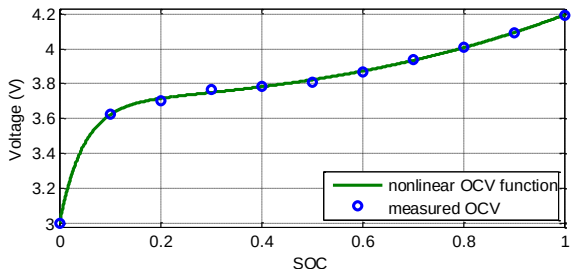

Fig. 2.9. OCV versus SOC.

In this section, other parameters of the equivalent circuit model are set constant to simplify the modeling process. Only the measurements at $SOC = 0.5$ are taken to obtain the parameters [6]. The battery voltage at $SOC = 0.5$ with the current $I = 0$ is shown in Fig. 2.10.

For the series circuit model, R_s is determined from the ratio between the instant voltage increase or drop when the current applies or stops. The voltage variation caused by R_s when the current changes is depicted in Fig. 2.10. R_s is calculated by:

$$R_s = \frac{V(R_s)}{I}. \tag{2.12}$$

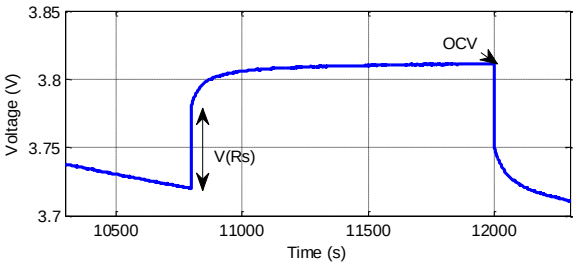

Fig. 2.10. The voltage in the resting period.

The circuit parameters in the RC networks are also identified from the battery terminal voltage in Fig. 2.10 [116]. The curve fitting method is applied. This technique does not need any prior knowledge of the RC circuit's time constant. The voltage curve in the battery resting period is approximated by the curve fitting tool box in Matlab. Considering the series model with one RC network, the battery terminal voltage is expressed by (2.6) with $I = 0$. Hence, the voltage curve in the resting period is described by the following equation:

$$V_t(t) = OCV + a \cdot e^{bt} \tag{2.13}$$

where *OCV* could be calculated by (2.11) with $SOC = 0.5$, and a and b are the coefficients determined by curve fitting. The curve fitting results from Matlab are shown in Fig. 2.11. Then, the RC circuit parameters are calculated by

$$R_1 = -\frac{a}{I},\ C_1 = -\frac{1}{R_1 b}. \tag{2.14}$$

The parameters for the series model with one RC network identified from experiments are shown in Table 2.1.

Table 2.1. Model parameters for the series circuit model with one RC network.

R_s	R_1	C_1
0.0782 Ω	0.02852 Ω	5222 F

For the series model with two RC networks, its voltage is expressed by (2.9). The battery voltage in the resting period with $I = 0$ is described by:

$$V_t(t) = OCV + p_1 \cdot e^{q_1 t} + p_2 \cdot e^{q_2 t} \tag{2.15}$$

where *OCV* has been calculated. The coefficients p_1, q_1, p_2, q_2 are also calculated by curve fitting. The curve fitting results from Matlab are shown in Fig. 2.12. Then, the RC circuit parameters are determined by:

$$R_1 = -\frac{p_1}{I},\ R_2 = -\frac{p_2}{I},\ C_1 = -\frac{1}{R_1 p_1},\ C_2 = -\frac{1}{R_2 p_2}. \tag{2.16}$$

The parameters for the series circuit model with two RC networks identified from experiments are shown in Table 2.2.

Table 2.2. Model parameters for the series circuit model with two RC networks.

R_s	R_1	C_1	R_2	C_2
0.0782 Ω	0.0249 Ω	1593 F	0.0135 Ω	22168 F

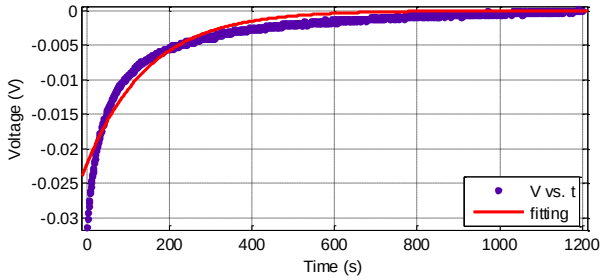

Fig. 2.11. Curve fitting results for R_1 and C_1.

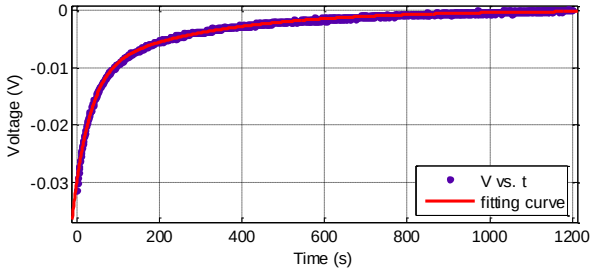

Fig. 2.12. Curve fitting results for R_1, C_1, R_2, C_2.

The parallel circuit model parameters are also calculated from the same experiment to make a comprehensive comparison. The resistors and capacitors in Fig. 2.1 are determined from the circuit analysis method [18]. Hence,

$$C_b = \frac{2C_n \cdot 3600 \cdot V_{full}}{(V_{full}^2 - V_{cut-off}^2)} = \frac{2 \cdot 9360 \cdot 4.2}{(4.2^2 - 3^2)} = 9100\,F\,. \tag{2.17}$$

It is assumed that R_t holds 25% of the internal resistance and R_p has the same resistance as R_b. The sum of R_t and R_b is determined from the battery voltage increase when the pulse current changes in Fig. 2.10, which is similar to (2.12):

$$R_t + R_b = \frac{V(R_s)}{I} \tag{2.18}$$

The capacitance of C_p is determined by:

$$C_p = \frac{\tau}{R_b + R_p} \tag{2.19}$$

where τ is the RC circuit's time constant. It is assumed that τ is the same as the time constant of the series model with one RC network. The parallel circuit model parameters are shown in Table 2.3:

Table 2.3. Model parameters for the parallel circuit model.

R_p	C_p	R_b	C_b	R_t
0.0196 Ω	1253.1 F	0.0588 Ω	9100 F	0.0588 Ω

After obtaining all the parameters for Li-ion battery equivalent circuit models, the different type models are established in Matlab/Simulink. The battery current in Fig. 2.6 is applied to the models. The output voltages from different models compared with the actual battery terminal voltage are shown in Fig. 2.13.

From the model output comparison in Fig. 2.13, it is obvious that the series circuit model has better performance than the parallel model. The series model's RC networks also improve the model's dynamic characteristics significantly. The root mean squared errors (RMSEs) for different models are calculated and compared in Table 2.4. It verifies that the series equivalent circuit model with two RC networks has the best accuracy for Li-ion battery.

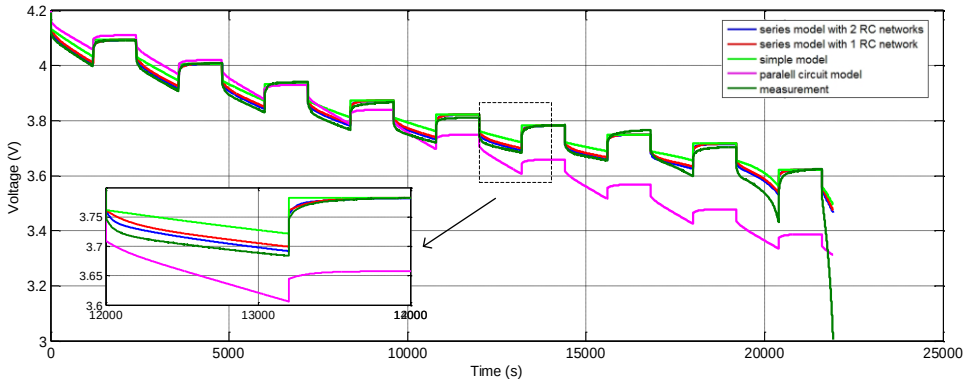

Fig. 2.13. The model output voltages compared with the actual voltage.

Table 2.4. The comparison of RMSEs for different models.

Simple model	Series model (1 RC)	Series model (2 RC)	Parallel model
0.0434 V	0.0337 V	0.0310 V	0.1162 V

2.3 A Fuzzy Logic-Based Model for Li-ion Batteries with Temperature Effect

In this section, a fuzzy logic-based Li-ion battery model considering temperature effect is established by experiments.

2.3.1 Experimental Setup

The battery model considering temperature effect is based on the battery circuit model described in Fig. 2.4. The same constant pulse current test in Fig. 2.6 is applied to another Li-ion battery with nominal capacity 2.6 Ah. All experiments are done in a thermal chamber maintaining different temperatures. The temperatures of 15 ℃, 25 ℃ (room temperature), 35 ℃ and 45 ℃ are tested. The experimental platform is shown in Fig. 2.14. To obtain the temperature effect clearly and exclude the effect caused by battery aging, the tested battery is new. The battery terminal voltage curves at different test temperatures are shown in Fig. 2.15. It indicates that temperature has obvious effect on Li-ion battery's operation.

Fig. 2.14. The test platform.

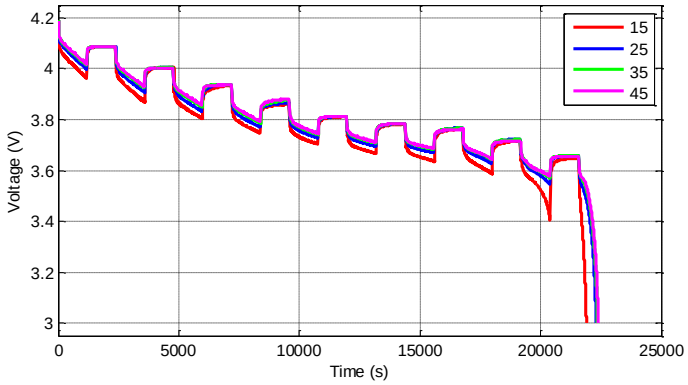

Fig. 2.15. The battery voltage curves at different temperatures.

The temperature also has effect on Li-ion battery's actual capacity represented by C_a. To obtain this effect, a constant discharging process (0.2C) is tested at 15 ℃, 25 ℃, 35 ℃ and 45 ℃. Before discharging, the battery has been fully charged with a constant 0.5C current and then 4.2 V constant voltage, until the charging current decays to 0.025 A. The discharging process stops when the battery voltage is smaller than 3 V. The discharging capacity is provided by the tester. At 25 ℃, the battery actual capacity is the same as C_n. In Fig. 2.16, the capacity C_a at 25 ℃ is set as 1. The capacities at other temperatures compared to the capacity at 25 ℃ are described in Fig. 2.16. It shows that at above 25 ℃, the battery actual capacity is almost constant with the same value of C_n. The capacity decreases obviously to a value of C_{n1} when the temperature is around 15℃. It reveals that the battery capacity changes drastically when battery operates below room temperature, and stays nearly constant above room temperature.

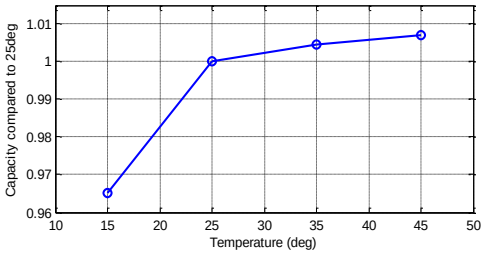

Fig. 2.16. The comparison of battery capacity at different temperatures.

2.3.2 Model Parameter Extraction

The circuit parameters are extracted from the battery voltage data by the same method described in Section 2.2.3. SOC is calculated by the tester using equation (1.1). The OCV curves at the four test temperatures are depicted in Fig. 2.17. It shows the OCV curves are almost the same at different temperatures. The OCV curve at 15 ℃ is also very similar to the curve at higher temperatures. Therefore, OCV is considered temperature independent and with the same expression as (2.11).

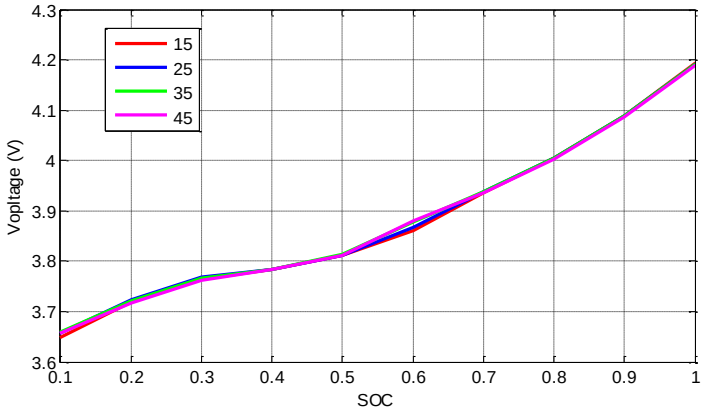

Fig. 2.17. The OCV curves at different temperatures.

The R_s values at different temperatures within the entire SOC range are depicted in Fig. 2.18. It is shown that R_s varies with SOC and temperature, indicating that both temperature and SOC have effect on R_s. Thus, the SOC effect on model parameters is also considered here.

The parameters of the RC ladders are also determined by the battery's terminal voltage during the resting period. The RC ladder parameters may vary to some extent by using the curve fitting method. It has been indicated in [17] that all the RC parameters stays nearly

constant in $SOC \in [0.2,1]$ and changes drastically in $SOC \in [0,0.1]$. To simplify the modeling process, R_1, R_2, C_1, C_2 are set constant in the region of $SOC \in [0.2,1]$ by $SOC = 0.5$ [17]. The values of R_1, R_2, C_1, C_2 at each test temperature are shown in Fig. 2.19. Similar to R_s, all the RC parameters also vary with temperature.

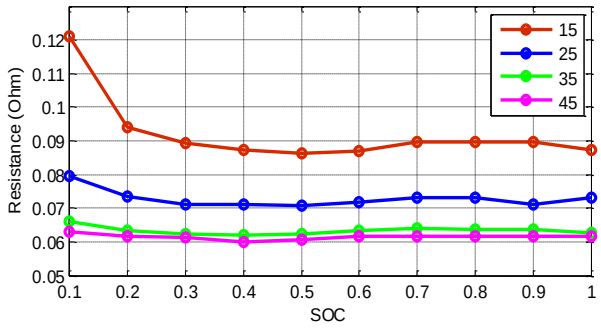

Fig. 2.18. The R_s values over the SOC range at test temperatures.

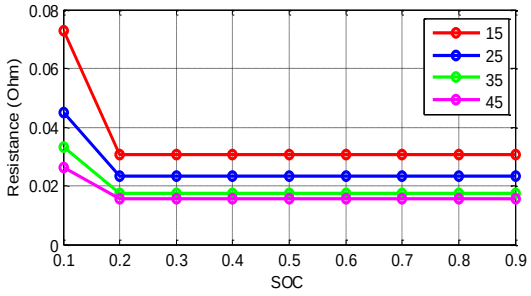

a) R_1.

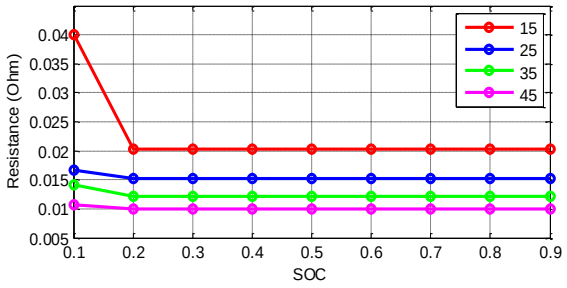

b) R_2.

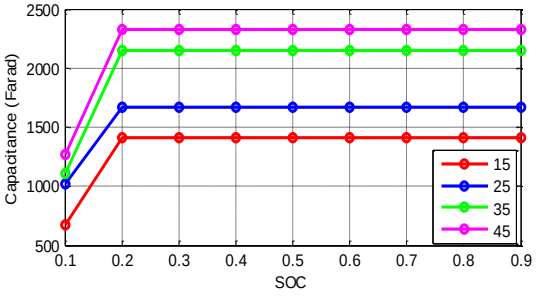

c) C_1.

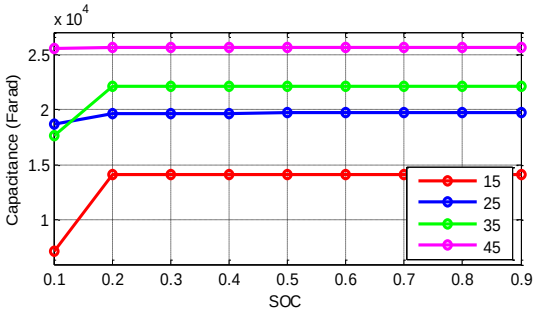

d) C_2.

Fig. 2.19. The RC parameter values at test temperatures.

2.3.3 The Fuzzy Logic-Based Model for Li-ion Batteries

The above section shows that the equivalent circuit model parameters are influenced by temperature and SOC. In this section, a global fuzzy logic-based model considering the parameters' variation to temperature and SOC is established. Fuzzy logic can describe

several antecedents in one rule and approximate system nonlinear dynamic properties with high accuracy. Therefore, the model parameters' variation to temperature and SOC represented by fuzzy rules could model the battery dynamics accurately. In our model, the parameter values around some partition points of temperature and SOC are taken as the fuzzy rule consequents.

1) Fuzzy rules describing the battery capacity

It has been stated that the battery capacity is almost constant around or above room temperature. When the temperature is below room temperature, the capacity becomes lower. To describe this variation trend, the fuzzy rule base of temperature for battery actual capacity C_a is determined by:

Rule 1: IF T is ($T \geq 23$℃), THEN $C_a = C_n$;

Rule 2: IF T is ($T \leq 15$℃), THEN $C_a = C_{n1}$,

where C_n and C_{n1} have been obtained from battery test in Section 2.3.1. The methodology to determine the fuzzy rules for model parameters within a low temperature range is based on the temperature scope described in this section. Here, the battery capacity within the interpolated interval $15\ ℃ < T < 23\ ℃$ is represented by a combination of these two rules with the membership function $\mu(T)$. Hence, the battery capacity varying with temperature is determined by:

$$C_a(T) = \sum_{m=1}^{2} \mu_m(T) \cdot C_{nm}, \tag{2.20}$$

where $\mu_m(T)$ represents the membership functions associating to the fuzzy rules. Here, $0 \leq \mu_m(T) \leq 1$ and $\sum_{m=1}^{2} \mu_m = 1$. The trapezoidal membership functions are shown as Fig. 2.20.

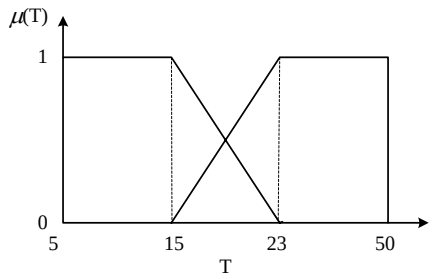

Fig. 2.20. The membership functions of temperature for C_a.

2) Fuzzy rules describing the model parameters

For the resistors in the model, the variation pattern of affecting factors should be established. First, the two affecting factors, SOC and temperature, are considered separately. The effect of SOC on the model parameters is analyzed based on the parameter variation trend at a specific temperature. As Fig. 2.18 shows, the variation trend of R_s versus SOC at each temperature is similar. The R_s value varies little within the region $SOC \geq 0.2$ at each temperature. In the region $SOC < 0.2$, R_s begins to increase. To describe this variation trend by fuzzy rules, the partition points and the membership functions are selected according to the R_s value over the SOC range. Hence, the SOC range is divided by two regions: [0, 0.1] and [0.2, 1]. Then, the rules can be optimized and verified by existing fuzzy identification algorithms [117]. The partition points can be amended to optimum subspace divisions to achieve high modeling accuracy over the entire range of the antecedent SOC. In this case, considering the model's accuracy and simplicity, the partitioning points of 0.1 and 0.2 of SOC are selected and the trapezoidal membership function is utilized. The fuzzy rule base is established by:

Rule 1: IF SOC is ($SOC \geq 0.2$), THEN $R_s = R_{s1(soc)}$;

Rule 2: IF SOC is ($SOC \leq 0.1$), THEN $R_s = R_{s2(soc)}$.

The membership functions over the entire SOC range for R_s are shown in Fig. 2.21.

The variation trends for the RC network parameters at a specific temperature are assumed to be similar to R_s. Hence, R_1, C_1, R_2, and C_2's variations to SOC are represented by similar fuzzy rule base. The membership functions of SOC associating to the fuzzy rules are defined the same to R_s.

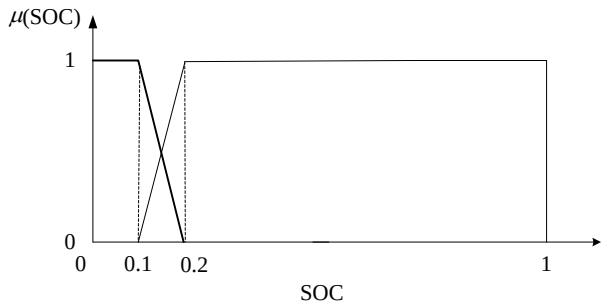

Fig. 2.21. The membership functions of SOC for R_s and the RC parameters.

After obtaining the fuzzy rules representing model parameters' variation versus SOC, the temperature effect is considered. The R_s values within the region of $SOC > 0.2$ and $SOC < 0.1$ at different temperatures are shown in Fig. 2.22. It indicates that R_s increases when the temperature decreases. When the temperature is above 35 ℃, R_s varies little, implying that the effect on R_s is not obvious in the high temperature region, i.e. above a temperature higher than 35 ℃, R_s remains almost constant. The difference in the R_s value between 15 ℃ and 25 ℃ is much larger than the difference between 25 ℃ and 35 ℃, indicating that R_s changes more drastically when the temperature is lower than the room temperature, i.e. R_s varies continuously over the interval between 15 ℃ and room temperature.

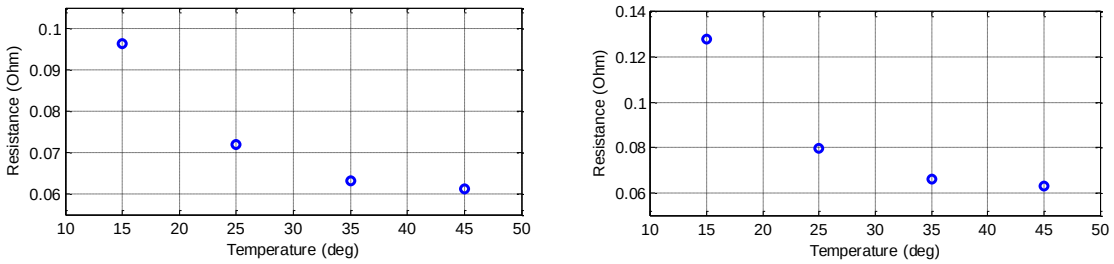

a) SOC > 0.2. b) SOC < 0.1.

Fig. 2.22. The R_s values at different temperatures.

The fuzzy rules are determined roughly based on the existing R_s data at different temperatures. Within the temperature interval from room temperature to high temperature, although data is collected from three test temperatures, R_s is set to be represented by 2 fuzzy rules because R_s's variation versus temperature is not severe in this region. The interpolated interval is selected as 10℃ considering the temperature range and parameter

variation scope. Here, the partition points in this temperature region are set to A and A+10. The R_s value tested at 35℃ is taken to determine A. $R_{s(T=35)}$ is a combined value calculated by:

$$\mu_{(T\in(T_{high}))}(35)\cdot R_{s(T_{high})}+\mu_{(T\in(T_{room}))}(35)\cdot R_{s(T_{room})}=R_{s(T=35)}\,. \tag{2.21}$$

When (2.21) is solved, A = 27. In this way, the temperature range 23~27℃ is taken as the room temperature interval. The trapezoidal membership function is also utilized over the entire temperature range. The fuzzy rule base is described as:

Rule 1: IF T is ($T \le 15$ ℃), THEN $R_s = R_{s1(T)}$;

Rule 2: IF T is (23 ℃ $\le T \le$ 27 ℃), THEN $R_s = R_{s2(T)}$;

Rule 3: IF T is ($T \ge 37$ ℃), THEN $R_s = R_{s3(T)}$.

The membership functions of the temperature for R_s are shown in Fig. 2.23.

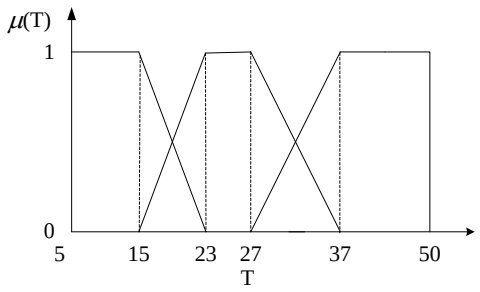

Fig. 2.23. The membership functions of temperature for R_s and the RC parameters

As shown in Fig. 2.24 a), the R_1 value's variation versus temperature trend is similar to that of R_s. To simplify the model, the same partition points and membership functions of the temperature for R_s are set for the RC ladder parameters. It should be mentioned that C_1 and C_2's variation versus temperature trends are opposite to those of the resistors, which indicates that C_1 and C_2 have larger capacitance at high temperature and smaller capacitance at low temperature. The values of C_1 varying with temperature are shown in Fig. 2.24 b).

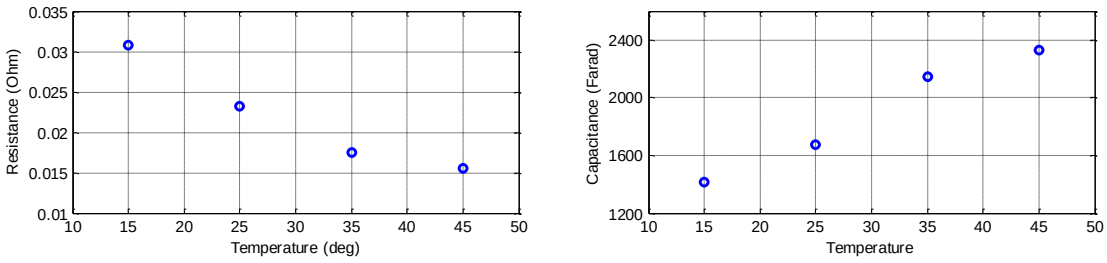

a) R_1. b) C_1.

Fig. 2.24. The R_1 and C_1 values at different temperatures.

After separately determining the fuzzy rules representing SOC and temperature's effect on model parameters, the comprehensive fuzzy rule bases considering the two factors together are established. To synthesize fuzzy rules of the two affecting factors, the connective "AND" is used. For example, the global fuzzy rule base for R_1 is described as:

Rule m: IF $SOC \in (SOC_{m,1})$ AND $T \in (T_{m,2})$, THEN $R_1 = R_{1m(SOC,T)}$, $m = 1, 2..., M$.

Here, M represents the number of fuzzy rules, determined by $M(SOC) \cdot M(T)$. Hence, the membership function $\mu(SOC, T)$ for *Rule m* is determined by:

$$\mu_m(SOC, T) = \mu_{(m,1)}(SOC) \cdot \mu_{(m,2)}(T). \tag{2.22}$$

Then, a two-dimension fuzzy membership function schematic is drawn in Fig. 2.25. Here, the operating space of SOC and temperature is decomposed into fifteen zones. The R_1 value is determined by:

$$R_1(SOC, T) = \sum_{m=1}^{M} \mu_m(SOC, T) \cdot R_{1m}. \tag{2.23}$$

The global fuzzy rule bases of SOC and temperature for other parameters are in the same form.

Hence, the fuzzy logic-based model considering SOC and temperature's effect on parameters is completed. The advantage of this modeling method is that only a few tests at specific temperatures are needed. The variation trends of model parameters versus SOC and temperature are described simply and clearly, especially for the parameters varying to both two factors.

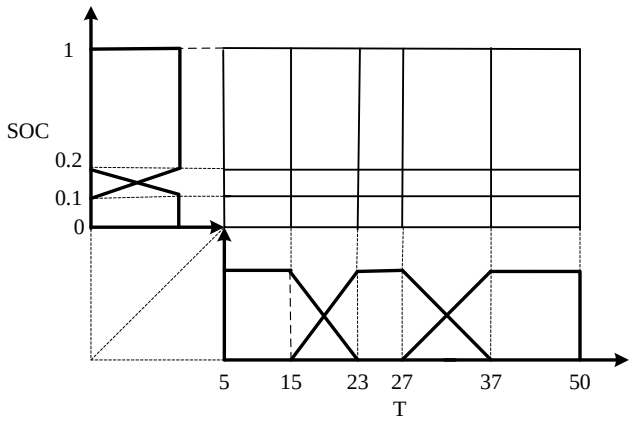

Fig. 2.25. The 2-dimension function membership schematic for R_1.

2.3.4 Model Verification

To verify that the proposed model can describe Li-ion battery dynamics at various SOC and temperatures, different current patterns shown in Fig. 2.26 a) and b) are applied in experiments. The corresponding SOC calculated by (1.1) for these two current patterns are shown in Fig. 2.26 c) and d). To test the model's flexibility over the entire temperature range, the experiments are done at some new temperatures. The tests stop when the battery voltage is smaller than 3V. The new test temperatures include 19 ℃, 20 ℃, 30 ℃, and 40 ℃. All the comparisons between the experimental battery voltage and the proposed model voltage in different conditions are shown in Figs. 2.27 a)-e). The RMSEs in various test conditions are shown in Table 2.5. It shows that for all the tests, the RMSE is smaller than 0.03 V. Especially, in the range when $SOC \in [0.1,1]$, the maximum model error is smaller than 0.03 V for most tests, except the 19 ℃/20 ℃ condition because the temperature effect on battery capacity is more obvious at lower temperature. All the large model errors exist in the range when $SOC \in [0,0.1]$. The model accuracy in small SOC range could be significantly improved if more fuzzy rules for this range are added. Thus, it is verified that the proposed model has high accuracy for Li-ion batteries over the entire SOC and temperature range.

Table 2.5 Model RMSEs for verification.

T/Current pattern	RMSE (V)
15 ℃/pulse current	0.0222
25 ℃/pulse current	0.0191
35 ℃/pulse current	0.018
45 ℃/pulse current	0.0172
19 ℃/current pattern 1	0.026
30 ℃/current pattern 1	0.0206
25℃/current pattern 2	0.0157
20 ℃/current pattern 2	0.0184
40 ℃/current pattern 2	0.0145

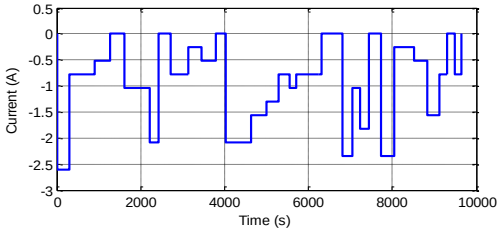

a) Current pattern 1.

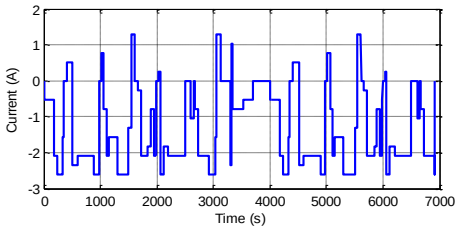

b) Current pattern 2.

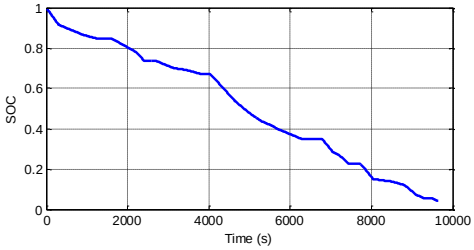

c) SOC for current pattern 1.

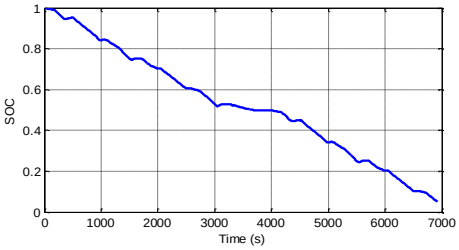

d) SOC for current pattern 2.

Fig. 2.26. Testing current pattern and SOC.

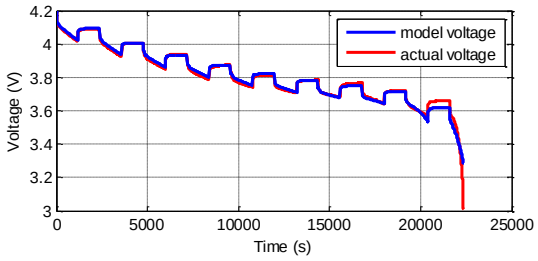

a) 35 ℃.

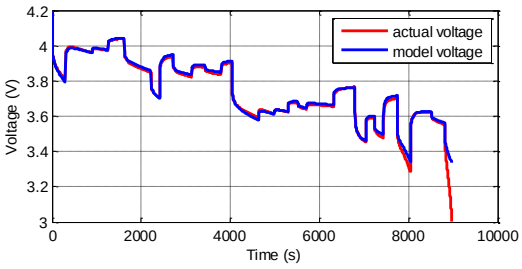

b) 19 ℃.

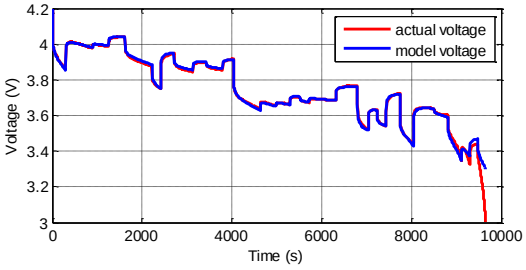

c) 30 ℃.

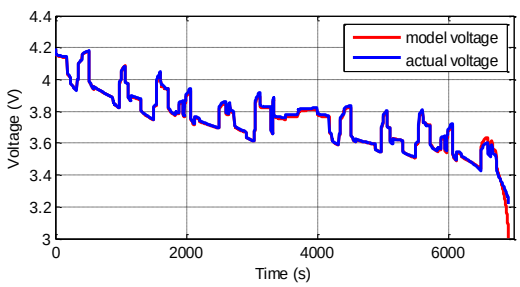

d) 40 ℃.

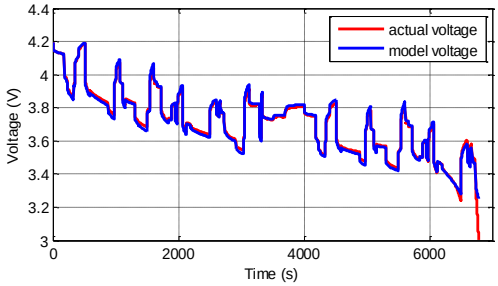

e) 20 ℃.

Fig. 2.27. The battery voltage compared with model voltage at different temperatures.

2.3.5 Battery Surface Temperature

In the previous section, only the ambient temperature is considered. Restricted by the experimental condition, the ambient temperature lower than 5 ℃ and higher than 50 ℃ is not considered in this research, whereas the modeling method in these temperature ranges is similar. To analyze the temperature effect more accurately, the battery surface temperature is also tested in this section. A data logger connected with thermocouples as shown in Fig. 2.28 are utilized in the experiment to record the battery surface temperature. Firstly, the pulse current test in Section 2.2.3 with the thermal chamber temperature maintained at 25 ℃ is conducted on a new 2.6 Ah Li-ion battery. The battery surface temperature is shown in Fig. 2.29 a). The sampling time is 10 s. It is clear that the battery

stays around the same temperature with ambient temperature when the battery is not in operation. When current applies, the battery temperature increases because of battery thermal characteristics. Then, the thermal chamber's temperature is improved to 40 ℃ and the current test in Fig. 2.26 b) is performed. The battery temperature is shown in Fig. 2.29 b). It is clear that the battery temperature's increase during the operation is lower than 4 ℃ without any cooling and thermal management measures. With a specially designed module structure and an ideal cooling strategy in battery pack, it is assumed that the battery's surface temperature will not vary too much with the ambient temperature in this research. In practice, the ambient temperature for the EV battery pack during operation will not change drastically. Besides, the battery current in EVs is limited to prevent overheating. Thus, it is reasonable to assume that the batteries in EVs are thermal balanced and operating within a narrow optimal temperature range. The battery model parameters could be determined by referring to the measured ambient temperature. With a certain ambient temperature range, the temperature effect on battery could be put aside temporarily. In later chapters, all the experiments and operations are under room temperature according to our experimental condition and the temperature effect is excluded.

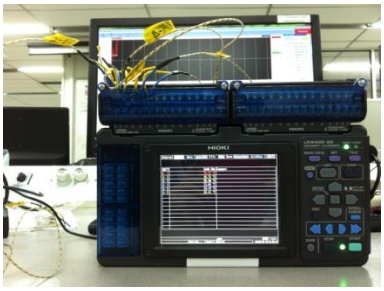

Fig. 2.28. Data logger connected with thermocouples in experimental setup.

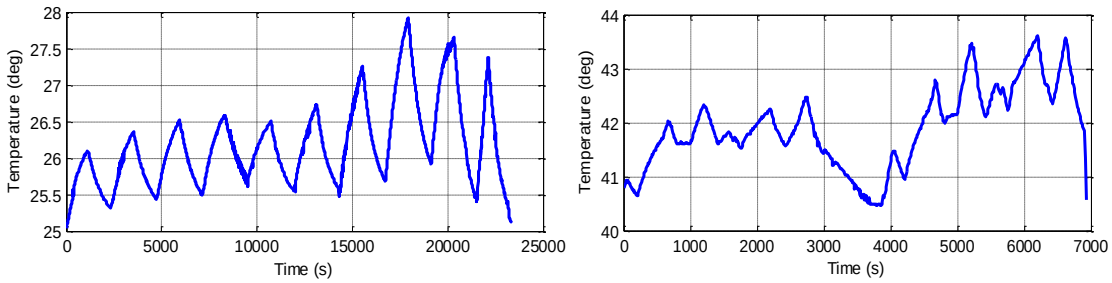

a) 25℃. b) 40℃.

Fig. 2.29. The battery temperature at ambient temperature of 25 ℃/40 ℃.

2.4 Li-ion Battery Model Proposed by Neural Networks

Although having good performance, sometimes the equivalent circuit type model for Li-ion battery may bring inconvenient modeling process. For example, it takes a long time to make the battery arrive at the equilibrium state when measuring OCV. The curve fitting process for identifying the circuit parameters may also be complex and time-consuming. For some simple current types, it is more convenient and intuitive to establish a mathematical battery model from NNs.

It has been stated that the equivalent circuit parameters are changing to different factors in practice. Such parameter variation brings complex equation and obvious nonlinearity to the circuit model. Thus, in experimental condition with simple current pattern, the NN model can be applied to Li-ion batteries to avoid the complex modeling process and complicated expressions in the model equations.

NNs can describe nonlinear mapping directly from existing input-output samples. The NN model provides a black box model without the need to know the battery's inner structure and electrochemical reactions, brining significant convenience to the battery modeling process. All the factors affecting the Li-ion battery's behavior can be taken as model inputs without considering their specific effects on the model parameters. After designing the model's inputs and outputs, existing learning algorithms can be applied to train the model automatically without the knowledge of the elements inside the black box. NNs can approximate any nonlinear function with desired accuracies [25]. NNs also have powerful capability of computational intelligence. Using appropriate training data set, a mathematical model describing the variation of the battery parameters regardless the expressions of exact laws can be obtained. Moreover, the NN learning algorithms provide a discrete model directly during the learning process. Thus, the battery model established by NNs can be controlled and estimated directly by discrete control methods such as KF-based methods. It will be easy for engineers to handle.

Recently, the model proposed by NNs is applied to Li-ion batteries more and more widely. Researchers establish the Li-ion battery's NN model approximating its characteristics with high accuracy. The battery NN model describes the relationships between SOC,

voltage, current and other battery state influential factors with mathematical equations. In this section, the NN model for Li-ion batteries is established and improved.

2.4.1 The Extreme Learning Machine Algorithm

Although NNs are suitable for Li-ion battery modeling, traditional NN algorithms still have the flaws of heavy computation and long training time. For traditional NNs, the model parameters need to be tuned iteratively during training. The iteration steps need large amounts of computation and make the mapping learning process inefficient [29, 118]. On the other hand, to represent Li-ion battery's dynamic characteristics comprehensively and achieve the desired model accuracy, the training data sampling time must be short enough. Thus, the amount of training data may be large. Hence, a faster mapping learning algorithm is needed here.

In this section, the ELM algorithm introduced in [29] is applied to establish the Li-ion battery model. Unlike conventional learning algorithms, ELM provides good learning performance with simple learning process at extremely fast speed. For ELM, there is no need to tune the model parameters during training. The input weights connecting the input neurons and hidden neurons and the hidden layer biases are chosen randomly [29, 118-121]. The output weights connecting the hidden neurons and output neurons are determined analytically. There is no dependency between the weights and the biases. ELM trains data fast and provides satisfactory training error with smaller norm of weights [29]. Compared with traditional NNs, the ELM algorithm has simpler model training process, satisfactory training accuracy, and spends much less time on training.

The application of ELM makes the battery modeling process simpler and provides a more accurate representation of the battery model's input-output relationship. Thus, a discrete Li-ion battery model is trained by ELM using the sampled data from experiment in this section. The input-output mapping in Fig. 2.30 is designed as the model structure, where x_j represents the model input vector and t_j represents the model output. One hidden layer is set for the proposed model.

The 3-step ELM learning algorithm is described as follows:

Step 1: Randomly assign the input weight vector $a_i = [a_{i1}, a_{i2}, ..., a_{in}]^T$ and the hidden layer bias b_i, where *i* represents the *ith* hidden node. The number of hidden nodes is set to *L*. The value of *L* is determined flexibly so as to achieve acceptable accuracy.

Step 2: Determine the hidden layer output matrix. The model is expressed as:

$$\sum_{i=1}^{L} \beta_i G(a_i, b_i, x_j) = t_j,\ j = 1, ..., N \tag{2.24}$$

where β_i is the output weight connecting the *ith* hidden neuron and output node. The activation function $G(x)$ is determined before training [29, 120]. In this case, a sigmoid function is used as the activation function $G(x)$ in (2.25):

$$G(a_i, b_i, x_j) = (1 + e^{-(a_i \cdot x_j + b_i)})^{-1}, i = 1, ..., L,\ j = 1, ..., N \tag{2.25}$$

(2.24) can be written in the equivalent form:

$$H\beta = T \tag{2.26}$$

where

$$H = \begin{bmatrix} G(a_1, b_1, x_1) & \dots & G(a_L, b_L, x_1) \\ \vdots & \dots & \vdots \\ G(a_1, b_1, x_N) & \dots & G(a_L, b_L, x_N) \end{bmatrix}_{N \times L}, \quad \beta = [\beta_1, ..., \beta_L]^T, \text{ and } T = [t_1, ..., t_N]^T. \ H$$

represents the hidden layer output matrix.

Step 3: Calculate the output weights. The output weights can be analytically determined through the generalized inverse operation of the hidden layer output matrix [29, 118]. Therefore, β is obtained by

$$\beta = H^+ T \tag{2.27}$$

where H^+ is the Moore-Penrose generalized inverse of *H* [122].

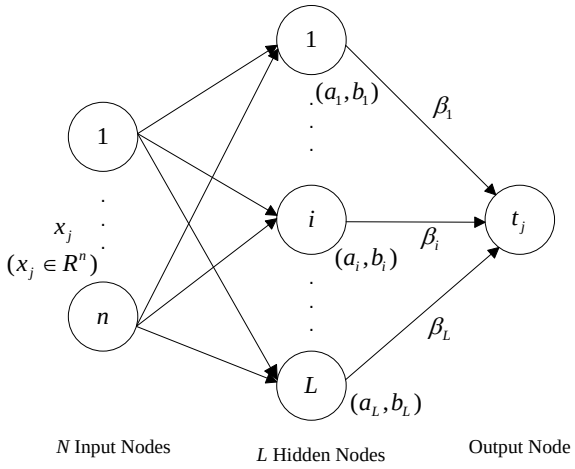

Fig. 2.30. Model structure of the ELM algorithm.

Considering the ELM algorithm described above, it is obvious that no iterative step is taken and this advanced technique will bring significant improvement to the model training speed. In general, the learning process of ELM is more efficient than that of traditional NNs. In [29], it has been tested and verified that the ELM algorithm has good accuracy and run much faster than traditional BP learning algorithm and support vector machines (SVWs). In the next section, the radial basis function neural network (RBF NN) will be taken as a comparison.

2.4.2 Radial Basis Function NN

RBF NN is a typical kind of feed-forward NN with nonlinear mapping characteristics, strong generalization ability and self-organized study ability [26]. Hence, RBF NN can be adopted to train the Li-ion battery model. The modeling structure is shown in Fig. 2.31. Here, a three-layer feed-forward network including one hidden layer is designed. x_j represents the model input vector and t_j represents the model output. $g(x)$ is the activation function of the hidden neurons, designed by Gaussian function:

$$g_i(x_j) = \exp(-\frac{\left\| x_j - c_i \right\|^2}{\sigma_i^2}), i = 1, 2...L \tag{2.28}$$

where L is the number of hidden neurons. c_i and σ_i represents the center and radius for the *ith* neuron. $\|...\|$ is the L_2 norm.

The model output is calculated by the sum of the weighted functions from the L neurons:

$$t_j = \beta_0 + \sum_{i=1}^{L} \beta_i G(x_j),\ j = 1, 2..N \tag{2.29}$$

where N represents the number of training data, $\beta_1 \sim \beta_L$ constitute the weight vector connecting the hidden neuron and the output layer. β_0 is defined as the bias weight adding directly to the output layer.

To improve the training efficiency, it should be noticed that all the input-output samples have been normalized before training.

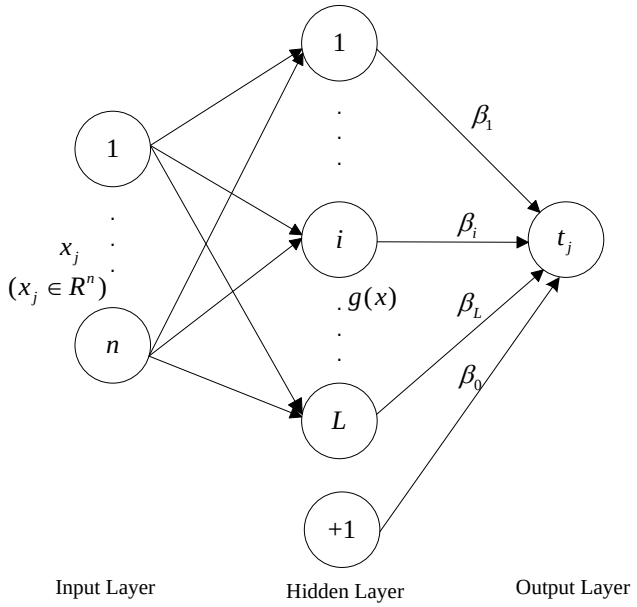

Fig. 2.31. The RBF NN model structure.

2.4.3 The Comparison between ELM and RBF NN Trained Battery Models

To establish the Li-ion battery model, the proposed model's inputs and output are determined first.

The SOC sampled at step *k*, $SOC(k)$, is taken as the model input since it represents the battery's present status. SOC has a nonlinear relationship with the battery voltage and current. The proposed model should be able to describe this relationship accurately. As the directly measured variable, the current $I(k)$ is taken as an input. The battery terminal voltage $V_t(k)$ is defined as the output. Moreover, the terminal voltage at sampling step $k-1$, $V_t(k-1)$, is chosen as the third input for the proposed model. $V_t(k-1)$ represents

the battery's status at the last step and implies the previous operation status. The theoretical ground for the selection of $V_t(k-1)$ is the derivative relationship of the equivalent circuit model stated in Section 2.2.2. As more inputs bring complexity to the model, the series circuit model with one RC network is utilized as the basis here. Simply transforming (2.6) to discrete form, the terminal voltage sampled at step *k* is expressed as:

$$V_t(k) = OCV(SOC(k)) + V_1(k) + R_s I(k) \tag{2.30}$$

where $V_1(k)$ represents the RC circuit voltage at the sampling step *k* relating to $V_1(k-1)$ via a first order differential equation derived from (2.5). To make the model inputs directly measured variables, $V_1(k-1)$ is considered being included in $V_t(k)$. Hence, $V_t(k-1)$ has a direct relationship with $V_1(k)$. A function expressing $V_t(k)$ is obtained by synthesizing the unknown parameters:

$$V_t(k) = F(V_t(k-1), I(k), SOC(k)) \tag{2.31}$$

which is to be approximated by learning algorithms.

The input vector and output for the proposed battery model are represented by $p(k) = [V_t(k-1) \quad I(k) \quad SOC(k)]^T$ and $V_t(k)$ respectively. The proposed model's mathematical equation is expressed by:

$$F(p(k)) = V_t(k). \tag{2.32}$$

The input-output samples of $\{p(k) \sim V_t(k)\}$ are used for model training. Define $p(k) = x_j$ and $V_t(k) = t_j$. The training set is defined as $\{(x_j, t_j) \mid x_j \in R^n, t_j \in R^m, j = 1, ..., N\}$. In this case, $n = 3$, $m = 1$. Here, *N* is the input-output sample number of the training set.

To obtain the input-output samples for the model training set, an experiment on battery discharging process is done. One fully charged 2.6 Ah Samsung 18650 Li-ion battery is tested. The ambient temperature is maintained around room temperature of 25 ℃. The testing pulse discharging current is shown in Fig. 2.32. In the figure, the discharging current is set positive because positive model inputs are used during model training.

During the experiment, the battery's terminal voltage, current and SOC are sampled and recorded by the existing battery testing system. The battery terminal voltage is shown in

Fig. 2.33. The SOC value is calculated with the Coulomb counting method in experimental condition, shown in Fig. 2.34. The initial SOC equals to 1. To avoid battery damage, the discharging process ends when the battery terminal voltage gets smaller than 3 V with 0.05 SOC. Therefore, the SOC range is from 1 to 0.05 in this test. The testing process lasts for 34020 s. Considering the desired model accuracy and the amount of the training data, the sampling interval for the experiment is set to 20 s.

Portions of the sampled data are selected to train the model. The input-output samples with SOC in the ranges of [1, 0.8] and [0.3, 0.05] are selected as the training data. The basis for this selection is that the samples in above ranges represent the typical battery dynamic characteristics and are highly nonlinear as described in Fig. 2.33. The training data amount is $N = 782$. After obtaining the training data, the ELM algorithm is applied to train the battery model. Meanwhile, RBF NN is taken for a comparison on both the training time and training accuracy.

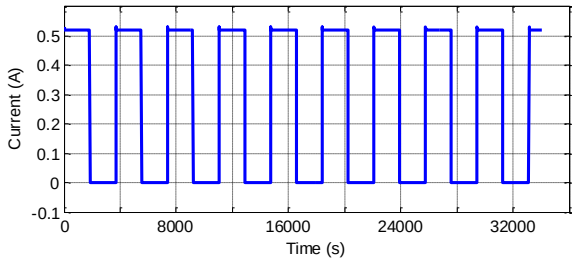

Fig. 2.32. The pulse discharging current for model training.

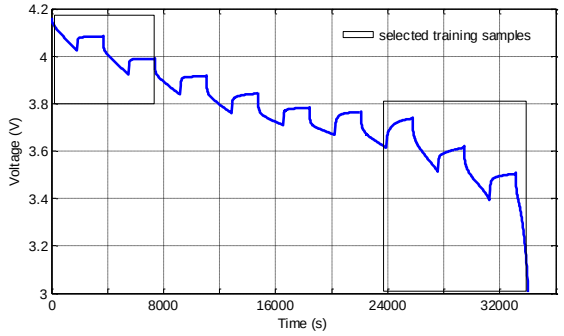

Fig. 2.33. Battery terminal voltage for model training.

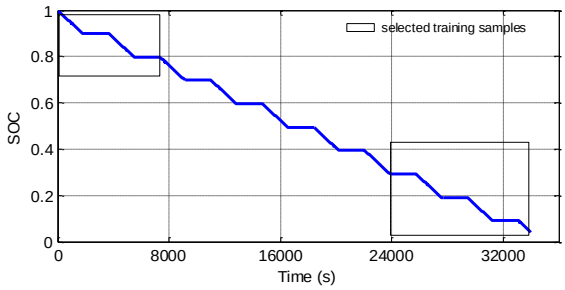

Fig. 2.34. Battery SOC for model training.

The same training data set extracted from the Li-ion battery discharging experiment is trained by the two algorithms of ELM and RBF NN. The data for verifying training accuracy is the whole sampled data set from the battery test. All the simulations are run in the computational environment of Matlab R2009b with the 2.66 GHz Intel Core 2 Quad CPU. The number of the hidden layer neurons is set to 10. At the end of training, the RMSE from RBF NN for the testing samples is 0.0138 V, which is much larger than 0.0056 V from ELM. The training time of RBF NN is much longer than the ELM algorithm.

The next comparison increases the number of hidden layer neurons to 15 for the two algorithms. In this case, the RMSE from RBF NN for the testing samples is similar to the ELM algorithm with 10 neurons, but still larger than ELM with 15 neurons. Moreover, the training time of RBF NN is also much longer than the training time of ELM. The testing errors for the two algorithms with 15 hidden neurons are shown in Fig. 2.35. It is obvious that ELM has smaller errors than RBF NN. Consequently, the ELM algorithm trains the input-output samples with higher accuracy and much less training time. A comparison between ELM and RBF NN is shown in Table 2.6. In this table, the algorithm training accuracy is represented by RMSE for the testing samples. In conclusion, the ELM algorithm improves both the training accuracy and reduces the training time for the Li-ion battery modeling process.

Table 2.6. The comparison between ELM and RBF NN.

	Training Time	Training Accuracy
ELM 10 neuron	0.0469 s	0.0056 V
ELM 15 neuron	0.0781 s	0.0026 V
RBF 10 neuron	4.3281 s	0.0138 V
RBF 15 neuron	7.1875 s	0.0064 V

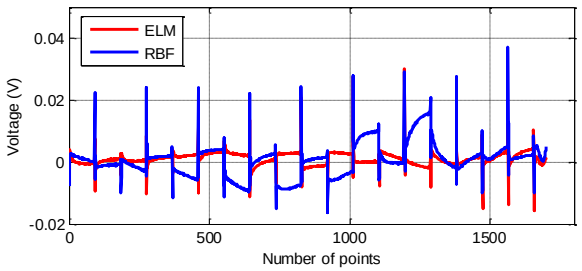

Fig. 2.35. The testing errors for ELM and RBF NN.

It is shown that ELM obtains better performance than RBF NN during the Li-ion battery modeling process. The ELM algorithm achieves a higher accuracy with less hidden neurons than that of RBF NN. It is obvious that more hidden layer neurons make the battery model more complex and improve the computation load for estimation. Therefore, the battery model trained by ELM with 10 hidden neurons will be selected to do estimation work in the next chapter for its better accuracy and simplicity. To apply the proposed ELM model for further study, the model expression is derived as:

$$V_t(k) = F(p(k)) = \sum_{i=1}^{L} \frac{\beta_i}{(1+e^{-(a_i \cdot [V_t(k-1), I(k), SOC(k)]^T + b_i)})} \tag{2.33}$$

where a_i, b_i, β_i and L have been set in Section 2.4.1.

Therefore, the discrete-time model equations describing Li-ion battery are obtained by combining (2.33) and the discrete SOC definition equation (1.2). To verify the proposed model, the initial variables are substituted into the model equations (2.33) to extract the model output. The actual battery voltage from a constant discharging current compared with the ELM model's output voltage is shown in Fig. 2.36. It verifies that the model error is quite small. Fig. 2.37 presents a comparison of the proposed model's output voltage and the measured terminal voltage of a different Samsung 2.6 Ah Li-ion battery.

The model output RMSE is 0.0165 V. The largest error is 0.0838 V. It is verified that this proposed Li-ion battery model has good accuracy.

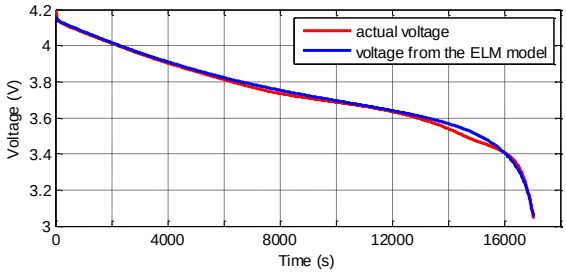

Fig. 2.36. The actual voltage and model output with constant current.

As the comparison, the model trained by RBF NN is also verified here. The RBF NN model is expressed by:

$$V_t(k) = F(p(k)) = \beta_0 + \sum_{i=1}^{10} \beta_i \cdot \exp(-\frac{\left\| [V_t(k-1), I(k), SOC(k)] - c_i \right\|^2}{\sigma_i^2}) \qquad (2.34)$$

where all the model parameters have been obtained during training. The hidden neuron number is also set as 10. Similar to the ELM model, the RBF NN model's equations are described by (2.34) and the SOC definition in equation (1.2).

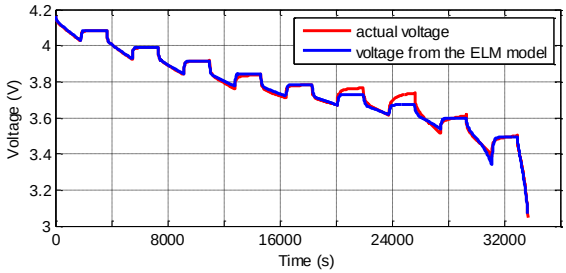

Fig. 2.37. The actual voltage and model output for another battery.

Fig. 2.38 presents a comparison of the RBF NN model's output voltage and the measured terminal voltage of the Samsung 2.6 Ah Li-ion battery used to test the ELM model in Fig. 2.37. The model output RMSE is 0.0219 V. The largest error is 0.0872 V. It indicates that the RBF NN model has a larger modeling error than that of the ELM model.

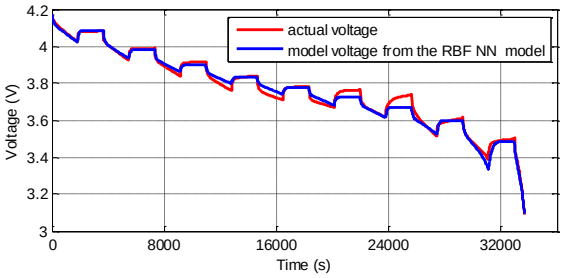

Fig. 2.38. The actual voltage and model output for the RBF NN model.

2.4.4 Li-ion Battery Modeling with the Online Sequential ELM Algorithm

In previous sections, the models for Li-ion batteries are all established off-line. Sometimes EV's energy system may need a battery model trained online. Based on the ELM model proposed in Section 2.4.1, an online trained ELM model is proposed for Li-ion batteries in this section.

In [118], an online sequential learning algorithm based on the ELM algorithm, named OS-ELM, is proposed. OS-ELM solves the problem that the input-output observations are obtained sequentially, but not in a batch. The OS-ELM algorithm trains the model's input-output mapping online. Compared with other kinds of sequential learning algorithms, OS-ELM has faster learning speed and good generalization performance [118].

The OS-ELM algorithm can learn input-output samples one-by-one or chunk-by-chunk sequentially. For Li-ion battery modeling in this section, the learning block is set to one and the model is learned with one-by-one input-output sample observation. For Li-ion battery, the utilization of OS-ELM provides possibility and improvement for the online modeling process. There is no need to know the prior knowledge of the model parameters before modeling. OS-ELM provides the online accurate and fast modeling process.

The algorithm of OS-ELM is described as follows. There are mainly two steps:

Step 1: Initialize the model parameters with some initial input-output samples. The initial training data is represented by:

$$\{(x_j, t_j) \mid x_j \in R^n, t_j \in R^m, j = 1, ..., N_0\} \tag{2.35}$$

where N_0 is the number of the initial input-output samples. There is no need to set N_0 a large set. The only demand for N_0 is $N_0 \geq L$ where L is the hidden neuron number.

The input weight a_i and the hidden neuron bias b_i are assigned randomly, where $i = 1,...,L$. It is noticed that the values of a_i and b_i are not tuned during training, which is the same to the ELM algorithm.

Then, the initial form of the hidden layer output matrix H_0 is determined as:

$$H_0 = \begin{bmatrix} G(a_1, b_1, x_1) & \cdots & G(a_L, b_L, x_1) \\ \vdots & \cdots & \vdots \\ G(a_1, b_1, x_{N_0}) & \cdots & G(a_L, b_L, x_{N_0}) \end{bmatrix}_{N_0 \times L} \tag{2.36}$$

where $G(x)$ is the activation function.

The equivalent form of the model is:

$$H_0 \beta_0 = T_0 \tag{2.37}$$

where $\beta_0 = [\beta_{10}, \beta_{20}, ..., \beta_{L0}]$ and $T_0 = [t_1, ..., t_{N0}]$. Thus, β_0 is determined by:

$$\beta_0 = (H_0^T H_0)^{-1} H_0^T T_0 \tag{2.38}$$

Set

$$M_0 = (H_0^T H_0)^{-1} \tag{2.39}$$

Step 2: It is designed that the new samples come one-by-one. Hence, when a new observation $\{(x_{k+1}, t_{k+1}), k \geq N_0\}$ arrives, the sequential learning phase is executed. A partial hidden layer output matrix is determined by:

$$H_k = [G(a_1, b_1, x_{k+1}) \cdots G(a_L, b_L, x_{k+1})] \tag{2.40}$$

Then, the output weight $\beta_{i(k+1)}$ is calculated by:

$$M_{k+1} = M_k - \frac{M_k H_{k+1} H_{k+1}^T M_k}{1 + H_{k+1}^T M_k H_{k+1}} \tag{2.41}$$

$$\beta_k = \beta_k + M_{k+1} H_{k+1} (t_{k+1}^T - H_{k+1}^T \beta_k) \tag{2.42}$$

Then set $k = k + 1$ and execute step 2 until the training process ends.

The same model structure in Fig. 2.30 is designed for the OS-ELM trained Li-ion battery model. Thus, in (2.35), $n=3$ and $m=1$. $\tilde{L}$ is set to 5. The initial training data amount is set to $N_0=75$. It is noted that there is no need to know the number of samples before training. The activation function $G(x)$ is also defined the sigmoid function:

$$G(a_i,b_i,x_j)=(1+e^{-(a_i\cdot x_j+b_i)})^{-1}, i=1,...L,\ j=1,... \tag{2.43}$$

A battery experiment with various discharging currents is executed to test the online modeling algorithm. The data sampling interval is set to 3 s. The SOC value is also calculated by the Coulomb counting method in experimental conditions. The input-output samples arrive sequentially and the battery model is trained with the new arriving observation after each sampling step. Fig. 2.39 shows the training results for the Li-ion battery model compared with the measured terminal voltage. The training accuracy represented by RMSE for the testing samples is 0.0135 V. It verifies that the OS-ELM algorithm trains the Li-ion battery model with good performance. Therefore, an online battery model is realized by the OS-ELM algorithm.

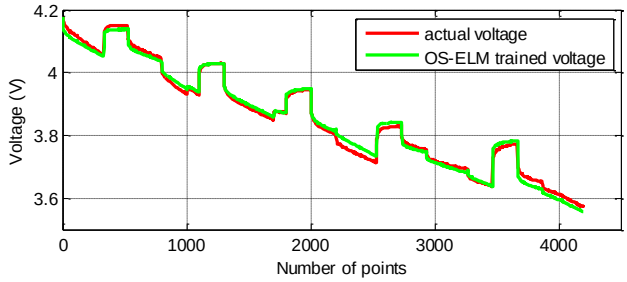

Fig. 2.39. The actual voltage and model output from the OS-ELM model.

2.5 Summary

In this chapter, Li-ion battery modeling is investigated and improved. The equivalent circuit model including the parallel circuit model and series circuit model are reviewed and established for Li-ion batteries. By model output comparison, it is verified that the series circuit model with two RC networks has good performance. The temperature effect on Li-ion battery behaviors is also considered. A fuzzy model based on equivalent circuit model considering temperature and SOC effect is established. This new model describes the ambient temperature effect on Li-ion battery clearly with good accuracy. Li-ion battery's surface temperature variation during operation is also tested here, verifying that

it is reasonable to exclude temperature effect when the battery operates in the same ambient temperature. Thus, in later chapters of this thesis, the temperature effect is not considered and all the experiments are under room temperature. Then, the NN model which is suitable for simple current pattern is applied and improved in experimental conditions in this chapter. Trained by the ELM algorithm, the proposed ELM model has a simple modeling process and high accuracy compared with those of the RBF NN model. Finally, an online trained battery model using OS-ELM is proposed and good modeling performance is achieved.

Based on various types of Li-ion battery models, several estimation algorithms corresponding to different focusing points will be applied to do SOC estimation in the following chapters. EMS's practical needs will be considered. Besides, when studying other EMS topics in this thesis, the models established in this chapter will also be applied to simulate or supervise the batteries. In the next chapter, the proposed ELM model will be used to do SOC estimation using KF-based algorithms.

Chapter 3 Li-ion Battery SOC Estimation Based On the ELM Model Using Kalman Filter Methods

In this chapter, the topic of Li-ion battery state of charge (SOC) estimation will be discussed. This chapter aims at SOC estimation using the widely-used methods of Kalman filter (KF)-based algorithms. Section 3.1 gives a rough introduction for the estimation methods used in this chapter. In Section 3.2, various KF-based algorithms are described in detail. Section 3.3 gives the system state space equations for Li-ion batteries using the ELM model. In Section 3.4, estimation results are compared and discussed. Section 3.5 concludes this chapter.

3.1 Introduction

SOC reflects Li-ion battery's remaining energy and present operation status. The energy management system (EMS) in electric vehicles (EVs) supervises Li-ion batteries and controls the batteries' charging and discharging referring to SOC. Thus, accurate SOC estimation for Li-ion batteries is necessary and important. With models focusing on different aspects, various estimation methods are applied in this chapter and the later chapters to obtain the estimated SOC for Li-ion batteries.

The proposed discrete Li-ion battery's ELM model in Chapter 2 has simple structure that is convenient to do estimation. This chapter aims at SOC estimation based on this model. As the unmeasured quantity of battery, SOC is defined as one state in the battery model system. SOC estimation could lead to filtering problem since it is to estimate system hidden variable as a set of online observations [56]. For the system with Gaussian noise, KF is an optimal selection. KF is a powerful estimation tool with good performance and simple implementation. KF or its variants are able to do estimation for linear or nonlinear systems. In this chapter, with the Li-ion battery's ELM model, several estimation algorithms based on KF, including extended Kalman filter (EKF), unscented Kalman filter (UKF), adaptive EKF (AEKF) and adaptive UKF (AUKF), are applied and compared for SOC estimation.

3.2 KF Variants

The KF theory for estimating a dynamic linear system with discrete data's unknown state variables using the measurements is first proposed in [123]. The algorithm includes a series of mathematical equations to provide the estimated state that minimized the mean of the squared error. Optimal estimation could be achieved with this recursive method. Compared with other kinds of estimation technologies, no convergence proof is needed. The filter design process is significantly simplified.

The KF algorithm mainly has two steps [124]: the predicting process and the updating process. Define a linear dynamic system with discrete-time state-space equations as (3.1) and (3.2):

$$x_k = Ax_{k-1} + Bu_{k-1} + \omega_{k-1} \tag{3.1}$$

$$z_k = Cx_k + \upsilon_k \tag{3.2}$$

where $x_k \in \Re^n$ is the state vector and $z_k \in \Re^m$ is the system output at sampling step k; $u_k \in \Re^p$ is the input to the system; $A \in \Re^{n\times n}$, $B \in \Re^{n\times p}$, and $C \in \Re^{m\times n}$ are constant matrices; and $\omega_k \in \Re^n$ and $\upsilon_k \in \Re^m$ represent the process and measurement noises. It is defined that ω_k and υ_k are uncorrelated white Gaussian noise with zero mean and constant covariance. The probability distributions are:

$$p(\omega) \sim N(0,Q)\,,\ p(v) \sim N(0,R) \tag{3.3}$$

where Q and R are the covariance matrices.

KF's operation schematic including the mathematical expressions is shown in Fig. 3.1. The two steps are executed concurrently to achieve the estimation for the state vector. K_k is the Kalman gain matrix. $\hat{x}_k^-$ is defined as the *a priori* state estimate before the measurement z_k is taken. $\hat{x}_k$ is defined as the *a posteriori* state estimate at step k given the knowledge of z_k . P_k^- and P_k are the *a priori* estimate error covariance and *a posteriori* estimate error covariance. The state vector is initialized in (3.4) and (3.5) with the mean of $\hat{x}_0$ and error covariance of P_0 before taking the estimation steps:

$$\hat{x}_0 = E[x_0] \tag{3.4}$$

$$P_0 = E[(x_0 - \hat{x}_0)(x_0 - \hat{x}_0)^T] \tag{3.5}$$

As stated in Chapter 2, the Li-ion battery model is generally nonlinear. Hence, the linear form filter of KF is not suitable for Li-ion battery estimation. Some nonlinear and improved versions of KF are described and applied in the following sections.

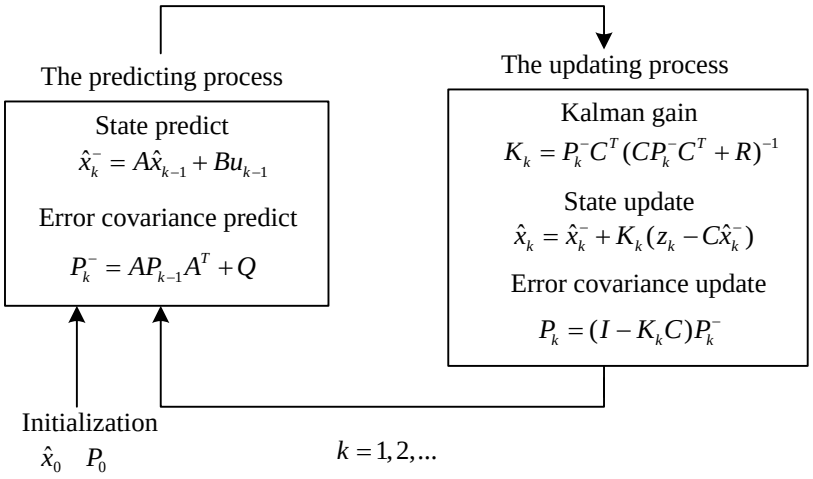

Fig. 3.1. KF operation schematic.

3.2.1 Extended Kalman Filter

As the nonlinear version of KF, EKF is developed based on the KF technique to do estimation for nonlinear dynamic systems. A linearization process is used to approximate the nonlinear system at every step. Define a nonlinear system as:

$$x_k = f(x_{k-1}, u_k) + \omega_{k-1} \tag{3.6}$$

$$z_k = h(x_k, u_k) + \upsilon_k \tag{3.7}$$

where x_k, z_k, and u_k have the same definitions as in (3.1) and (3.2); ω_k and υ_k have the same distributions as (3.3); and $f(\cdot)$ and $h(\cdot)$ represent the nonlinear state transition and measurement functions. Before taking estimation, the state vector is initialized as (3.4) and (3.5).

The EKF algorithm has similar operation steps as shown in Fig. 3.1. The mathematical equations are described as follows:

1) The predicting process:

$$\begin{cases} \hat{x}_k^- = f(\hat{x}_{k-1}, u_{k-1}) \\ P_k^- = A_{k-1} P_{k-1} A_{k-1}^T + Q \end{cases} \tag{3.8}$$

2) The updating process:

$$\begin{cases} K_k = P_k^- H_k^T (H_k P_k^- H_k^T + R)^{-1} \\ \hat{x}_k = \hat{x}_k^- + K_k (z_k - h(\hat{x}_k^-, u_k)) \\ P_k = (I - K_k H_k) P_k^- \end{cases} \tag{3.9}$$

In (3.8) and (3.9), A_k and H_k are the Jacobian matrices of the partial derivatives of $f(x,u)$ and $h(x,u)$ with respect to *x*, expressed by: $A_{k-1} = \frac{\partial f}{\partial x}|_{x=\hat{x}_{k-1}}$, $H_k = \frac{\partial h}{\partial x}|_{x=\hat{x}_k^-}$.

The EKF algorithm is widely used for nonlinear system's estimation. At each time step, $f(x_{k-1}, u_k)$ and $h(x_k, u_k)$ are linearized around the operation point by a first-order Taylor-series expansion [30]. However, EKF relies on this linearization process to update the state mean and covariance [36]. Inaccurate estimation and divergence may be caused for the systems with stronger nonlinearity.

3.2.2 Unscented Kalman Filter

The EKF algorithm may diverge when the higher order terms become significant for the nonlinear model. The approximation error between the original system and the linearized model may bring significant estimation error when a large initial state error or system noise exists [53]. To improve SOC estimation performance for nonlinear battery model, the UKF algorithm is investigated in this section.

To overcome the shortcomings of EKF, the UKF algorithm based on unscented transformation (UT) is proposed and developed [125]. UT is a method of nonlinear transformation for approximating the probability distribution of a random variable. Hence, UKF propagates the state mean and covariance information through a nonlinear transformation directly instead of doing linearization [125, 126]. There is no need to calculate Jacobian matrices and the linearization error is decreased. Compared with EKF, UKF calculates the mean and covariance to the second order [127]. As an alternative

nonlinear extension, UKF could provide better estimation than EKF.

The mathematical equations of UKF are shown on the discrete nonlinear system described in (3.6) and (3.7). It should be noticed that the state vector's dimension is represented by n_x here. The initialization step in (3.4) and (3.5) is also executed before estimation. The UKF algorithm also includes the predicting process and the updating process. The details are described as follows:

1) The predicting process:

a) Computing sigma points:

At time step $k-1$, it has been defined that the state estimate has mean $\hat{x}_{k-1}$ and error covariance P_{k-1}. A set of $2n_x+1$ weighted samples named sigma points are selected at time step $k-1$ as shown in (3.10):

$$\begin{cases} \tilde{\chi}_{k-1}^{(i)} = \hat{x}_{k-1}, i=0 \\ \tilde{\chi}_{k-1}^{(i)} = \hat{x}_{k-1} + (\sqrt{(n_x+\lambda)P_{k-1}})_i,\ i=1,...,n_x \\ \tilde{\chi}_{k-1}^{(i)} = \hat{x}_{k-1} - (\sqrt{(n_x+\lambda)P_{k-1}})_i,\ i=n+1,...,2n_x \end{cases} \tag{3.10}$$

where $\tilde{\chi}_{k-1}^{(i)}$ represents the sigma points, and λ is a scaling factor determined by $\lambda=\alpha^2(n+\kappa)-n_x$. The constant α is set to a small positive value. It determines the spread of the sigma points around $\hat{x}_{k-1}$. κ is the secondary scaling parameter usually set to 0 or $3-n_x$ [125]. The expression of $(\sqrt{(n_x+\lambda)P_{k-1}})_i$ represents the *ith* column of the matrix square root of $(n_x+\lambda)P_{k-1}$. Define the mean weights W_{m} associated with the sigma points as:

$$\begin{cases} W_m^{(i)} = \dfrac{\lambda}{\lambda+n_x}, i=0 \\ W_m^{(i)} = \dfrac{\lambda}{2(\lambda+n_x)}, i=1,...,2n_x \end{cases} \tag{3.11}$$

b) Propagating sigma points:

Propagate each sigma point through the nonlinear state transition function:

$$\bar{\chi}_{k|k-1}^{(i)} = f(\tilde{\chi}_{k-1}^{(i)}, u_{k-1}) \tag{3.12}$$

c) Determining the *a priori* state estimate and the *a priori* estimate error covariance:

The *a priori* state estimate $\hat{x}_{k|k-1}$ at time instant $k|k-1$ is computed by:

$$\hat{x}_{k|k-1} = \sum_{i=0}^{2n} W_m^{(i)} \bar{\chi}_{k|k-1}^{(i)} \tag{3.13}$$

To obtain the *a priori* estimate error covariance $P_{k|k-1}$, define the variance weights W_c as:

$$\begin{cases} W_c^{(i)} = \dfrac{\lambda}{\lambda + n_x} + (1 - \alpha^2 + \beta), i = 0 \\ W_c^{(i)} = \dfrac{\lambda}{2(\lambda + n_x)}, i = 1, ..., 2n_x \end{cases} \tag{3.14}$$

where β is used to incorporate part of the prior knowledge of the distribution of state estimate [128]. For Gaussian distributions, β is usually set to 2 to achieve optimal estimation. Then,

$$P_{k|k-1} = \sum_{i=0}^{2n} W_c^{(i)} (\bar{\chi}_{k|k-1}^{(i)} - \hat{x}_{k|k-1})(\bar{\chi}_{k|k-1}^{(i)} - \hat{x}_{k|k-1})^T + Q \tag{3.15}$$

2) The updating process:

a) Computing sigma points:

At time instant $k|k-1$, a new set of sigma points, $\tilde{\chi}_{k|k-1}^{(i)}$, based on the *a priori* state estimate $\hat{x}_{k|k-1}$ is selected as (3.16):

$$\begin{cases} \tilde{\chi}_{k|k-1}^{(i)} = \hat{x}_{k|k-1}, i = 0 \\ \tilde{\chi}_{k|k-1}^{(i)} = \hat{x}_{k|k-1} + (\sqrt{(n_x + \lambda) P_{k|k-1}})_i, i = 1, ...n_x \\ \tilde{\chi}_{k|k-1}^{(i)} = \hat{x}_{k|k-1} - (\sqrt{(n_x + \lambda) P_{k|k-1}})_i, i = n_x + 1, ..., 2n_x \end{cases} \tag{3.16}$$

b) Computing predicted output:

Compute the corresponding output for each sigma point through the measurement function:

$$\tilde{Y}_{k|k-1}^{(i)} = h(\tilde{\chi}_{k|k-1}^{(i)}, u_k) \tag{3.17}$$

Then, the predicted output is determined by:

$$\hat{Y}_{k|k-1} = \sum_{i=0}^{2n} W_m^{(i)} \tilde{Y}_{k|k-1}^{(i)} \tag{3.18}$$

c) Computing the Kalman gain K_k :

$$\begin{cases} P_{y_k y_k} = \sum_{i=0}^{2n} W_c^{(i)} (\tilde{Y}_{k|k-1}^{(i)} - \hat{Y}_{k|k-1})(\tilde{Y}_{k|k-1}^{(i)} - \hat{Y}_{k|k-1})^T + R \\ P_{x_k y_k} = \sum_{i=0}^{2n} W_c^{(i)} (\tilde{\chi}_{k|k-1}^{(i)} - \hat{x}_{k|k-1})(\tilde{Y}_{k|k-1}^{(i)} - \hat{Y}_{k|k-1})^T \end{cases} \tag{3.19}$$

where $P_{y_k y_k}$ represents the filter covariance of the predicted output at time instant $k|k-1$, and $P_{x_k y_k}$ represents the filter cross-covariance between the predicted output and the state at time instant $k|k-1$. Then,

$$K_k = P_{x_k y_k} P_{y_k y_k}^{-1} \tag{3.20}$$

d) Determining *a posteriori* state estimate $\hat{x}_k$ and *a posteriori* estimate error covariance P_k:

At time step *k*, given the output measurement z_k, the state estimate and error covariance are obtained by:

$$\begin{cases} \hat{x}_k = \hat{x}_{k|k-1} + K_k (z_k - \hat{Y}_{k|k-1}) \\ P_k = P_{k|k-1} - K_k P_{y_k y_k} K_k^T \end{cases} \tag{3.21}$$

3.2.3 Adaptive Extended Kalman Filter and Adaptive Unscented Kalman Filter

Considering Li-ion battery's dynamic characteristics, some improvement is developed on EKF and UKF to obtain better SOC estimation and reduce the probability of divergence. In (3.3), the process and measurement noise covariance matrices *Q* and *R* are defined constant. In previous sections, it has been shown that EKF and UKF are suitable for the system with constant covariance noises. It is stated in [129] that the optimality of KF's estimation depends on the quality of the prior knowledge about system noise statistics. Hence, a proper selection of *Q* and *R* is essential to the filter estimation performance.

Improper Q and R may lead to large estimation error or filter divergence. The classical method to determine the two covariance matrices is through empirical analysis on the system and measurement errors or manually tuning with the trail and error method. It is obvious that such methods cost much time and the selected Q and R are not guaranteed to have suitable values. On the other hand, these filter parameters may change while the filter is working. To compensate for unknown or time-varying Q and R, the adaptive filter algorithm is utilized to achieve better estimation performance.

The adaptive technique is developed on EKF and UKF, constituting adaptive nonlinear Kalman filters. The adaptive Kalman filtering algorithm updates the system noise statistical information online. The main advantage of adaptive Kalman filter is to achieve less reliance on the prior statistical information and to adapt the noise covariance matrices according to filter learning history [52]. Therefore, building on the descriptions of EKF and UKF, the algorithms of AEKF and AUKF are described in this section to apply better estimation on Li-ion battery system.

In [130], the AEKF and AUKF algorithms are proposed. Compared with conventional EKF and UKF, such adaptive Kalman filtering algorithms add an online adjustment block to adapt the filter parameters Q and R. In each step, after achieving the state estimate, Q and R are updated according to the system information and measurement variation. With this method, Q and R can be tuned to the optimal value during estimation. The adaptive filtering technique of covariance matching using residual covariance matrix is utilized here. The elements of the residual-based covariance matrix should be matched to their theoretical form [131]. The residual covariance matrix at step k is represented as C_k, calculated by:

$$C_k = \frac{\sum_{j=k-N+1}^{k} \mu_j \mu_j^T}{M} \tag{3.22}$$

where M defines the window size for covariance matching [52, 132], and μ_k defines the residual sequence representing the difference between the *kth* real measurement and the predicted measurement computed by $h(\hat{x}_k, u_k)$ with the filter's state estimation:

$$\mu_k = z_k - h(\hat{x}_k, u_k). \tag{3.23}$$

The AEKF algorithm adds the following adjusting block (3.24) and (3.25) to the EKF algorithm (3.8)-(3.9):

$$Q_k = K_k C_k K_k^T \tag{3.24}$$

$$R_k = C_k + H_k P_k H_k{}^T \tag{3.25}$$

For the AUKF algorithm, the adjusting block (3.26) with (3.24) is added to the UKF algorithm (3.10)-(3.21):

$$R_k = \sum_{i=0}^{2n_x} W_c^{(i)} \left(\tilde{Y}_{k|k-1}^{(i)} - h(\hat{x}_k, u_k)\right)\left(\tilde{Y}_{k|k-1}^{(i)} - h(\hat{x}_k, u_k)\right)^T + C_k \,. \tag{3.26}$$

In (3.24)-(3.26), the Kalman gain matrix K_k has been obtained from the updating step of conventional EKF and UKF. The system noise covariance matrices of Q and R are not constant anymore. Q_k and R_k are updated every time step when a new measurement z_k is taken. Thus, Q_k and R_k are adaptive to the real-time system information. If the prior knowledge of the system noise statistics is not accurate, the effect on the estimation performance will be reduced significantly. Better performance during estimation and convenience on state vector initialization are brought by the AEKF and AUKF algorithms described above. Meanwhile, no complex mathematical operation is added by AEKF and AUKF.

To describe the adaptive Kalman filtering procedure clearly, the operation schematic of AUKF is depicted in Fig. 3.2. It shows that the adjustment block is also executed recursively with conventional Kalman filter algorithms. Before the estimation procedure, the parameters of Q, R and M should be initialized.

With AEKF and AUKF, the process and measurement noise covariance matrices are adapted to the residual sequences step by step. Therefore, their state estimation performances do not depend much on the initial values of Q and R. The initial filter parameters can be selected simply.

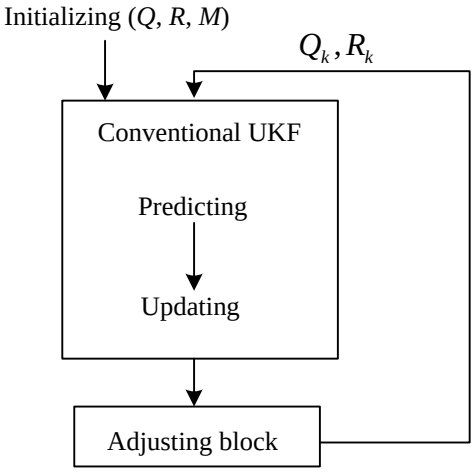

Fig 3.2 The operation schematic for AUKF.

3.3 System State Space Equations

Before taking the estimation algorithms stated in previous sections, the discrete-time state-space equations for the Li-ion battery model should be defined first. The proposed ELM model in Section 2.4.3 is applied to do SOC estimation here. The RBF NN model trained in Section 2.4.3 is also estimated as a comparison. As the variable to be estimated, the *SOC* value at the *kth* sampling step, $SOC(k)$, is taken as one of the state variables of the model's state-space equations. The other state variable $V_t(k-1)$ is defined by equation (2.31). Thus, the state vector is defined by:

$$x_k = [x_1(k) \;\; x_2(k)]^T = [V_t(k-1) \;\; SOC(k)]^T . \tag{3.27}$$

From the model equations, the state-space equations and output equations are expressed by (3.28) and (3.29):

$$\begin{bmatrix} V_t(k) \\ SOC(k+1) \end{bmatrix} = \begin{bmatrix} F(p(k)) \\ SOC(k) - \dfrac{\Delta t}{C_n} I(k) \end{bmatrix} + \begin{bmatrix} \omega_1(k) \\ \omega_2(k) \end{bmatrix} \tag{3.28}$$

$$\begin{bmatrix} z_1(k) \\ z_2(k) \end{bmatrix} = \begin{bmatrix} F(p(k)) \\ V_t(k-1) \end{bmatrix} + \begin{bmatrix} v_1(k) \\ v_2(k) \end{bmatrix} \tag{3.29}$$

where $[V_t(k) \;\; SOC(k+1)]^T = \left[x_1(k+1) \;\; x_2(k+1)\right]^T$; $[z_1(k) \;\; z_2(k)]^T$ represents the measurements of $[V_t(k) \;\; V_t(k-1)]^T$; $[\omega_1(k) \;\; \omega_2(k)]^T = \omega(k)$ and $[v_1(k) \;\; v_2(k)]^T = v(k)$.

The functions of $F(p(k))$ and $SOC(k)-\frac{\Delta t}{C_n}I(k)$ describe the battery model. The current $I(k)$ is defined as the system input u_k. The vectors $\omega(k)$ and $v(k)$ express the process noise and measurement noise defined as zero-mean white Gaussian noises.

The system equations (3.28) and (3.29) have nonlinear form. The state transition function $f(x,u)$ and the measurement function $h(x,u)$ are defined as

$$f(x_k,u_k)=\begin{bmatrix} F(p(k)) \\ SOC(k)-\frac{\Delta t}{C_n}I(k) \end{bmatrix},\ h(x_k,u_k)=\begin{bmatrix} F(p(k)) \\ V_t(k-1) \end{bmatrix}, \tag{3.30}$$

where $F(p(k))$ represents the ELM model or RBF NN model. The nonlinear estimation techniques described in the last section are applied to the system state-space equations in the next section.

3.4 SOC Estimation From Experiment and Comparison

EKF is executed on the ELM model to do SOC estimation. To verify the ELM model's performance on estimation, the RBF NN model is also estimated by EKF as a comparison. For the system equations (3.28) and (3.29), define the Jacobian matrices of A_k and H_k expressed by

$$A_{k-1}=\frac{\partial f}{\partial x}|_{x=\hat{x}_{k-1}}=\begin{bmatrix} \frac{\partial F(p(k))}{\partial x_k} \\ 0 \quad 1 \end{bmatrix}|_{x=\hat{x}_{k-1}},\ H_k=\frac{\partial h}{\partial x}|_{x=\hat{x}_k^-}=\begin{bmatrix} \frac{\partial F(p(k))}{\partial x_k} \\ 1 \quad 0 \end{bmatrix}|_{x=\hat{x}_k^-}. \tag{3.31}$$

For the ELM model, it is derived from (2.33) that:

$$\frac{\partial F(p(k))}{\partial x_k}=\sum_{i=1}^{10}\frac{\beta_i\cdot a_i\cdot(1+e^{-(a_i\cdot p(k)+b_i)})}{(1+e^{-(a_i\cdot p(k)+b_i)})^2}\cdot\frac{\partial p(k)}{\partial x_k} \tag{3.32}$$

where $\frac{\partial p(k)}{\partial x_k}=\begin{bmatrix} 1 & 0 \\ 0 & 0 \\ 0 & 1 \end{bmatrix}$.

For the RBF NN model, the Jacobian matrices are derived from (2.34) as:

$$\frac{\partial F(p(k))}{\partial x_k} = \sum_{i=1}^{10} \frac{-2\beta_i}{\sigma_i^2} \exp(-\frac{1}{\sigma_i^2} \| p(k) - c_i \|) \cdot (p(k) - c_i)^T \cdot \frac{\partial p(k)}{\partial x_k} \tag{3.33}$$

where $\frac{\partial p(k)}{\partial x_k} = \begin{bmatrix} 1 & 0 \\ 0 & 0 \\ 0 & 1 \end{bmatrix}$.

The pulse current experimental data for the Li-ion battery model test in Section 2.4.3 is used to test the EKF algorithm. The current pattern is shown as Fig. 2.32. The initial SOC for estimation is set to 1, the same to the actual initial SOC value. The filter parameters are set as: $P_0 = \begin{bmatrix} 0.001 & 0 \\ 0 & 0.001 \end{bmatrix}$, $Q = \begin{bmatrix} 0.001 & 0 \\ 0 & 0.000001 \end{bmatrix}$, and $R = \begin{bmatrix} 0.01 & 0 \\ 0 & 0.01 \end{bmatrix}$. Here, Q and R are constant matrices. Then, EKF is applied on the two models. The estimation results for the two state variables including SOC and $V_t(k-1)$ for the two models are shown in Figs. 3.3 and 3.4. It indicates that EKF provides good SOC estimation results for both models when the initial SOC is at its real value. The SOC errors as the difference between the actual and estimation SOC results are computed. The largest SOC errors during estimation for the two models are both smaller than 3.5%. The estimated terminal voltage $V_t(k-1)$ is also similar to the measured battery terminal voltage.

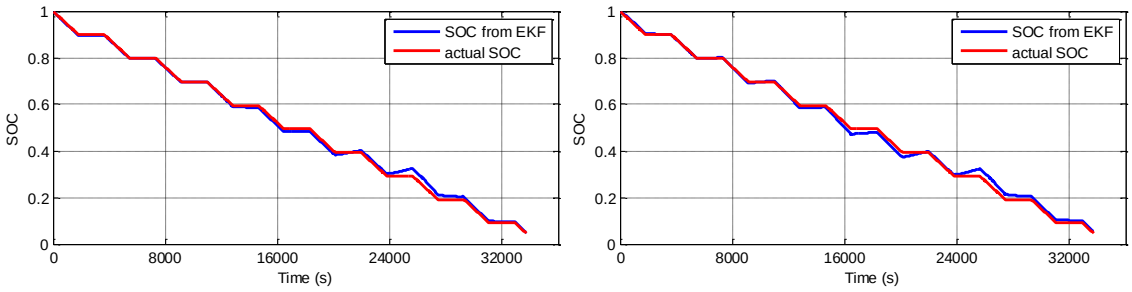

a) The ELM model. b) The RBF NN model.

Fig. 3.3. SOC estimation results from EKF compared with actual SOC.

The SOC estimation errors from the ELM and RBF NN model are depicted and compared in Fig. 3.5. It shows that the SOC error from RBF NN model is larger than the ELM model in most SOC regions. In addition, the computational time for estimation of RBF

NN model is 0.4992 s, which is 1.6 times to the ELM model, 0.3120 s. It indicates that the ELM model has a simpler estimation procedure with EKF than the RBF NN model.

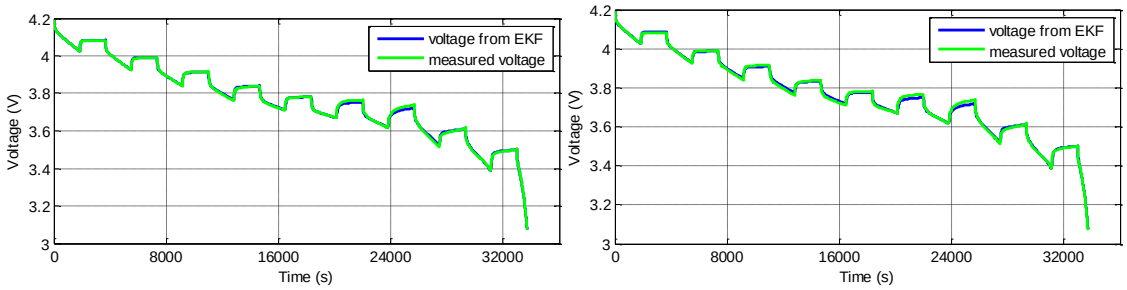

a) The ELM model. b) The RBF NN model.

Fig. 3.4. Voltage estimation results from EKF compared with actual terminal voltage.

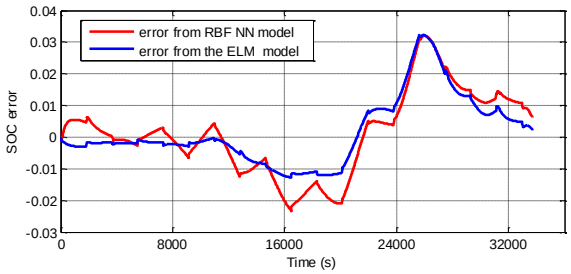

Fig. 3.5. SOC error comparison between the ELM model and RBF NN model.

In EV applications, the accurate knowledge of the Li-ion battery's initial SOC may be hard to know. Therefore, the estimation algorithms must be robustly insensitive to the initial state value. After getting the results stated above, SOC estimation on the ELM model by EKF with inaccurate initial SOC is tested. The initial SOC is set to an incorrect value with the initial error of 0.25. The same experiemental data is tested. The SOC estimation results and errors from EKF for the ELM model are shown in Fig. 3.6. It reveals that EKF is robust to the initial SOC. The estimation converges to the actual value after some steps. The largest SOC error stays smaller than 3.5% after convergence. However, the converging process takes long time. It takes about 700 s, i.e. more than 10 mins for SOC error to reach in the range of 5%. In EV applications, the energy system needs a faster convergence rate. More than 10 mins is a bit long for EVs during driving. Thus, a faster convergence rate is needed in this case.

Then, UKF is applied on the ELM model to test whether better SOC estimation and robustness can be achieved. Here, the state vector's dimension n_x is 2. Thus, $2n_x+1=5$ sigma points should be determined. The initial SOC is also set to the incorrect value of 0.75. The filter parameters for UKF are also set as: $P_0=\begin{bmatrix}0.001 & 0\\ 0 & 0.001\end{bmatrix}$, $Q=\begin{bmatrix}0.001 & 0\\ 0 & 0.000001\end{bmatrix}$, and $R=\begin{bmatrix}0.01 & 0\\ 0 & 0.01\end{bmatrix}$. The SOC estimation results and errors from UKF for the ELM model are shown in Fig. 3.7. It displays similar estimation performance to EKF. The estimation error also converges to the range of 5% after nearly 700 s.

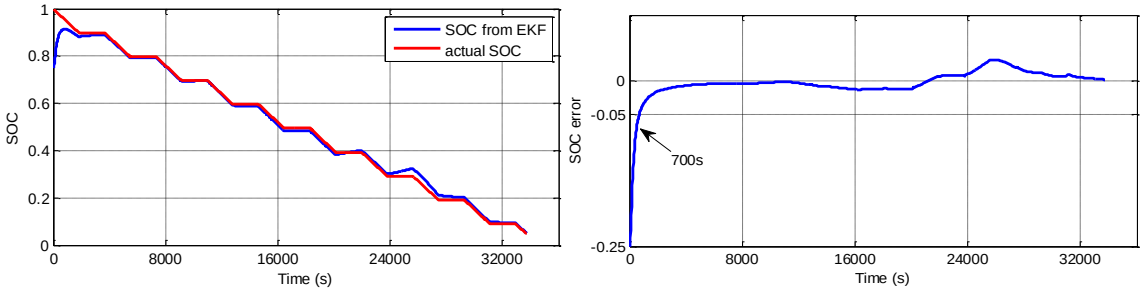

a) SOC estimation compared with actual SOC. b) SOC error.

Fig. 3.6. SOC estimation from EKF with incorrect initial SOC.

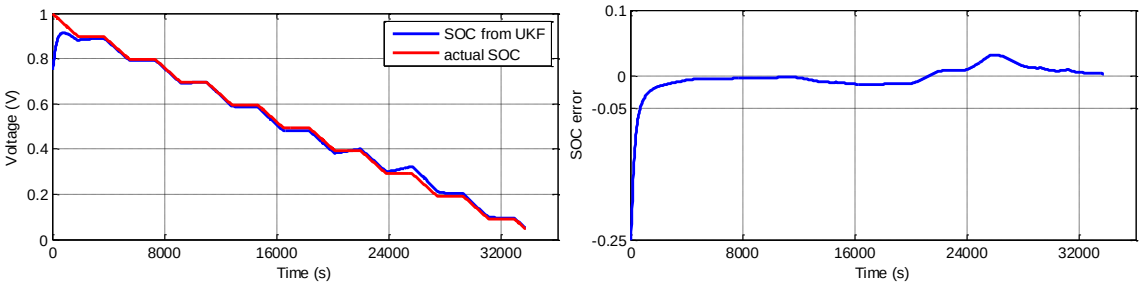

a) SOC estimation compared with actual SOC. b) SOC error.

Fig. 3.7. SOC estimation results from UKF.

To achieve more improvement on SOC estimation, the adaptive Kalman filters including AEKF and AUKF are applied on the ELM model. The filter parameters for AEKF and AUKF are also initialized to $P_0=\begin{bmatrix}0.001 & 0\\ 0 & 0.001\end{bmatrix}$, $Q=\begin{bmatrix}0.001 & 0\\ 0 & 0.000001\end{bmatrix}$, and

$R = \begin{bmatrix} 0.01 & 0 \\ 0 & 0.01 \end{bmatrix}$, the same parameters designed for EKF and UKF. Here, Q and R are the initial values of the system noise covariance matrices and they will be adjusted during the estimation process. The window size M is set to 100 for AEKF and AUKF.

In this way, some more tests are executed and a comprehensive comparison is taken for the SOC estimation results from all the four algorithms. Battery SOC estimation of the range $SOC \in [0.8, 0.05]$ for the ELM battery model is tested. In order to verify the performance and robustness of the algorithms, the initial SOC is set to 0.4, which is different from the correct initial value, 0.8.

The comparison of SOC estimation errors for the four algorithms, EKF, UKF, AEKF and AUKF are shown in Fig. 3.8. It is obvious that AEKF and AUKF have much better state estimation accuracy than UKF and EKF. The estimation errors from AEKF and AUKF after convergence are smaller than 1.5%, much smaller than the errors from EKF and UKF. For both AEKF and AUKF algorithms, the estimation converges to the actual SOC in very few steps, performing much quicker convergence rate than EKF and UKF. In Fig. 3.9, a clear comparison of SOC estimation error between AEKF and AUKF is depicted, indicating that AUKF achieves smaller error. In conclusion, the algorithm of AUKF has the best performance in SOC estimation compared with the other three algorithms.

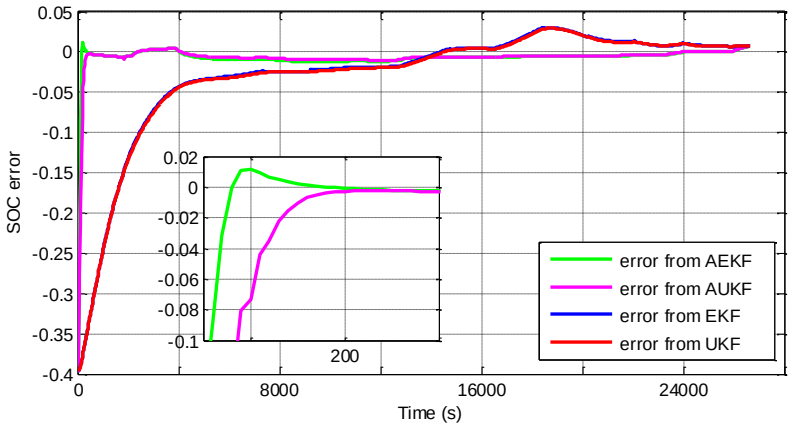

Fig. 3.8. SOC errors for the four algorithms.

Then, in order to test the adaptive Kalman filtering algorithms more comprehensively, SOC estimation results from a different Samsung 2.6 Ah battery with the same ELM

model are described. The actual SOC is from 1 to 0.05. The initial SOC of 1 is tested for AUKF. The SOC estimation results are shown in Fig. 3.10. It is obvious that the estimated SOC has good accuracy. Then, the initial SOC is also set to a different value of 0.75. The SOC estimation comparison for the four algorithms is shown in Fig. 3.11. The results are similar to Fig. 3.8 in the entire SOC range. To depict the AUKF algorithm's performance clearly, the estimation results of AUKF are shown in Figs. 3.12-3.14. The estimated SOC and SOC errors are depicted in Figs. 3.12-3.13. It verifies that the SOC estimation results from AUKF lead to a high accuracy. The largest estimation error is smaller than 0.5%. As shown in Fig. 3.14, the SOC error achieves smaller than 5% after 140 s. Compared with conventional EKF, the convergence rate improves significantly. The estimation results from AUKF for the other state, $V_t(k-1)$, compared with the measured terminal voltage and the ELM model output voltage, are depicted in Fig. 3.14. It is obvious that the estimated voltage is very close to the ELM model's output voltage. Therefore, AUKF's adjusting effect on the system during estimation is verified.

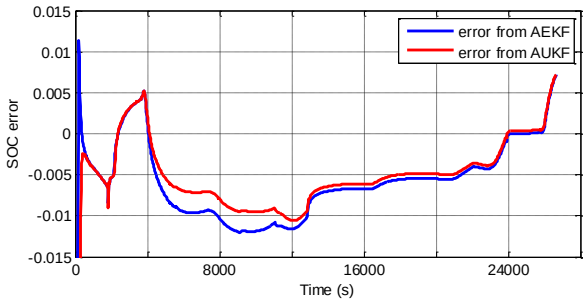

Fig. 3.9. SOC errors from AEKF and AUKF.

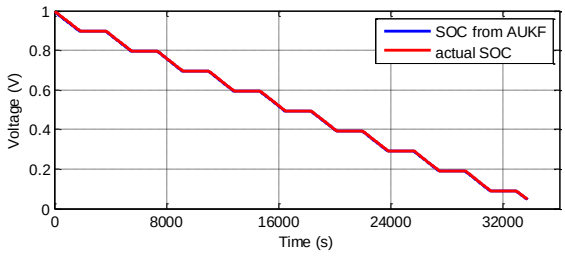

Fig. 3.10. SOC estimation from AUKF.

Furthermore, to test that whether the ELM model's performance on estimation by AUKF is still better than the RBF NN model, more comparisons are taken for the estimation process. In [25], the RBF NN model for Li-ion battery is established and SOC estimation results

from AEKF are obtained. Here, the RBF NN model is also used to do SOC estimation with AUKF. The same RBF NN model tested for EKF is used here. Then, the AUKF algorithm is applied. The estimated state variables of SOC and $V_t(k-1)$ are shown in Fig. 3.15. The SOC estimation error from the RBF NN model compared with the error from the ELM model is shown in Fig. 3.16. The error from RBF NN model is obviously larger than that of the ELM model. Moreover, the computational time of the estimation process for the ELM model is 0.6049 s, whereas the time for the RBF NN model is 0.7258 s at 1.2 times that of the ELM model. Considering the EKF estimation computational time comparison for the two models, the ELM model improves the estimation speed from 20% to 60% compared to that of the RBF NN model. It reveals a lighter computational load for the ELM model for SOC estimation. Therefore, the performance of SOC estimation is improved by the ELM model with a higher accuracy and a lighter computational load. In general, the application of AUKF on the ELM model improves SOC estimation accuracy, robustness and reduces the computational load.

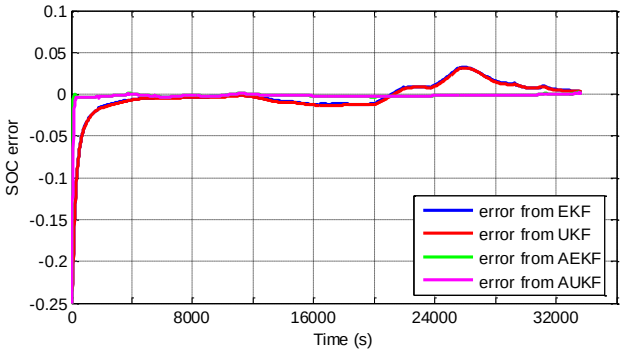

Fig. 3.11. SOC errors from EKF, UKF, AEKF and AUKF.

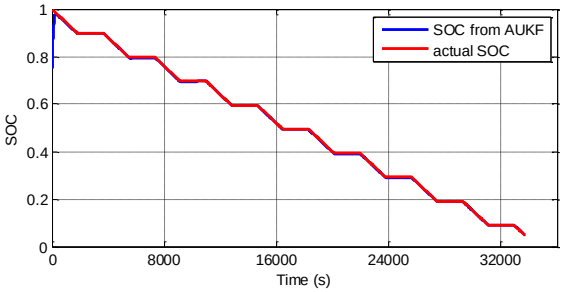

Fig. 3.12. SOC estimation from AUKF for the ELM model.

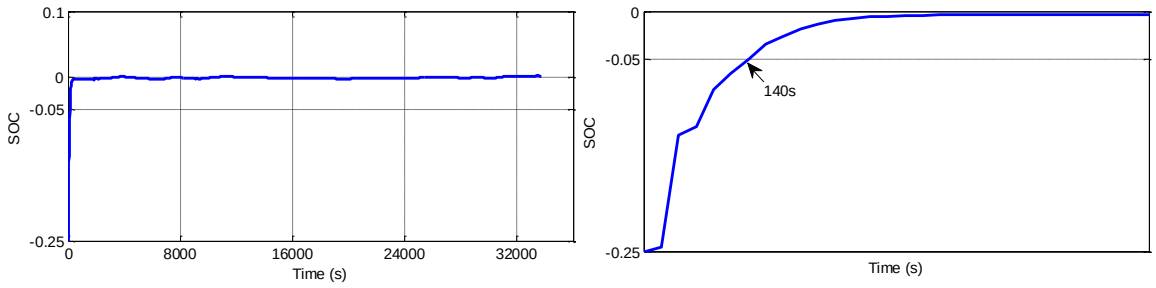

a) SOC error. b) The convergence time.

Fig. 3.13. SOC error from AUKF.

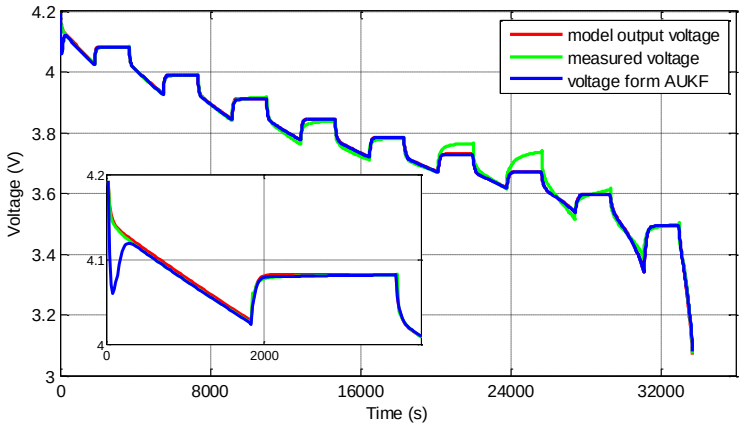

Fig. 3.14. Estimated voltage from AUKF compared with model voltage and actual voltage.

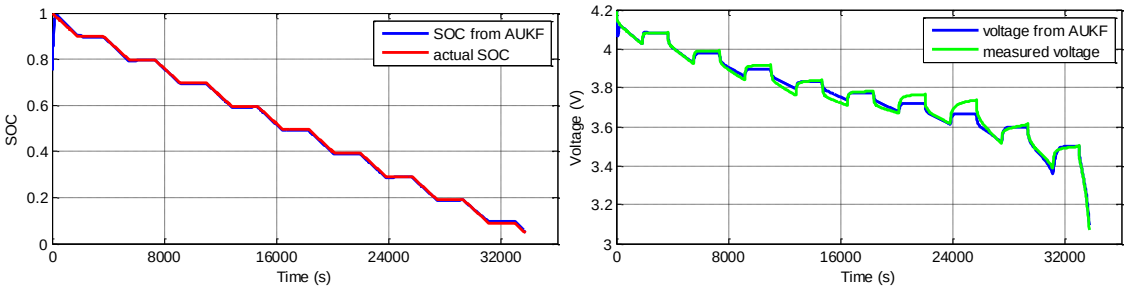

a) SOC estimation compared with actual SOC. b) Voltage estimation compared with actual voltage.

Fig. 3.15. Estimation results from AUKF for the RBF NN model.

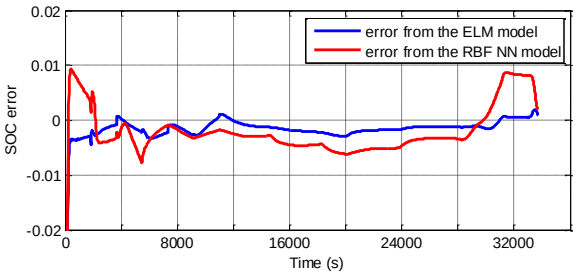

Fig. 3.16. SOC errors from AUKF for the ELM model and the RBF NN model.

3.5 Summary

In this chapter, the designs for Li-ion battery SOC estimation algorithm are presented. The KF variant algorithms are investigated and compared based on a discrete nonlinear battery model of the ELM model with experimental data. Both conventional Kalman filters including EKF and UKF, and adaptive Kalman filters including AEKF and AUKF, are applied to estimate SOC. The RBF NN model is also used in estimation process as a comparison. The estimation results show that adaptive Kalman filters have much better performance than conventional Kalman filters, both on estimation accuracy and state convergence rate. The AUKF algorithm has the highest accuracy with robustness to the initial state knowledge for SOC estimation. The estimation results also show that the ELM battery model has better performance on SOC estimation with a higher accuracy and lighter computational load compared with those of the RBF NN model. Finally, simulations and experiments show that the proposed method for SOC estimation with AUKF based on the battery model trained by the ELM algorithm achieves good performance.

Although AUKF is verified to have good performance on Li-ion battery SOC estimation in experimental conditions, this algorithm still encounters some limitations. The KF-based methods have their own flaws in practice, which will be discussed and overcome by other filtering methods in the next chapter.

Chapter 4 Li-ion Battery SOC Estimation Based On the Nonlinear Equivalent Circuit Model Using Particle Filter Methods

Considering battery model's flexibility and applications, in this chapter, another filtering strategy of the particle filter (PF) method [133] is applied to do Li-ion battery state of charge (SOC) estimation on a nonlinear equivalent circuit model. Section 4.1 introduces PF's advantage over the Kalman filter (KF) methods. In Section 4.2, a nonlinear equivalent circuit model considering SOC effect on model parameters is established. Section 4.3 describes the PF and unscented PF (UPF) algorithms. In Section 4.4, the estimation results from PF and UPF are displayed and discussed. Section 4.5 gives the conclusion of this chapter.

4.1 Introduction

The SOC estimation algorithm proposed in Chapter 3 can obtain accurate SOC estimation results for Li-ion batteries. However, the KF-based algorithms have specific demand for the system noise to be Gaussian distribution. In practice, the batteries in EVs have a harsher working environment than experimental condition. Moreover, even the adaptive part is added to extended Kalman filter (EKF) and unscented Kalman filter (UKF), their performance still depend on the model's form and accuracy since EKF has linearization error and UKF is also an approximate nonlinear estimator [36]. If the system nonlinearity is severe or the model is with complex expressions, the KF-based methods may still encounter divergence.

On the other hand, the neural network (NN) model for batteries is more suitable for simple current pattern in experimental condition. If the battery operations are in complex patterns, large data training sets and plenty of experiments are needed, making the modeling process also complex. The equivalent circuit model for Li-ion batteries considers its dynamic behavior despite the current pattern, which is more flexible. To obtain the equivalent circuit model with higher accuracy like the NN model, SOC's effect on the model circuit parameters must be clearly considered. Then, more complex structure will be brought to the model so that the KF-based methods' performance may be reduced.

In this way, the filtering algorithm of PF is proposed in this chapter to avoid the above shortcomings. As the completely nonlinear estimator, PF can perform state estimation for a complex system with strong nonlinearity in non-Gaussian system noise [57]. PF also has high estimation accuracy and does not depend much on system model's accuracy. In [17], an accurate equivalent circuit model with two RC networks considering SOC effect for Li-ion batteries is proposed. Although the model has complex expression, it is more practical and has good accuracy. In this chapter, the model with the similar form to [17] is applied. The model parameter variations to SOC are represented by nonlinear functions. Thus, it has a complex structure and nonlinearity. Then, PF is applied to perform estimation for the complex nonlinear model. Based on PF, an improved PF algorithm, the UPF algorithm, is also used to estimate SOC for Li-ion battery to achieve better estimation results.

4.2 The Equivalent Circuit Model Considering SOC Effect on Parameters

In Chapter 2, various Li-ion battery equivalent circuit models have been established. The model circuit components are set constant in Section 2.2. In Section 2.3, the SOC effect is simply described by fuzzy rules and set by a constant value in the range $SOC \in [0.2,1]$ and $SOC \in [0,0.1]$. This SOC effect is clearly interpreted in [17]. By representing SOC effect via nonlinear functions, the proposed model in [17] is quite accurate.

Instead of fuzzy rules, the SOC effects on battery model parameters are represented by nonlinear functions in this section. In this way, the proposed two-RC network equivalent circuit model in Section 2.2.2 is reconstructed. All the data for modeling is also obtained from the experiment of 0.3C current pulse test on the same battery in Section 2.2.3. The parameter extraction method is the same to the method described in Section 2.2.3. Then, all the circuit parameters including R_s, R_1, C_1, R_2, C_2 (described in Fig. 2.4) at every 0.1 SOC are computed. The R_s value versus SOC is shown in Fig. 4.1 a). When SOC is small, R_s increases exponentially. This variation trend is approximated by a single-variable nonlinear function of SOC as:

$$R_s = 0.1224e^{-17.64soc} + 0.08001 \tag{4.1}$$

Equation (4.1) is derived from Matlab curve fitting tool box. The approximation curve of R_s variation to SOC compared with the computed R_s at every 0.1 SOC is compared in Fig. 4.1 b). It indicates that the fitting curve clearly represents the SOC effect on R_s. Although some fitting errors exist at certain points, the varying trend of R_s to SOC is described accurately, especially for the low SOC range. Then, the RC network parameters are also represented by approximation curves of SOC with similar functions to R_s. The computed parameters at every 0.1 SOC compared with the SOC functions obtained by curve fitting are shown in Fig. 4.2 and 4.3. The SOC functions representing the RC parameters are derived as (4.2)-(4.5). The OCV function is the same as (2.11).

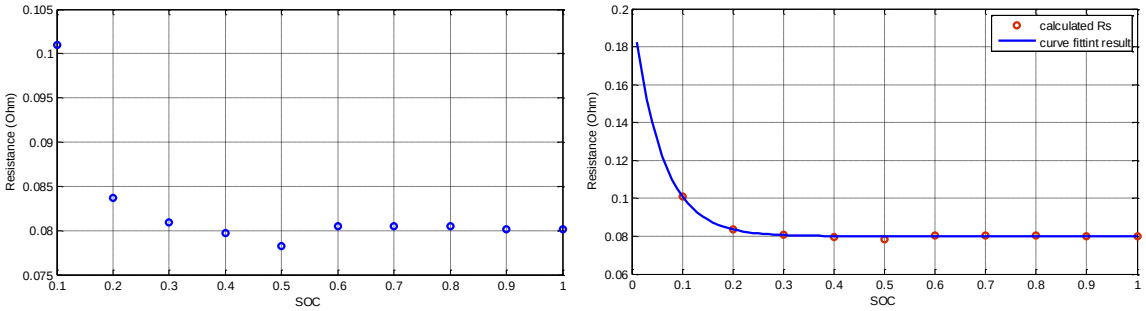

a) The calculated R_s. b) The fitting curve for R_s.

Fig. 4.1. R_s versus SOC.

$$R_1 = 2.106e^{-41.14soc} + 0.02906 \tag{4.2}$$

$$C_1 = -2000e^{-11.94soc} + 1420 \tag{4.3}$$

$$R_2 = 0.1059e^{-14.64soc} + 0.02116 \tag{4.4}$$

$$C_2 = -17300e^{-3.098soc} + 20000 \tag{4.5}$$

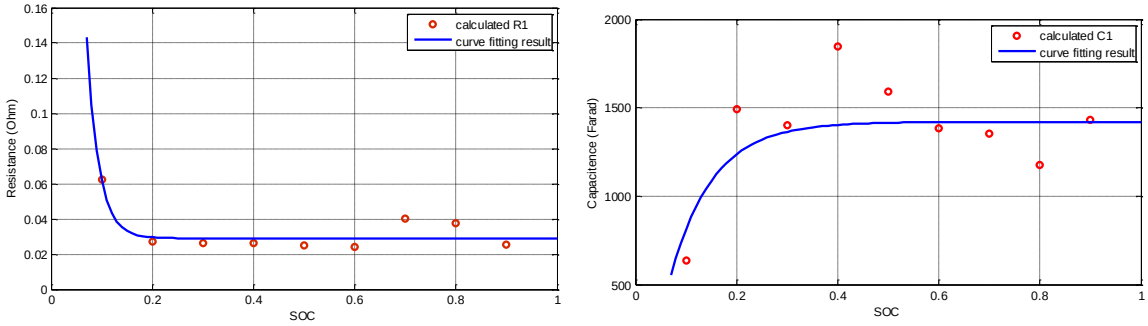

a) The fitting curve for R_1. b) The fitting curve for C_1.

Fig. 4.2. R_1 and C_1.

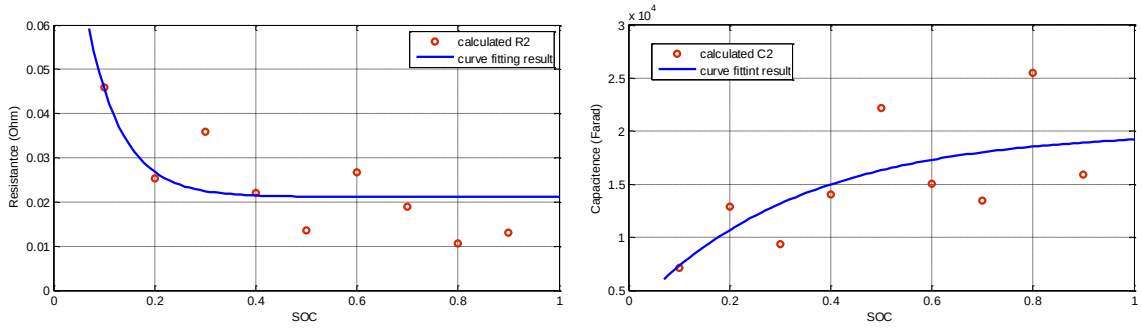

a) The fitting curve for R_2. b) The fitting curve for C_2.

Fig. 4.3. R_2 and C_2.

To test the reconstructed model, the experimental data in Section 2.2.3 is applied to both the new model and the previous model with constant parameters. The two model voltages and measured battery voltage are depicted and compared in Fig. 4.4. It is verified that the new model's accuracy is improved obviously compared with the model established in Section 2.2.3. The model RMSE is reduced from 0.0301 V to 0.0201 V.

Then, the new derived model with nonlinear functions of SOC is applied to do SOC estimation. The state-space equations for the model are derived from (1.1) and (2.7)-(2.9), described as (4.6) and (4.7):

$$\begin{bmatrix} \dot{Z} \\ \dot{V}_1 \\ \dot{V}_2 \end{bmatrix} = \begin{bmatrix} 0 & 0 & 0 \\ 0 & -\dfrac{1}{R_1 C_1} & 0 \\ 0 & 0 & -\dfrac{1}{R_2 C_2} \end{bmatrix} \begin{bmatrix} Z \\ V_1 \\ V_2 \end{bmatrix} + \begin{bmatrix} \dfrac{1}{C_n} \\ \dfrac{1}{C_1} \\ \dfrac{1}{C_2} \end{bmatrix} I \tag{4.6}$$

$$V_t = f(Z) + V_1 + V_2 + R_s I \tag{4.7}$$

where Z represents SOC and $f(Z)$ represents the $OCV(SOC)$ curve. V_1, V_2 are taken as the state variables. Considering the estimation algorithm to be used, a discrete form for system equations (4.6) and (4.7) should be obtained.

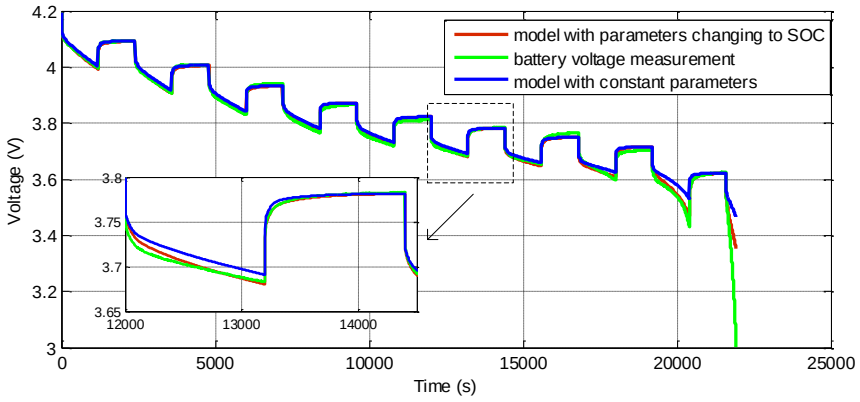

Fig. 4.4. The model output voltages compared with the measured voltage.

The discrete form for the SOC equation has been obtained as equation (1.2). Based on circuit theory, $V_1(k+1)$ can be represented by the sum of RC circuit's discrete-time zero-state response $R_1(1-e^{-\frac{\Delta t}{R_1C_1}})I(k)$ and zero-input response $e^{-\frac{\Delta t}{R_1C_1}}V_1(k)$ [134]. $V_2(k+1)$ has the similar form to $V_1(k+1)$. In experiment, the sampling internal is set around 1 s, i.e. $\Delta t = 1\,s$. Considering that all the circuit parameters are nonlinear functions of SOC, substitute these functions into the system equations with simplicity. Then, the discrete-time system with nonlinearity is described by:

$$\begin{bmatrix} Z(k+1) \\ V_1(k+1) \\ V_2(k+1) \end{bmatrix} = \begin{bmatrix} 1 & 0 & 0 \\ 0 & e^{-\frac{\Delta t}{R_1(Z(k))C_1(Z(k))}} & 0 \\ 0 & 0 & e^{-\frac{\Delta t}{R_2(Z(k))C_2(Z(k))}} \end{bmatrix} \begin{bmatrix} Z(k) \\ V_1(k) \\ V_2(k) \end{bmatrix} + \begin{bmatrix} \frac{\Delta t}{C_n} \\ R_1(1-e^{-\frac{\Delta t}{R_1(Z(k))C_1(Z(k))}}) \\ R_2(1-e^{-\frac{\Delta t}{R_2(Z(k))C_2(Z(k))}}) \end{bmatrix} I(k) \tag{4.8}$$

$$V_t(k) = f(Z(k)) + V_1(k) + V_2(k) + R_s(Z(k))I(k) \tag{4.9}$$

where all the expressions like $R_s(Z(k))$ represent the SOC functions in (4.1)-(4.5).

4.3 Particle Filter and Unscented Particle Filter

4.3.1 The PF Algorithm

The PF algorithm is a probability-based estimation approach which is suitable for highly nonlinear system. PF provides estimation results with good performance and high accuracy. Considering a nonlinear system represented by (4.10) and (4.11):

$$x_k = f(x_{k-1}, u_{k-1}, \omega_{k-1}) \tag{4.10}$$

$$y_k = h(x_k, u_k, \nu_k) \tag{4.11}$$

where ω_k and ν_k are independent white noises with known probability distribution functions (pdfs) [36]. Here it is assumed that $\omega \sim N(0,Q)$ and $\upsilon \sim N(0,R)$. The system states are Markovian, i.e.,

$$P(x_k \mid x_{k-1}, x_{k-2}, ..., x_0) = P(x_k \mid x_{k-1}) \tag{4.12}$$

PF is a Monte Carlo method based on sequential importance sampling for implementing a recursive Bayesian filter. The posterior state is approximated by a set of weighted state vectors named particles. The key part for PF is to obtain $P(x_t \mid y_{0:t})$ by generating a set of samples with associated weights. At each time step, the particles are propagated and corresponding weight for each particle is computed. The PF algorithm is described as follows [57]:

1) Initialization:

Determine the number of particles *M* according to the system's form and computational cost. Generate the state particles $x_0^i (i = 1, 2..., M)$ based on the initial pdf $p(x_0)$, where *i* represents the *ith* particle. Here,

$$x_0^i = x_0 + N(0,Q) \tag{4.13}$$

2) State propagation:

For *i* = 1, 2…, *M* particles, propagate the state particles $x_{k-1}^i (i = 1, 2..., M)$ to the next step *k* by the system process equation (4.14):

$$x_k^i = f(x_{k-1}^i, u_{k-1}) + N(0, Q) \tag{4.14}$$

where x_{k-1}^i represents the prior state.

3) Determination of particle weights:

Update and normalize the important weights for each particle based on the measurement. Calculate the *ith* particle's likelihood as:

$$q_i = \exp(-\frac{1}{2\sqrt{R}}(y_k - h(x_k^i, u_k))^2) / \sqrt{2\pi R} \tag{4.15}$$

where y_k represents the measurement at step *k*. $h(x_k^i, u_k)$ is the *ith* particle's output calculated with the system measurement equation. Then normalize the likelihood q_i of each particle by:

$$\bar{q}_k^i = \frac{q_i}{\sum_{j=1}^{M} q_j} \tag{4.16}$$

where $\bar{q}_k^i$ is the normalized weight for the *ith* particle. After the normalization step, all the likelihoods' sum is 1. $\bar{q}_k^i$ represents the probability of observing the measurement from the corresponding particle's state.

4) Re-sampling:

A new particle set $\{\bar{x}_k^i\}_{i=1}^M$ is obtained by re-sampling. The basic idea of re-sampling is to eliminate particles with small weights and to concentrate on particles with large weights. For $i = 1, 2\ldots, M$, execute the re-sampling process with the following two steps. A random number λ uniformly distributed on [0, 1] is chosen. Then, accumulate the particle weight into a sum successively until the sum is greater than λ [36]. When $\sum_{n=1}^{j-1} \bar{q}_k^n < \lambda$ and $\sum_{n=1}^{j} \bar{q}_k^n > \lambda$, set the particle $\bar{x}_k^i$ to x_k^j with the weight $\bar{q}_k^i$.

5) Estimation:

Calculate the mean of the re-sampled particles to obtain PF's estimation result $\hat{x}_k$:

$$\hat{x}_k = \frac{1}{M}\sum_{i=1}^{M} \bar{x}_k^i \quad . \tag{4.17}$$

For k = 1, 2…, the steps 2)-5) are executed recursively.

4.3.2 The UPF Algorithm

The algorithm of PF obtains the proposal distribution for the state vector by sampling from the state evolution's probabilistic model. However, such proposal distribution generation strategy may be inefficient if new measurement is not used to propagate the states' new values. Based on the PF algorithm, the UPF algorithm [56] is proposed to improve state estimation performance. UPF utilizes the UKF algorithm for proposal distribution generation with a PF framework. The utilization of UKF can provide more accurate proposal distribution generation. It moves the particles to high likelihood region. UPF has better performance than PF, especially for the system with high nonlinearity. At every step, the particles are propagated using UKF and the latest observation is incorporated. The UPF algorithm is described as follows.

First, generate particles as ordinary PF algorithm described in the previous section at time step k = 0. After initialization, update the state and covariance with the UKF algorithm for each particle. The UKF algorithm has been described in Section 3.2.2 and it is combined with the PF algorithm structure described in Section 4.3.1. With UKF, the measurement is incorporated into the new pdf at each sampling step. Then the M particles are evaluated by the weights and the re-sampling step is taken. The algorithm is executed iteratively like PF. The UPF operation schematic is depicted in Fig. 4.5. It reveals that the UPF algorithm has similar execution steps to PF, except that the state propagate step is implemented by UKF.

4.4 Estimation Results and Discussion

In this section, SOC estimation is done on the discrete-time nonlinear battery model proposed in Section 4.2. Both the PF and UPF algorithms are used and the estimation results are compared and discussed in this section. The current and voltage measured from the battery experiment in Section 2.2.3 are used. Considering the trade-off between estimation accuracy and calculation speed, the number of particles is set to $M = 100$ in both algorithms.

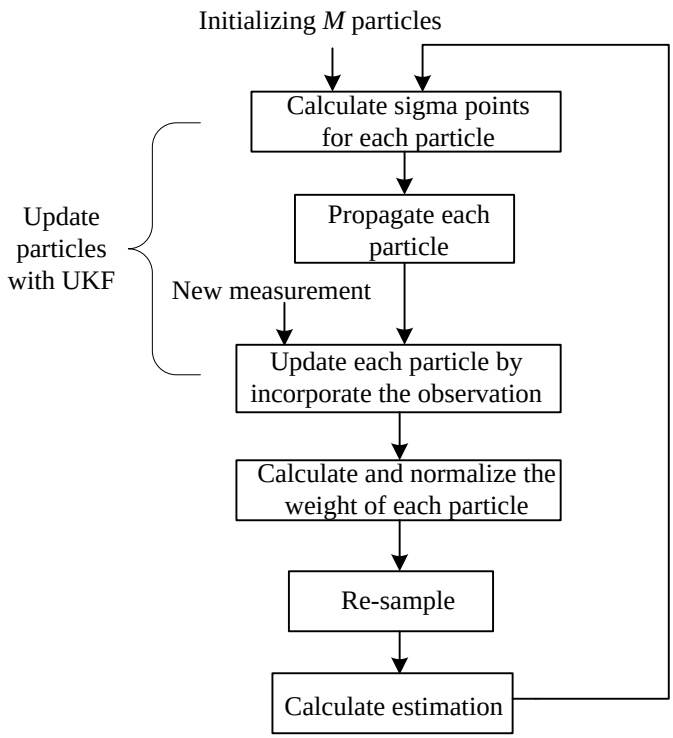

Fig. 4.5. The operation schematic for UPF.

The estimation results from the PF algorithm are shown in Fig. 4.6. The initial SOC is set to the correct initial value of 1. The estimated SOC compared with actual SOC and the estimation error is depicted. It reveals that the maximum SOC error is around 6%, larger than common tolerant SOC error of 5%. The estimation computational time is 14.1805 s. The estimation results for the other two state variables, V_1 and V_2, are shown in Fig. 4.7. Then, the initial SOC is set an incorrect value of 0.8 to test PF's robustness. The estimation results are shown in Fig. 4.8. It shows that the maximum SOC error after convergence is still larger than 5%. To test the convergence speed of PF, a clear display of the convergence time is shown in Fig. 4.9. It takes around 530 s for the estimation error to achieve less than 5%, which is a bit long for EV applications.

Then, the UPF algorithm is also tested for both estimation accuracy and robustness. Firstly, the initial SOC is set 1 and the estimation results are shown in Fig. 4.10. It verifies that the estimation performance from UPF is better than PF. The maximum estimation error of UPF achieved is smaller than 5%. A comparison between PF and UPF for SOC estimation error is shown in Fig. 4.11, indicating the error form UPF perform smaller with less variation than PF in most regions. To compare the SOC error more clearly, the estimation

RMSEs are computed. The RMSE for UPF is 0.0151, smaller than 0.0181 for PF. It verifies that the UPF algorithm obtains better accuracy than PF. The estimation results for the other two states, V_1 and V_2, are shown in Fig. 4.12. Compared with PF, the estimation results from UPF are more stable. Nevertheless, the computational time of estimation for UPF is 227.5587 s, which is also much longer than PF. It indicates that the UPF algorithm brings heavy computation to the system.

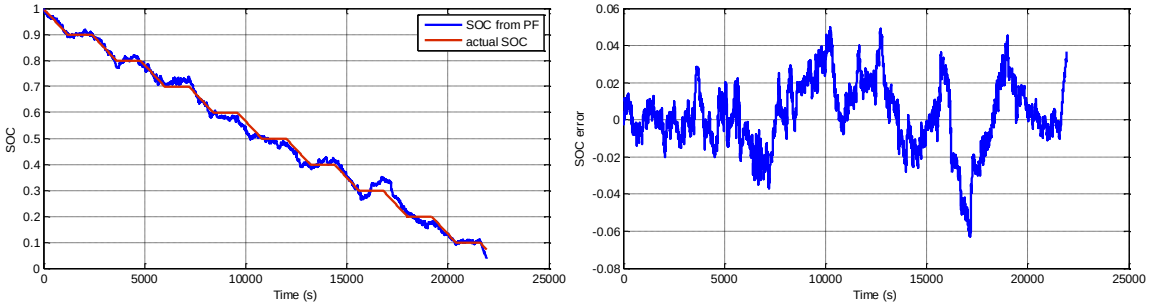

a) SOC estimation. b) SOC error.

Fig. 4.6. SOC estimation results from PF compared with actual SOC.

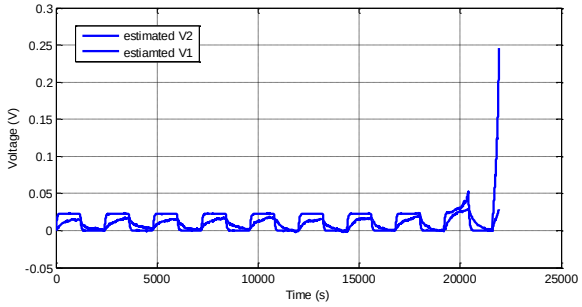

Fig. 4.7. Estimation results for the RC voltages.

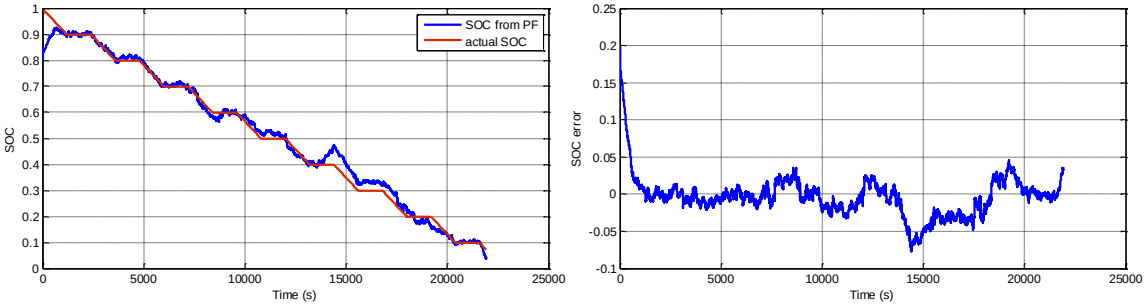

a) SOC estimation. b) SOC error.

Fig. 4.8. SOC estimation results from PF compared with actual SOC (incorrect initial SOC).

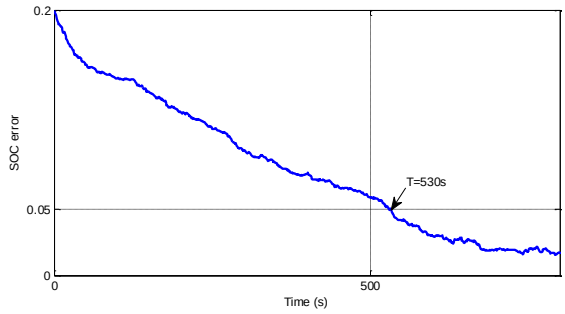

Fig. 4.9. PF convergence time.

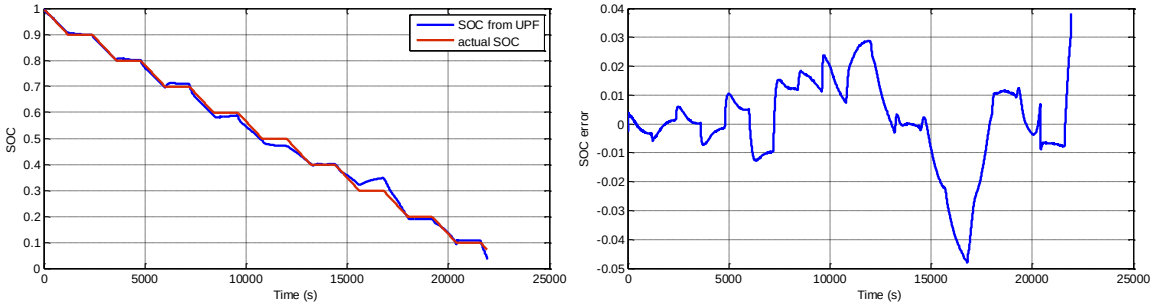

a) SOC estimation compared with actual SOC. b) SOC error.

Fig. 4.10. SOC estimation results from UPF.

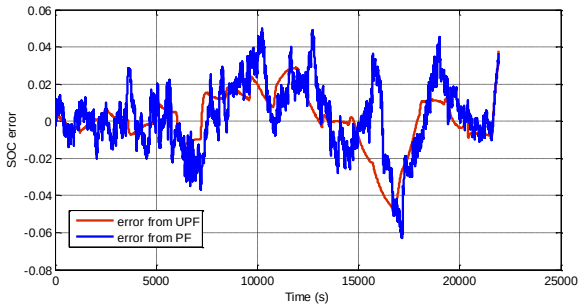

Fig. 4.11. The comparison of SOC error between PF and UPF.

The estimation results from UPF with the initial SOC set at 0.8 are shown in Fig. 4.13. The maximum SOC error after convergence is also smaller than 5%, which is better than PF. The RMSE for the SOC error from UPF is 0.0157, much smaller than 0.0280 of PF in the same testing condition. Fig. 4.13 b) shows that the estimated SOC converges with a much faster speed than that of PF. A clear display for the convergence speed of UPF is shown in Fig. 4.14. It takes only around 23 s for the estimated SOC with incorrect initial value to achieve error smaller than 5%. It is verified that the UPF algorithm has

robustness to the initial state and the convergence speed is much faster than the PF algorithm.

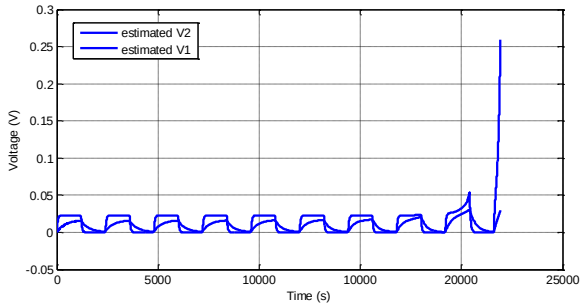

Fig. 4.12. Estimation results from UPF for the RC voltages.

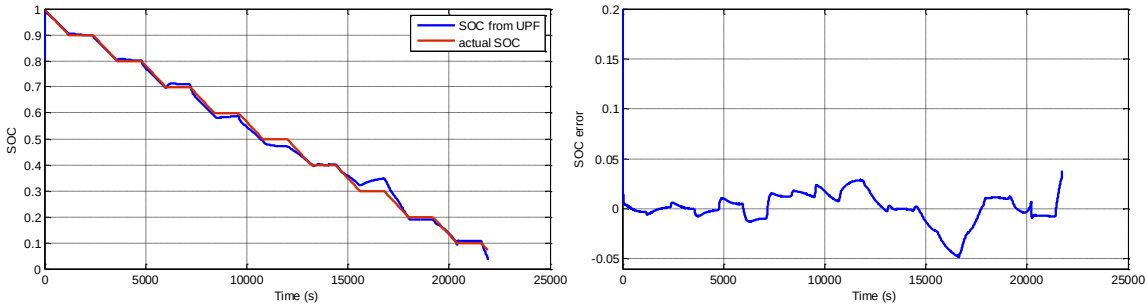

a) SOC estimation compared with actual SOC. b) SOC error.

Fig. 4.13. SOC estimation results from UPF (incorrect initial SOC).

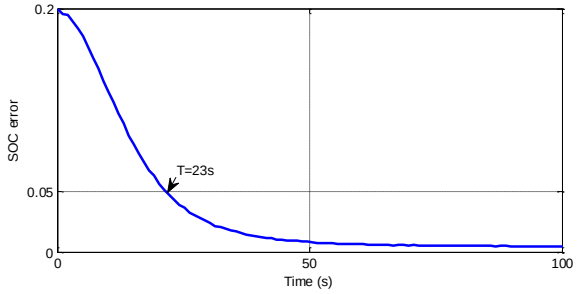

Fig. 4.14. UPF convergence time.

It is shown that UPF has better performance for SOC estimation on the same battery model, especially for the case that the initial SOC is incorrect. Both the estimation accuracy and convergence rate are obviously improved for UPF compared with PF. However, the estimation computational time for UPF also increases, implying heavier computation. Actually, compared with the KF-based algorithms, the PF and UPF

algorithms have heavy computation. With more number of particles, the estimation accuracy will be improved, whereas the estimation time will also be prolonged. Thus, a trade-off between estimation accuracy and system computational load is needed when choosing the PF methods.

4.5 Summary

In this chapter, the equivalent circuit model with two RC networks for Li-ion battery is reconstructed and SOC estimation is executed on this model. The SOC effect on model circuit parameters is represented by nonlinear functions. Thus, the model accuracy is improved. Then, the nonlinear estimators including PF and UPF are applied to estimate SOC for the model. The utilization of UPF improves the estimation method's performance. The estimation results show that the PF methods can do SOC estimation for the nonlinear battery model. Compared with PF, the improved algorithm of UPF has better performance, although with heavier computation. This heavy computational load may be problematic in practice, leading to strict limitation for EMS in EVs. This problem will be solved in the next chapter. In the next chapter, a novel estimation technique which is simpler and more applicable will be used instead of the PF methods. Correspondingly, the battery model will also be modified. The proposed estimation algorithm in the next chapter will provide accurate estimation results despite the noise distribution with reduced computation load.

Chapter 5 An Adaptive Sliding Mode Observer for Li-ion Battery SOC and SOH Estimation

Based on previous chapters, research on state of charge (SOC) estimation is continued and improved in this chapter. Besides, estimation for Li-ion battery state of health (SOH) is also discussed in this chapter. Section 5.1 gives an introduction to the model and estimation algorithm used in this chapter. In Section 5.2, the battery model established in Section 4.2 is simplified by adding the expressions of uncertainty. In Section 5.3, an adaptive gain sliding mode observer is designed in detail. Compared with the conventional sliding mode observer, the adaptive sliding mode observer gives better SOC estimation for Li-ion battery based on the model with uncertainty. In Section 5.4, an adaptive observer scheme using the sliding mode technique is proposed and applied to do battery SOC and SOH estimation simultaneously. Section 5.5 gives the summary of this chapter.

5.1 Introduction

As Chapter 4 indicates, the algorithm of unscented particle filter (UPF) provides accurate SOC estimation with robustness for the equivalent circuit model of Li-ion batteries. However, the computation of PF methods is quite complex, which will bring heavy burden to energy management system (EMS) in electric vehicles (EVs). Besides, the equivalent circuit model with SOC functions has complex expressions and the model error is still inevitable. Even tested precisely, the battery model is difficult to obtain with very high accuracy because of complex inner electrochemical reactions of Li-ion batteries. In this chapter, the equivalent circuit model with two resistor-capacitor (RC) networks for Li-ion batteries is established with all the parameter variations and model errors represented by uncertainties. This model provides a simple structure and a convenient implementing process, whereas the accuracy could also be acceptable if appropriate estimation algorithms are selected.

Using the proposed model with uncertainties, the sliding mode observer is applied to do state estimation in this chapter. The sliding mode observer is proposed and developed in [63]. This kind of observer deals with system uncertainty and noise efficiently and its

algorithm is simple without complex matrix operation like Kalman filter (KF)-based methods [91], which is suitable for practical applications. When the sliding surface is reached, the equivalent control method can be applied to obtain some unknown system quantities [63, 66]. In [67], an adaptive gain observer combined with the sliding mode approach is proposed. This adaptive observer is simple to implement and robust to the *a priori* knowledge of the system noise. Based on the proposed battery model, a sliding mode observer with adaptive gain could be applied to estimate battery SOC. Comparing with the sliding mode observer in [18], the adaptive observer could improve the estimation performance.

SOH estimation is also investigated and executed in this chapter. As another important state for Li-ion batteries, SOH also needs estimation results with accuracy and robustness. Based on the proposed SOC observer, an adaptive observer scheme based on the sliding mode technique is proposed and designed in this chapter. Then, SOC and SOH are estimated simultaneously by this proposed adaptive observer. The battery estimation results show good accuracy and robustness for both SOC and SOH of the proposed method.

5.2 Li-ion Battery Equivalent Circuit Model with Uncertainties

As the model with appropriate trade-off between accuracy and simplicity, the equivalent circuit model with two RC networks for Li-ion batteries described in previous chapters is also investigated and applied in this section. The model circuit has been depicted in Fig. 2.4. Compared with the model in Section 4.2, some changes are made to the system equations of (4.6)-(4.7). A function $g(SOC)$ approximating the relationship *OCV*(*SOC*) is used in the model.

The model equations describing the model circuit include (1.1) and (2.7)-(2.9), where (2.9) is reconstructed as:

$$V_t = g(Z) + V_1 + V_2 + R_s I \tag{5.1}$$

where $g(Z)$ consists of a series of piecewise linear functions as in [18]:

$$g(Z) = k_i \cdot Z + d_i, i = 1, 2... \tag{5.2}$$

Neglect the current time derivative in one sampling interval. Considering (2.7) and (2.8), the time derivative of (5.1) is obtained as:

$$\dot{V}_t = -V_d + b_1 I \tag{5.3}$$

where $V_d = \frac{V_1}{R_1 C_1} + \frac{V_2}{R_2 C_2}$, $b_1 = k_i \frac{1}{C_n} + \frac{1}{C_1} + \frac{1}{C_2}$.

The current I is represented by the following expression derived from (5.1):

$$I = \frac{1}{R_s}(V_t - g(Z) - V_1 - V_2) \tag{5.4}$$

Substituting (5.4) and V_d into the model equations, the system equations are obtained as (5.5)-(5.7):

$$\dot{V}_d = -a_{22} V_d + a_{23} V_2 + b_2 I \tag{5.5}$$

$$\dot{V}_2 = a_{31} V_t - a_{32} V_d + a_{33} V_2 - a_{34} g(Z) \tag{5.6}$$

$$\dot{Z} = a_{41} V_t - a_{42} V_d - a_{43} V_2 - a_{44} g(Z) \tag{5.7}$$

where

$$a_{22} = \frac{1}{R_1 C_1} \quad , \quad a_{23} = \frac{1}{R_1 C_1 R_2 C_2} - \frac{1}{R_2^2 C_2^2} \quad , \quad b_2 = \frac{1}{R_1 C_1^2} + \frac{1}{R_2 C_2^2} \quad , \quad a_{31} = \frac{1}{R_s C_2} \quad , \quad a_{32} = \frac{R_1 C_1}{R_s C_2} \quad ,$$

$$a_{33} = -\frac{1}{R_2 C_2} - \frac{1}{R_s C_2} + \frac{R_1 C_1}{R_s R_2 C_2^2}, \; a_{34} = a_{31}, \; a_{41} = \frac{1}{R_s C_n}, \; a_{42} = \frac{R_1 C_1}{R_s C_n}, \; a_{43} = \frac{1}{R_s C_n}(1 - \frac{R_1 C_1}{R_2 C_2}),$$

$a_{44} = a_{41}$.

All the circuit parameters have been extracted in Chapters 2 and 4. Here, the piecewise linear function $g(Z)$ is obtained by curve fitting in some specific SOC regions. The measured OCV, the nonlinear fitting function (2.11) accurately representing OCV and the piecewise linear functions $g(Z)$ are depicted and compared in Fig. 5.1. It reveals that $g(Z)$ describes the OCV curve with linearization errors.

The calculated value of R_s versus SOC has been shown in Fig. 4.1 a). To simplify this variation trend in battery model, the average R_s in $SOC \in [0.2,1]$ is approximated as the

R_s value, which is set constant in the entire SOC range. The RC circuit parameters also vary in the entire SOC range as shown in Fig. 4.2 and Fig. 4.3. To simplify the model, R_1, C_1, R_2, and C_2 are also designed as constant when SOC varies, instead of the nonlinear functions of SOC proposed in Chapter 4. The Matlab function "*fminsearch*" in the optimization tool box is utilized after curve fitting to obtain the optimal RC values for the entire SOC range. Then, the optimized values are taken as the model RC circuit parameters. The calculated circuit parameters from Section 4.2 and the newly designed constant parameters in this section are shown in Figs. 5.2-5.4. The new model parameter values are displayed in Table 5.1. The coefficients in the system equations including (5.3) and (5.5)-(5.7) are calculated by these parameters.

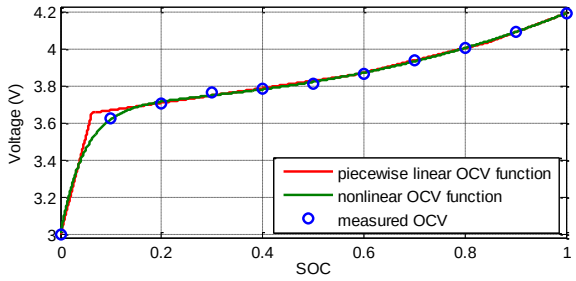

Fig. 5.1. The measured OCV and piecewise linear OCV functions.

Table 5.1 Model parameters for the newly designed equivalent circuit model.

R_s	R_1	C_1	R_2	C_2
0.08 Ω	0.0299 Ω	1455 F	0.02 Ω	16026 F

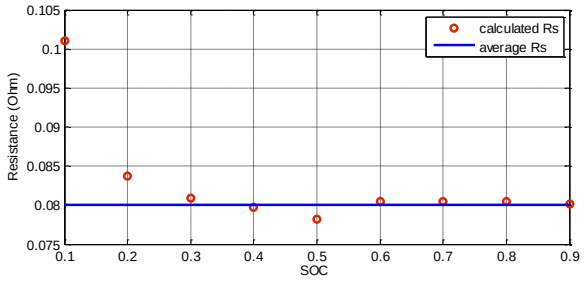

Fig. 5.2. The R_s value versus SOC.

After determining all the model parameters, the established model's output voltage is compared with the experimental voltage in Fig. 5.5. It shows that the model error is quite small in the range $SOC \in [0.2,1]$. The largest error exists around the cut-off voltage

region. The model RMSE is 0.0288 V, larger than the model with nonlinear functions representing SOC effect but smaller than the model with parameters calculated at $SOC = 0.5$. The model has obvious simplification steps during the modeling process. To test the model's flexibility, another larger discharging current (0.8C) in Fig. 5.6 is applied to the battery in experiment and the model. The model voltage compared with the measured battery voltage is shown in Fig. 5.7. The model's error has similar characteristics as found in Fig. 5.5.

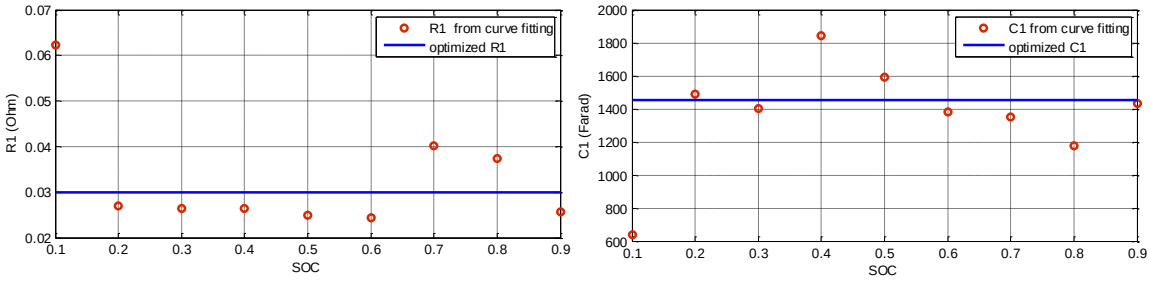

a) R_1. b) C_1.

Fig. 5.3. Optimized R_1 and C_1 values versus SOC.

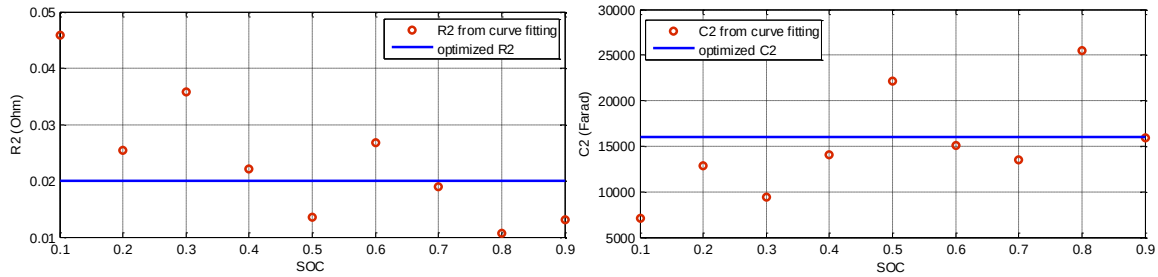

a) R_2. b) C_2.

Fig. 5.4. Optimized R_2 and C_2 values versus SOC.

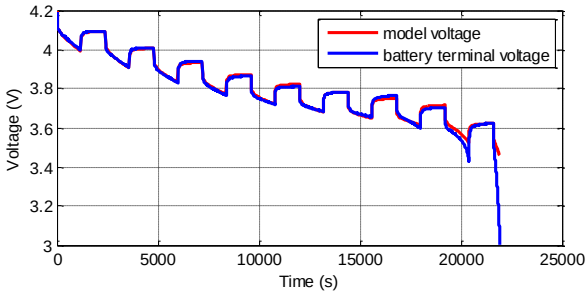

Fig. 5.5. The model output compared with measured battery voltage.

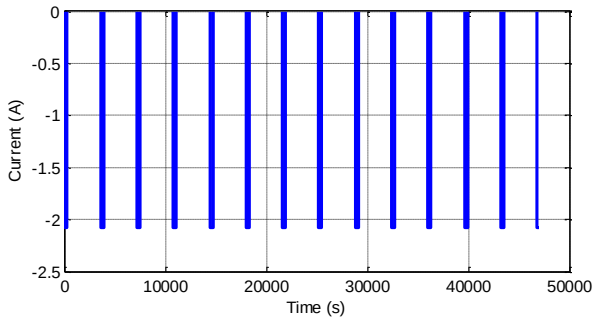

Fig. 5.6. The 0.8C current.

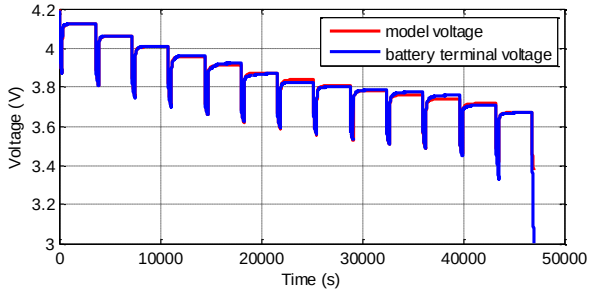

Fig. 5.7. The model output compared with measured battery voltage (0.8C).

The battery equivalent circuit model described above is established using the approaches of linearization and parameter simplification. These steps bring inaccuracy to the model. For example, the model's large error around the cut-off voltage region is caused by the obvious parameter approximation error in small SOC range. Besides, the battery parameter uncertainty is hard to avoid thoroughly in practice. In summary, the system equations of (5.3) and (5.5)-(5.7) are not accurate and the modeling error should be taken into consideration. Hence, the system equations are changed to (5.8)-(5.11) by adding uncertainties to the original model:

$$\dot{V}_t = -V_d + b_1 I + \Delta f_1 \tag{5.8}$$

$$\dot{V}_d = -a_{22} V_d + a_{23} V_2 + b_2 I + \Delta f_2 \tag{5.9}$$

$$\dot{V}_2 = a_{31} V_t - a_{32} V_d - a_{33} V_2 - a_{34} g(Z) + \Delta f_3 \tag{5.10}$$

$$\dot{Z} = a_{41} V_t - a_{42} V_d - a_{43} V_2 - a_{44} g(Z) + \Delta f_4 \tag{5.11}$$

The uncertainties $\Delta f_1 \sim \Delta f_4$ describe the model inaccuracy caused by varying parameters,

linearization, and measurement noise. It is noticed that the Li-ion battery current and voltage are both bounded according to the battery operation conditions: $|I| \le 5A$, $3\,V \le V_t \le 4.23\,V$, which is controlled by the existing test system. Hence, the uncertainties are also bounded and the upper bounds can be calculated by the model error from experiments or experts' experiences.

5.3 Sliding Mode Observer with Adaptive Gain

5.3.1 Sliding Mode Observer

To estimate the proposed Li-ion battery's equivalent circuit model with uncertainties, the sliding mode observer is studied and designed in this section. Based on the sliding mode control technique, the sliding mode observer is designed using sliding manifold concepts to make the estimation error dynamics converged to zero in finite time by a discontinuous control law. The sliding mode observer has simple implementation with reliable and robust tracking property in the presence of modeling error and uncertainties [18, 59]. This kind of observers has no specific demand for the system noise, e.g. Gaussian noise or zero-mean noise. Compared with the KF-based methods, the sliding mode observer has no matrix operations and achieves lighter computation.

In [63], the sliding mode observer based on an equivalent control method is proposed and implemented. This kind of observers has a simple design process and a fast convergence rate. The state equations (5.8)-(5.11) have the special structure that the sliding mode observer can be designed directly. Hence, the sliding mode observer with the form in [18] is designed here. For the system measurement V_t in (5.8), the observer is designed as:

$$\dot{\hat{V}}_t = -\hat{V}_d + b_1 I + \lambda_1 \operatorname{sgn}(V_t - \hat{V}_t) \tag{5.12}$$

where λ_1 represents the observer gain defined by a positive constant. sgn(.) is the sign function: $\operatorname{sgn}(e) = \begin{cases} 1 & e > 0 \\ 0 & e = 0 \\ -1 & e < 0 \end{cases}$. Then,

$$\dot{e}_1 = -(V_d - \hat{V}_d) + \Delta f_1 - \lambda_1 \operatorname{sgn}(e_1) \tag{5.13}$$

where $e_1 = V_t - \hat{V}_t$.

The convergence proof is described below. Define the Lyapunov candidate function as $V_1 = 0.5e_1^2$. The time derivative of the Lyapunov candidate is $\dot{V}_1 = e_1\dot{e}_1$. Set the observer gain as a constant in the range $\lambda_1 > \max(|\Delta f_1| + |V_d - \hat{V}_d|)$, then $\dot{V}_1 < 0$. In [66], it is stated that sliding mode occurs in finite time when system (5.12) is forced to the sliding manifold. $e_1 = 0$ and $\dot{e}_1$ is considered 0 thereafter. When the system behaves on the sliding mode surface, using the equivalent control method and assuming $e_1 = \dot{e}_1 = 0$ [63], e_2 is calculated by $e_2 \approx [-\lambda_1 \operatorname{sgn}(e_1)]_{eq}$. Here, Δf_1 is neglected because it is very small compared with the selected λ_1. The equivalent control part describes e_2's contribution to forcing V_t to stay along the sliding mode surface.

For the other three states, the sliding mode observers with the same form to (5.12) are designed as (5.14)-(5.16):

$$\dot{\hat{V}}_d = -a_{22}\hat{V}_d + a_{23}\hat{V}_2 + b_2 I + \lambda_2 \operatorname{sgn}(V_d - \hat{V}_d) \tag{5.14}$$

$$\dot{\hat{V}}_2 = a_{31}\hat{V}_t - a_{32}\hat{V}_d + a_{33}\hat{V}_2 - a_{34}g(\hat{Z}) + \lambda_3 \operatorname{sgn}(V_2 - \hat{V}_2) \tag{5.15}$$

$$\dot{Z} = a_{41}\hat{V}_t - a_{42}\hat{V}_d - a_{43}\hat{V}_2 - a_{44}g(\hat{Z}) + \lambda_4 \operatorname{sgn}(Z - \hat{Z}) \tag{5.16}$$

where $\lambda_2 \sim \lambda_4$ are observer gains defined by positive constants. Define the state estimation errors e_2, e_3, and e_4 as $e_2 = V_d - \hat{V}_d$, $e_3 = V_2 - \hat{V}_2$, and $e_4 = Z - \hat{Z}$. The error dynamics are obtained as:

$$\dot{e}_2 = -a_{22}e_2 + a_{33}(V_2 - \hat{V}_2) + \Delta f_2 - \lambda_2 \operatorname{sgn}(e_2) \tag{5.17}$$

$$\dot{e}_3 = a_{31}e_1 - a_{32}e_2 + a_{33}e_3 - a_{34}(g(Z) - g(\hat{Z})) + \Delta f_3 - \lambda_3 \operatorname{sgn}(e_3) \tag{5.18}$$

$$\dot{e}_4 = a_{41}e_1 - a_{42}e_2 - a_{43}e_3 - a_{44}(g(Z) - g(\hat{Z})) + \Delta f_4 - \lambda_4 \operatorname{sgn}(e_4) \tag{5.19}$$

Define the Lyapunov candidate function for (5.17) as $V_2 = 0.5e_2^2$. The time derivative of the Lyapunov candidate is $\dot{V}_2 = e_2\dot{e}_2$. Determine the observer gain that meets the demand

$\lambda_2 > \max(|\Delta f_2| + |a_{22}e_2| + |a_{23}e_3|)$. Then, $\dot{V}_2 = e_2\dot{e}_2 < 0$. The sliding mode manifold will be reached in finite time. e_2 converges to 0 and $\dot{e}_2$ is considered 0 thereafter. Using the equivalent control method and assuming $e_2 = \dot{e}_2 = 0$, the description for e_3 is obtained by $e_3 \approx [(1/a_{23})\lambda_2 \operatorname{sgn}(e_2)]_{eq}$.

Define the Lyapunov candidate function $V_3 = 0.5e_3^2$ for e_3. Define $\lambda_3 > \max(|\Delta f_3| + |a_{33}e_3| + |a_{34}(g(Z) - g(\hat{Z}))|)$. Thus, $\dot{V}_3 = e_3\dot{e}_3 < 0$. e_3 converges to 0 in finite time and $\dot{e}_3$ is considered 0 thereafter. It is assumed that $g(Z) - g(\hat{Z}) = k_i e_4$. The inaccuracy caused by this approximation is incorporated into Δf_3. Using the equivalent control method, e_4 is described by $e_4 \approx [1/(k_i a_{34})\lambda_3 \operatorname{sgn}(e_3)]_{eq}$.

Define the Lyapunov candidate function for e_4 as $V_4 = 0.5e_4^2$. Define $\lambda_4 > \max(|(k_i / a_{34})e_4| + |\Delta f_4|)$. Then, $\dot{V}_4 = e_4\dot{e}_4 < 0$. The sliding mode manifold will be reached in finite time and e_4 converges to zero.

In the established Li-ion battery model, all the states are obviously bounded. Thus, $e_1 \sim e_4$ are bounded and the bounds can also be determined. The sliding mode observer gains can be determined directly according to the bounds of $\Delta f_1 \sim \Delta f_4$ and $e_1 \sim e_4$.

5.3.2 Sliding Mode Observer with Adaptive Gain

Although easy to design, the sliding mode observer described in Section 5.3.1 may encounter the problems of large chattering effect or poor tracking performance with unsuitably designed gains. Taking (5.12) as an example, the appropriate margin above $\max(|\Delta f_1| + |e_2|)$ of the determined λ_1 is not easy to decide. In [67] and [135], a sliding-mode technique based observer with adaptive gain is proposed. The observer gains are self-tuned to achieve better performance. The adaptive gain improves the observer's robustness and estimation accuracy. In this section, the design for an adaptive sliding mode observer with the form in [135] is proposed to perform the Li-ion battery SOC estimation to avoid improper chattering effect and improve estimation performance. The observer of (5.12) is changed to a new form:

$$\dot{\hat{V}}_t = -\hat{V}_d + b_1 I + \hat{\lambda}_1(t)\frac{e_1}{|e_1| + \delta} \tag{5.20}$$

where $\dot{\hat{\lambda}}_1(t) = \begin{cases} 2\alpha|e_1|, \ if \ |e_1| > 2\delta \\ 0, \quad else \end{cases}$ [67].

In the adaptive sliding mode observer (5.20), the discontinuous function sgn(e_1) in (5.12) is substituted by a continuous function $e_1/(|e_1| + \delta)$ to reduce the chattering effect [135, 136]. δ is defined a small positive scalar. α determines the adjusting speed of the adaptive gain $\hat{\lambda}_1$. $\hat{\lambda}_1(0)$ is set a positive constant and it is obvious that $\hat{\lambda}_1(t) \geq \hat{\lambda}_1(0)$. Thus, the dynamics for e_1 is:

$$\dot{e}_1 = -e_2 + \Delta f_1 - \hat{\lambda}_1(t)\frac{e_1}{|e_1| + \delta} \tag{5.21}$$

Define the Lyapunov candidate function [135] as $V_1^1 = e_1^2 + \alpha_1^{-1}(0.5\hat{\lambda}_1 - \lambda_1)^2$, where λ_1 is the constant observer gain designed in (5.12). Differentiate the Lyapunov function, considering $\dot{\lambda}_1 = 0$ and $\lambda_1 > \max(|\Delta f_1| + |e_2|)$:

$$\begin{aligned} \dot{V}_1^1 &= 2e_1\dot{e}_1 + (1/2\alpha_1)\hat{\lambda}_1\dot{\hat{\lambda}}_1 - (1/\alpha_1)\lambda_1\dot{\hat{\lambda}}_1 \\ &= 2e_1(-e_2 + \Delta f_1 - \hat{\lambda}_1\frac{e_1}{|e_1| + \delta}) + \hat{\lambda}_1|e_1| - 2\lambda_1|e_1| \\ &= 2(e_1(-e_2 + \Delta f_1) - \lambda_1|e_1|) + \frac{2\hat{\lambda}_1\delta|e_1| - \hat{\lambda}_1\delta|e_1| - \hat{\lambda}_1|e_1|^2}{|e_1| + \delta} \\ &= 2(e_1(-e_2 + \Delta f_1) - \lambda_1|e_1|) + 2\hat{\lambda}_1\frac{|e_1|\delta}{|e_1| + \delta} - \hat{\lambda}_1|e_1| \\ &< 2\hat{\lambda}_1\frac{|e_1|\delta}{|e_1| + \delta} - \hat{\lambda}_1|e_1| \end{aligned} \tag{5.22}$$

Considering the condition $|e_1(t)| > 2\delta$, (5.22) becomes:

$$\dot{V}_1^1 < -\frac{2}{3}\delta\hat{\lambda}_1(0) \tag{5.23}$$

In [135], it is interpreted that $|e_1(t)| > 2\delta$ cannot be satisfied forever because of V_1^1's

form. The bound $|e_1(t)| \le 2\delta$ will be reached in finite time and then maintained. When the bound for e_1 is reached, $\hat{\lambda}_1$ stops increasing and stays constant. In addition, it is proved in [135] that $|\dot{e}_1|$ stays in a range which is a multiple of δ. The bound of $|\dot{e}_1|$ will be very small if δ is set a very small scalar. Hence, $|\dot{e}_1|$ and Δf_1 are negligible in (5.21) in finite time. Then, $e_2 \approx -\hat{\lambda}_1 \frac{e_1}{|e_1| + \delta}$.

To test the proposed observer's effect, the observers for the other three states are set the same as (5.14)-(5.16) in Section 5.3.1. The convergence proof is also the same as stated in Section 5.3.1.

5.3.3 SOC Estimation Results and Discussion

To verify the proposed observer's performance, both the sliding mode observer (5.12), (5.14)-(5.16) with the form in [18] and the adaptive gain sliding mode observer described in Section 5.3.2 are designed in this section. The estimation results are shown and compared. The observer parameters are designed as follows: $\hat{\lambda}_1(0) = 0.05$, $\lambda_1 = 0.05$, $\lambda_2 = 0.001$, $\lambda_3 = 0.03$, $\lambda_4 = 0.02$, $\delta = 0.000001$, $\alpha = 0.0005$.

The battery data from experiments are used to conduct the SOC estimation and comparison. The actual battery SOC is calculated by the Coulomb counting method using the current and sampling time recorded by the test system. The actual initial SOC is 1 and the initial SOC for estimation is set to 0.2, which aims to show the robustness of the proposed observer.

Firstly, the SOC for the battery experiment described in Section 2.2.3 is estimated by the two observers. The estimation results are shown in Fig. 5.8 to Fig. 5.11. The comparison between actual SOC and the estimated SOC from the two observers are shown in Fig. 5.8. The estimation error comparison clearly verifies that the adaptive observer provides much better estimation performance. For the sliding mode observer in [18], the estimation encounters an obvious spine caused by chattering effect and model uncertainties when battery current changes. For the adaptive observer, the spine is relieved apparently into an acceptable extent. In the SOC range [0.2, 1], the estimation error after convergence stays

smaller than 2%. In the small SOC range, although the model has an obvious error that having been taken as the uncertainty, the estimated SOC error from the adaptive observer is still kept around 5%, which is much smaller than the sliding mode observer in [18]. Fig. 5.10 describes the convergence time for the adaptive gain sliding mode observer clearly. The initial SOC error decreases to smaller than 5% after 318 s. The convergence rate will be faster with a larger designed $\hat{\lambda}_1(0)$. The estimated terminal voltage from the proposed observer is nearly the same as the measured voltage in Fig. 5.11. In summary, the adaptive gain sliding mode observer has good robustness, not only on the initial state, but also on the model uncertainty. In this way, the equivalent circuit model with uncertainties described in Section 5.2, which achieves the trade-off between modeling simplification and accuracy, can be used for SOC estimation by the adaptive sliding mode observer. The SOC estimation error is kept in suitable range although the model has unavoidable errors in some SOC regions. Hence, the adaptive gain sliding mode observer brings convenience to both the modeling and estimation process.

In Figs. 5.12 and 5.13, the SOC estimation results and errors for the current pattern in Fig. 5.6 are depicted. The initial SOC is also set to incorrect values. Fig. 5.13 shows that the adaptive observer improves the estimation performance obviously. The largest estimation error after convergence decreases to the range of around 3%. The model error caused by a large current leads to a large estimation error from the sliding mode observer in [18], whereas this large error is effectively decreased by the adaptive sliding mode observer. It is verified that this sliding mode observer with adaptive gain has good performance on SOC estimation of Li-ion batteries.

The current file of the urban dynamometer driving schedule (UDDS) cycles for EVs is also tested for SOC estimation by the adaptive observer. The initial SOC is set to 0.1, in order to test the observer's robustness. The comparison and estimation results are depicted in Figs. 5.14 and 5.15. The improvement brought by the proposed observer is obvious.

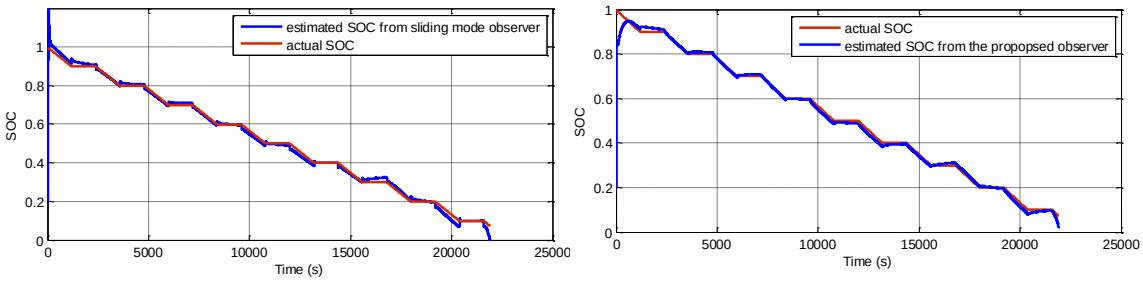

a) SOC estimation from sliding mode observer. b) SOC estimation from the adaptive observer.

Fig. 5.8. Estimated SOC compared with actual SOC.

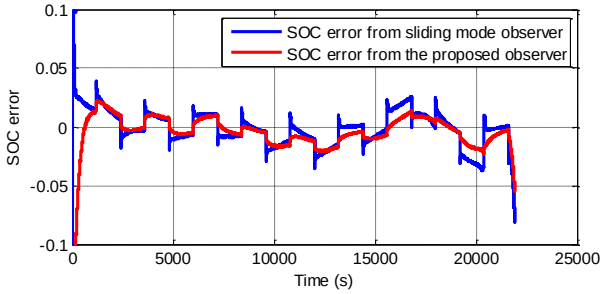

Fig. 5.9. SOC error comparison.

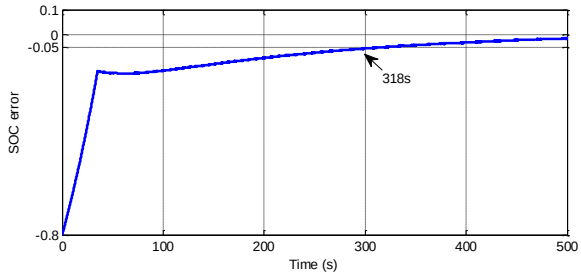

Fig. 5.10. The convergence time for the adaptive observer.

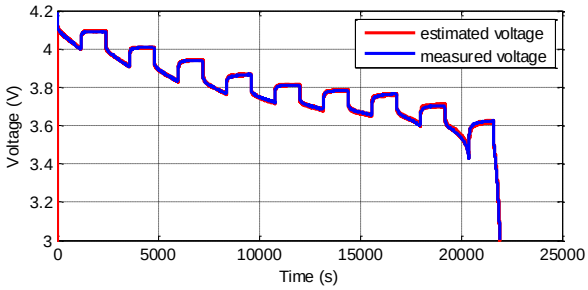

Fig. 5.11. Estimated voltage by the adaptive observer.

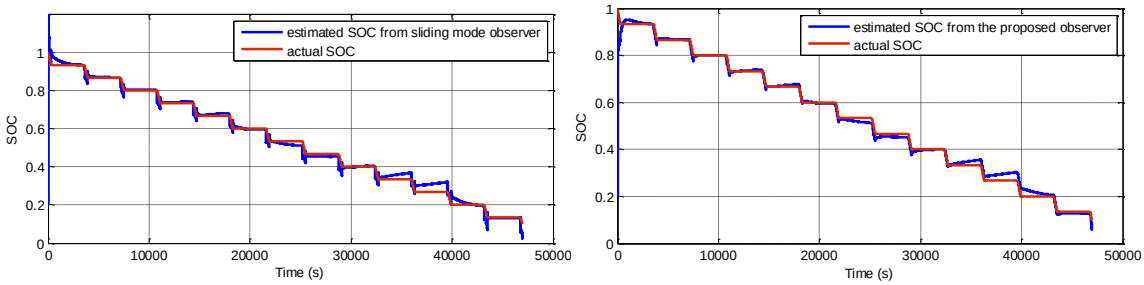

a) SOC estimation from sliding mode observer. b) SOC estimation from the adaptive observer.

Fig. 5.12. Estimated SOC compared with actual SOC (0.8C).

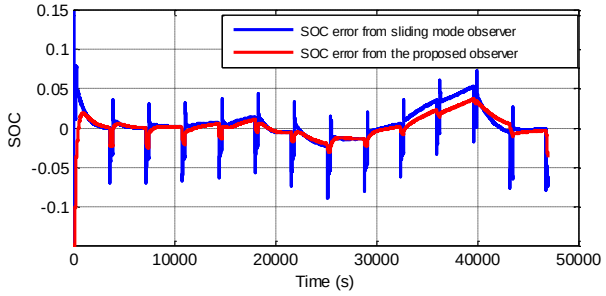

Fig. 5.13. SOC error comparison (0.8C).

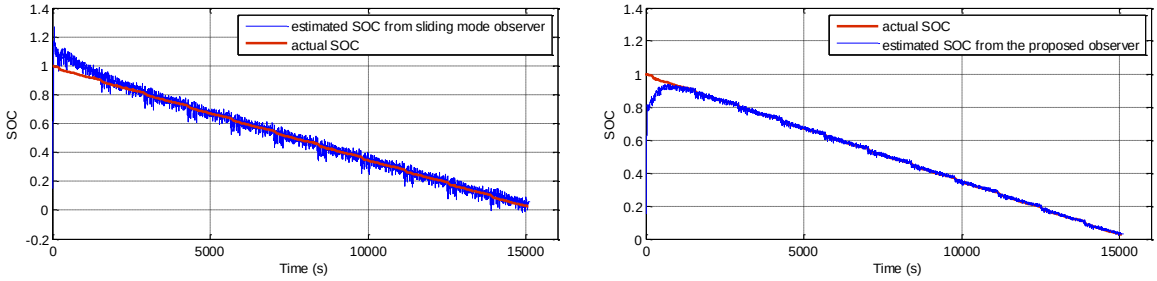

a) SOC estimation from sliding mode observer. b) SOC estimation from the adaptive observer.

Fig. 5.14. Estimated SOC compared with actual SOC (UDDS cycles).

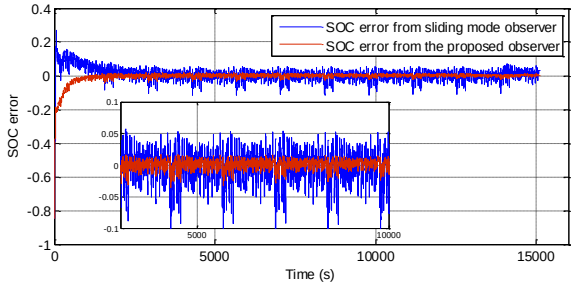

Fig. 5.15. SOC error comparison (UDDS cycles).

5.4 The Adaptive Observer Based on Sliding Mode Scheme for SOC and SOH Estimation

In this section, Li-ion battery SOH estimation is implemented. In the Li-ion battery's equivalent circuit model without the battery aging mechanism functions, SOH can be reflected and estimated by the circuit resistances. In the equivalent circuit model, the series resistance's quantity indicates the battery's aging level [83]. The increase of R_s induces the power fade directly, which is an important sign for battery aging. Therefore, the variation of R_s is estimated and taken to determine SOH in this chapter.

Excluding temperature effect, the R_s variation to SOC is incorporated in the R_s value here. The relationship of the estimated R_s versus SOC can be displayed online and SOH is determined by R_s estimation at the same SOC condition.

The Li-ion battery's SOH is set to 100% at beginning-of-life (BOL) and 0% at end-of-life (EOL). In [90], the R_s range at a chosen SOC during battery life time is defined by $R_{EOL} = 2R_{BOL}$. According to this range, an expression for SOH could be deduced from R_s by:

$$SOH = \frac{2R_{BOL} - R_s}{R_{BOL}} \times 100\% \tag{5.24}$$

where R_{BOL} is identified from a fresh battery. Hence, with the real-time knowledge of R_s, SOH can be indicated by (5.24).

In the system equations (5.8)-(5.11) and SOC observer equations proposed in Section 5.3.2, R_s is taken as the model parameter. Compared with SOC and other state variables in (5.8)-(5.11), R_s is regarded slowly time-varying. Thus, another adaptive observer scheme for slowly time-varying parameters as the SOH observer is proposed here. At each sampling step, the SOC observer and SOH observer work concurrently, applying the priori estimation from each other. Hence, the observers for the battery SOC estimation and SOH estimation could be executed simultaneously to estimate the battery's real-time SOC and SOH. The observer operation schematic is depicted in Fig. 5.16.

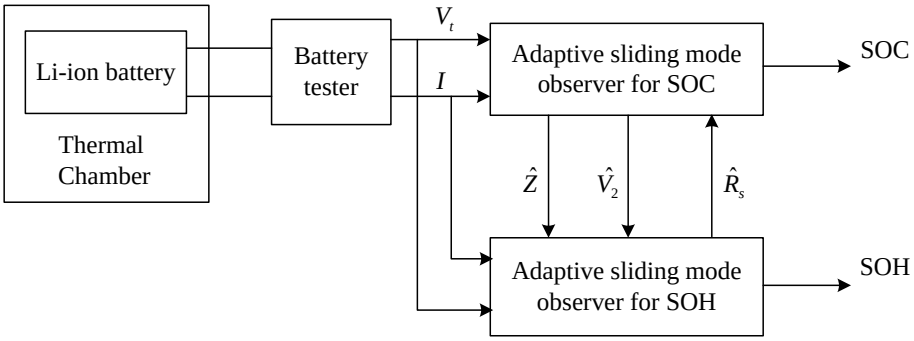

Fig. 5.16. The operation schematic for SOC and SOH estimation.

5.4.1 Adaptive Observer Based on Sliding Mode Scheme

Based on the SOC observer's form described in previous sections, the SOH observer is proposed and implemented in this section. Another series of observers of the form (5.20) are designed. The battery terminal voltage V_t is also taken as the measurement. The dynamics for V_t described in (5.3) is changed to:

$$\dot{V}_t = -V_d + b_1 I = -a_{52}V_2 - a_{51}V_1 + b_1 I = -a_{51}V_t + a_{51}g(Z) + (a_{52} - a_{51})V_2 + b_1 I + a_{51}IR_s \quad (5.25)$$

where $a_{51} = \dfrac{1}{R_1 C_1}$, $a_{52} = \dfrac{1}{R_2 C_2}$.

Assume Z and V_2 in (5.25) are the estimations from SOC observer and represented by $\hat{Z}$ and $\hat{V}_2$. Here, $\hat{Z}$ and $\hat{V}_2$ are regarded as known parameters. Considering modeling approximation, (5.25) is completed to:

$$\dot{V}_t = -a_{51}V_t + a_{51}IR_s + (a_{51}g(\hat{Z}) + (a_{52} - a_{51})\hat{V}_2 + b_1 I) + \Delta f_V \quad (5.26)$$

where Δf_V represents the voltage uncertainty. The expression $a_{51}g(\hat{Z}) + (a_{52} - a_{51})\hat{V}_2 + b_1 I$ in (5.26) can be regarded as system input.

As the variable to be estimated by SOH observer, R_s is taken as the state variable for (5.26). All the other battery model parameters are set the same to the identified parameters in Section 5.2. Then, the adaptive sliding mode observer for (5.26) is designed as:

$$\dot{\hat{V}} = -a_{51}\hat{V} + a_{51}g(\hat{Z}) + (a_{52} - a_{51})\hat{V}_2 + b_1 I + a_{51}I\hat{R}_s + \hat{\lambda}_V(t)\frac{e_V}{|e_V| + \delta_V} \quad (5.27)$$

where $\hat{V}$ represents the estimation for V_t and $\hat{R}_s$ represents the estimation for R_s from the SOH observer (5.27); $e_V = V_t - \hat{V}$; δ_V is a small positive scalar, and

$$\dot{\hat{\lambda}}_V(t) = \begin{cases} 2\alpha_V |e_V|, \ if \ |e_V| > 2\delta_V \\ 0, \quad else \end{cases},$$

where α_V describes the adaptive gain $\hat{\lambda}_V$'s adjusting rate. Then,

$$\dot{e}_V = -a_{51} e_V + \Delta f_V - \hat{\lambda}_V(t) \frac{e_V}{|e_V| + \delta_V} + a_{51} I (R_s - \hat{R}_s) \tag{5.28}$$

Define the Lyapunov candidate function as $V_V = {e_V}^2 + {\alpha_V}^{-1}(0.5\hat{\lambda}_V - \lambda_V)^2$, where λ_V is set a constant that satisfies $\lambda_V > \max(|\Delta f_V| + |a_{51} I (R_s - \hat{R}_s)|)$. Taking the same convergence proof in (5.22) and (5.23), $\dot{V}_V < -\frac{2}{3}\delta_V \hat{\lambda}_V(0)$. e_V and $\dot{e}_V$ are bounded in small range in finite time. Assume Δf_V is negligible in (5.26). Thus, when $I \neq 0$,

$$e_R \approx \frac{1}{a_{51} I} \hat{\lambda}_V(t) \frac{e_V}{|e_V| + \delta_V} \tag{5.29}$$

where $e_R = R_s - \hat{R}_s$.

The dynamics of R_s is modeled as: $R_s = R_s + \Delta R_s$, where ΔR_s describes R_s variation. Hence, the dynamics for R_s is described as:

$$\dot{R}_s = \Delta f_R \tag{5.30}$$

where Δf_R represents R_s's variation caused by SOC and model uncertainty during the estimation process. It should be mentioned that (5.30) could be added a positive constant describing R_s's increasing rate in long run [90, 91]. In practice, the battery aging effect changes R_s by a very slow rate. R_s gets several percentage's increase after hundreds of cycles [83]. Hence, the increasing rate is very small. In this section, only the proposed adaptive observer's performance is tested. Hence, the increasing rate of R_s is not incorporated in (5.30).

As R_s stays in a small range and varies slowly, it is sensitive to the observer gain. Thus, the adaptive sliding mode observer is also applied to achieve suitable gain. The observer for R_s is designed as:

$$\dot{\hat{R}}_s = \hat{\lambda}_R(t)\frac{e_R}{|e_R| + \delta_R} \tag{5.31}$$

where $\dot{\hat{\lambda}}_R(t) = \begin{cases} 2\alpha_R |e_R|, \; if \; |e_R| > 2\delta_R \\ 0, \quad else \end{cases}$,

δ_R and α_R are designed manually. Then, the error dynamics is:

$$\dot{e}_R = \Delta f_R - \hat{\lambda}_R(t)\frac{e_R}{|e_R| + \delta_R} \tag{5.32}$$

Based on conclusions of (5.23), e_R reaches the bound $|e_R| \leq 2\delta_R$ in finite time.

When the current is zero, e_R in (5.29) is set to zero and the observer (5.31) is temporarily suspended. The R_s estimation maintains constant until non-zero current applies.

5.4.2 Estimation Results and Discussion

To verify the proposed observer scheme's performance, the estimation for SOC and R_s are implemented in one test. All the SOC observer parameters are set the same to Section 5.3.3. The parameters in the SOH observer (5.27) and (5.31) are set as: $\hat{\lambda}_V(0) = 0.001$, $\alpha_V = 0.0000001$, $\delta_V = 0.000001$, $\hat{\lambda}_R(0) = 0.0000005$, $\alpha_R = 0.0000001$, $\delta_R = 0.000001$.

First, the current pattern in Fig. 2.6 is tested. The R_s value calculated at every 0.1 SOC in Fig. 4.1 a) is taken as the actual R_s. The initial R_s is set to 0.08 Ω, the actual initial R_s. The R_s estimation is depicted in Fig. 5.17. It is obvious that R_s stays constant when the SOH observer is suspended with zero current. The estimation results for R_s versus SOC compared with the actual R_s at every 0.1 SOC are shown in Fig. 5.18. It is verified that $\hat{R}_s$ tracks R_s with good performance. Meanwhile, the SOC estimation results and the estimated battery voltage $\hat{V}_t$ from the SOC observer are shown in Figs. 5.19 and 20. They also show good estimation performance. Then, an incorrect initial R_s is set to 0.07 Ω. The

estimation results are described in Fig. 5.21. The estimated R_s converges to the real R_s and then tracks R_s in good accuracy. It verifies that the proposed observer has robustness on the initial R_s value. The series resistance R_s is accurately estimated by the SOH observer and SOH can be simply determined by (5.24) using R_{BOL} from a fresh battery.

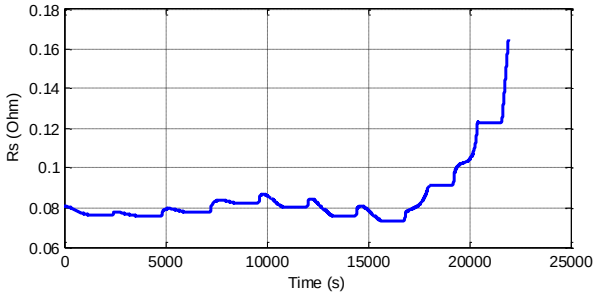

Fig. 5.17. Estimated R_s.

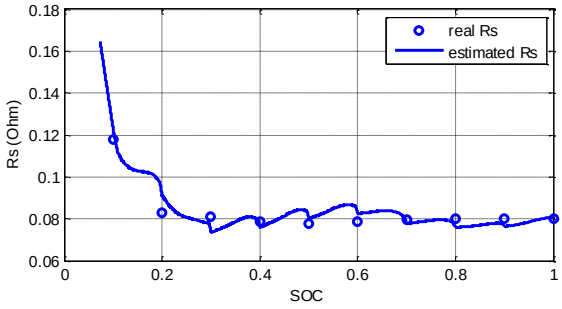

Fig. 5.18. Estimated R_s versus SOC.

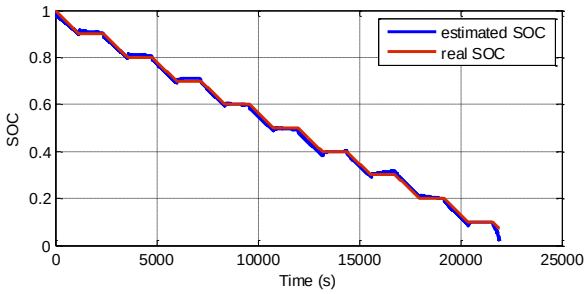

Fig. 5.19. Estimated SOC from the SOC observer compared with actual SOC.

The UDDS cycles for EVs are also tested on the Li-ion battery for SOC and SOH estimation by the proposed observer scheme. The initial observer gain is changed as $\hat{\lambda}_1(0) = 0.1, \hat{\lambda}_V(0) = 0.000001$. The SOC and SOH estimation results are shown in Figs. 5.22 and 5.23. They also show good estimation performance for both the SOC and SOH

observers.

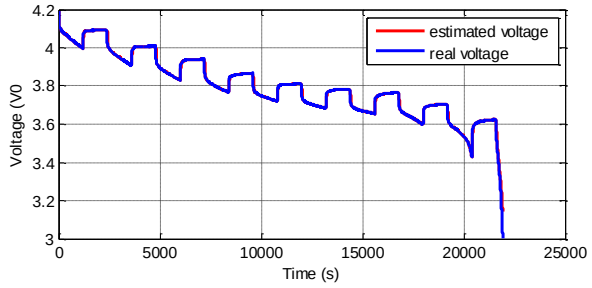

Fig. 5.20. Estimated voltage from the SOC observer compared with measured voltage.

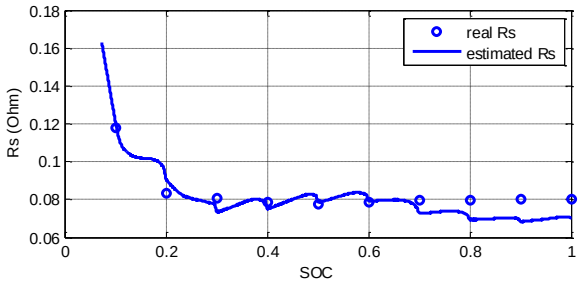

Fig. 5.21. Estimated R_s versus SOC (incorrect initial R_s).

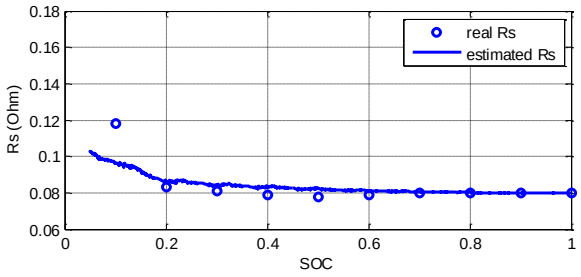

Fig. 5.22. Estimated R_s versus SOC (UDDS cycles).

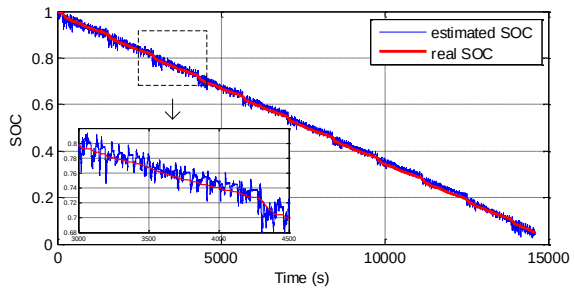

Fig. 5.23. SOC estimation (UDDS cycles).

5.5 Summary

In this chapter, the SOC and SOH of Li-ion batteries are estimated simultaneously by an adaptive observer scheme. Firstly, the equivalent circuit model with uncertainties is established. All the approximation steps in battery modeling process and inevitable model errors are described as system uncertainties. Then, the sliding mode observer in [18] is designed to estimate SOC for the model. An adaptive gain observer based on the sliding mode technique is also applied to improve the estimation performance. Compared with the conventional sliding mode observer, the adaptive sliding mode observer effectively improves SOC accuracy. Then, an adaptive observer based on the sliding mode scheme to estimate SOC and SOH simultaneously is proposed. The estimation results show that the estimation performances for Li-ion battery SOC and SOH are both accurate and robust.

Compared with the SOC estimation methods proposed in Chapter 3 and Chapter 4, the combination of equivalent circuit model with uncertainties and the adaptive sliding mode observer presented in this chapter is more suitable for EV applications. With more convenient modeling process and the estimation algorithm with high accuracy, no demand for system noise and light computation load, the proposed SOC estimation method in this chapter is applicable in practice.

Based on the improved results of the Li-ion battery SOC and SOH estimation by the proposed observer in this chapter, the topics relevant to the Li-ion battery pack's operation in EVs will be discussed in the next two chapters.

Chapter 6 Cell Equalization System For Series Connected Li-ion Batteries

In the previous chapters, research on a single Li-ion battery was discussed. From this chapter, Li-ion battery pack operation status in electric vehicles (EVs) will be emphasized. In this chapter, the methods of cell equalization in a Li-ion battery pack are studied and improved. Section 6.1 gives an introduction to the functions and significances of cell equalization. In Section 6.2, the equalization method using switched capacitors is established and improved to form a chain structure. Then, the cell equalization topology by modules with chain switched capacitors is proposed and tested. In Section 6.3, the cell equalization topology by modules with double switched capacitors is proposed based on the single switched capacitor method. State of charge (SOC) and state of health (SOH) of Li-ion batteries are used to determine the cell charge transfer paths. Section 6.4 summarizes this chapter.

6.1 Introduction

On the basis of battery SOC and SOH estimation, to implement Li-ion battery voltage equalization in one string is another important topic. To provide high voltage and power, Li-ion batteries in EVs are connected in series and parallel to constitute battery packs. In one series-connected battery string, the charging and discharging currents are the same for the cells without any equalization methods. However, an individual cell may have certain differences in parameters when it is manufactured. In this way, it is possible that the battery cells in the same string get different voltages and SOC during EV driving. If the difference grows bigger, irretrievable damage such as over-charging and over-discharging will be caused by cell imbalance. Therefore, the cell imbalance phenomenon must be avoided. Implemented cell equalization methods are essential in battery packs.

In EV applications, the cell equalization circuit also tries to obtain maximum usable capacity from battery pack [94]. An out-of-balancing cell may approach the preset cut-off voltage prematurely during charging or discharging, but cell equalization measures can control the higher or lower voltage cells until the rest of cells can catch up [94]. In this chapter, the equalization method using switched capacitors for its simple implementation

and direct control method is studied and some improved topologies based on the conventional switched capacitor method are proposed.

6.2 Cell Equalization Method Using Switched Capacitors

The equalization circuit using switched capacitors performs very simple topology and control mode. The capacitors are taken as energy transfer and storage devices. It is verified in [103] that the equalization results are independent on the equalization capacitor capacity, switching frequency and battery characteristics.

6.2.1 Cell Equalization with Switched Capacitors

An elementary circuit schematic for cell equalization method with switched capacitors, named adjacent switched capacitors, is depicted in Fig. 6.1, where the series-connected cells are represented by $Cell_1$~$Cell_4$ and the equalization capacitors are represented by C_1~C_3. The single-pole, double-throw switch (SPDT) is used in the equalization circuit.

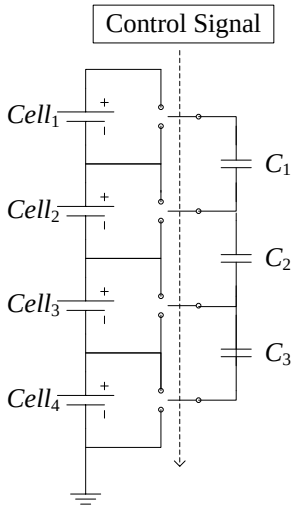

Fig. 6.1. Cell equalization using adjacent switched capacitors.

All the switches are under the same control signal. A pulse signal as shown in Fig. 6.2 is used to make the switches operate up and down. The switching frequency is fixed as $1/T_s$. The switch up and down states last for the same time interval, i.e.,

$$D_1 = D_2 \tag{6.1}$$

where D_1 and D_2 represent the duty cycle. A very short time interval d, defined by dead time, is set in the switching function to avoid the possibility of shoot through failure

during the equalization process [103].

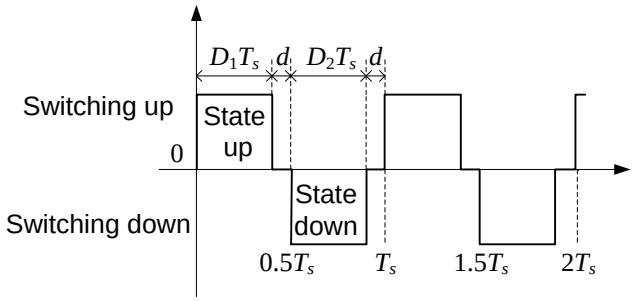

Fig. 6.2. Switching function.

When the switches are controlled at up state, the capacitors of C_1~C_3 are connected to $Cell_1$~ $Cell_3$ in parallel through the switches. When the switches are controlled at down state, the capacitors are connected to $Cell_2$~ $Cell_4$ in parallel. The circuit diagrams for up state and down state are depicted in Fig. 6.3. Thus, each capacitor is connected alternatively to adjacent cells. The voltages across the equalization capacitors are the same as the average voltage for the two adjacent cells connecting with them. Then,

$$V_{C1} = \frac{1}{2}(V_{Cell1} + V_{Cell2}),\ V_{C2} = \frac{1}{2}(V_{Cell2} + V_{Cell3}),\ V_{C3} = \frac{1}{2}(V_{Cell3} + V_{Cell4}). \tag{6.2}$$

Adjacent batteries are equalized through the capacitors by transferring charge from higher-voltage cell to lower-voltage cell. The average currents transferring charging between cells and capacitors are represented by (6.3) (assuming $V_{Cell1} > V_{Cell2}$) [104]:

$$I_{Cell1} = D \cdot \frac{V_{Cell1} - V_{C1}}{R_{eq}},\ I_{Cell2} = D \cdot \frac{V_{C1} - V_{Cell2}}{R_{eq}}, \tag{6.3}$$

where R_{eq} represents the sum of the resistances of the battery, switched capacitor and switch.

For equalization circuit with adjacent switched capacitors, no sensing circuit or closed-loop control is needed [105]. The switches operate repeatedly as long as there is imbalance between cells. The equalization process stops automatically when the imbalance disappears. The equalization circuit structure can also be extended easily. If the series string is extended to N cells, N-1 capacitors will be needed and the circuit structure will be very similar to Fig. 6.1.

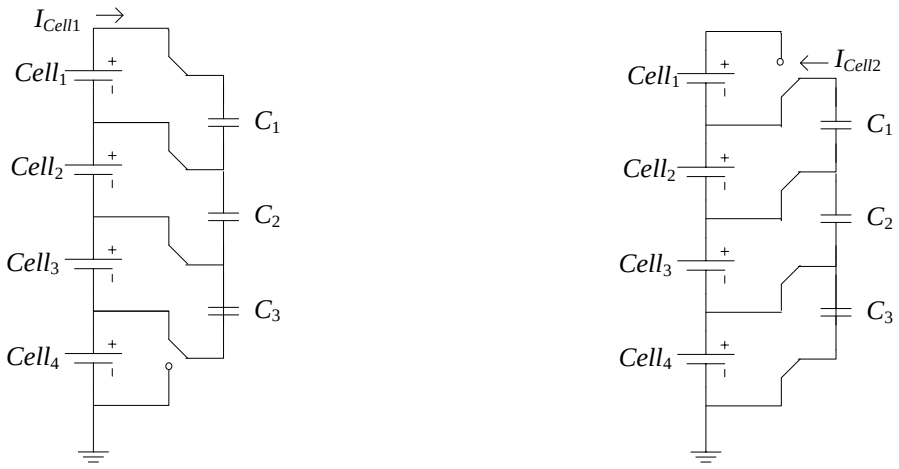

a) State up. b) State down.

Fig. 6.3. Equalization circuit schematics for adjacent switched capacitors.

However, the equalization speed for the above circuit may be slow in some conditions. For example, in a long string with imbalance occurring between the first cell and the last cell, the charge will be transferred through all the cells and capacitors in the string during equalization. The equalization time will be long. To solve such problems and increase the cell equalization speed, some new circuit schematics using switched capacitors are studied and proposed in the next sections.

6.2.2 Cell Equalization with Chain Structure Switched Capacitors

In [104] and [105], new topologies using equalization capacitors are proposed and tested. Compared with the double-tiered structure in [105], the chain structure proposed in [104] increases the equalization speed between the two cells in both string edges more effectively. In this section, the chain structure of switched capacitors for cell equalization is analyzed and established.

Based on the existing equalization circuit in Fig. 6.1, one capacitor and four switches are added to form a chain structure as shown in Fig. 6.4. The added switches are also controlled by the same switching function depicted in Fig. 6.2. When C_1~C_3 are in the up state, C_4 is connected with $Cell_4$ with corresponding switches turned on. When C_1~C_3 are in the down state, C_4 is connected with $Cell_1$. The circuit diagrams in two states are shown in Fig. 6.5. Battery charge can be transferred between the first cell and the last cell through C_4 with no need to go through other cells or capacitors. Thus, the added

equalization capacitor establishes the connection between $Cell_1$ and $Cell_4$ and the imbalance between the two cells is alleviated directly. A detailed analyze is given in [104].

When using the chain structure switched capacitor for cell equalization, the equalization topology can also be extended with increased battery string scale. *N* capacitors are needed for *N* series-connected cells.

To test the improvement of the equalization schematic with chain structure switched capacitors compared with adjacent switched capacitors, some simulations are done in Matlab/Simulink. A string of four cells are taken to test the equalization methods.

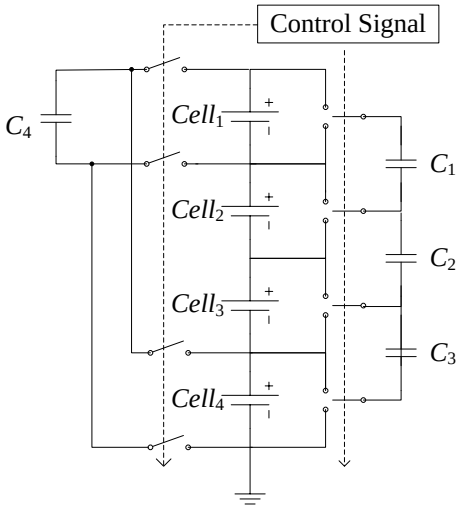

Fig. 6.4. Cell equalization using switched capacitors with chain structure.

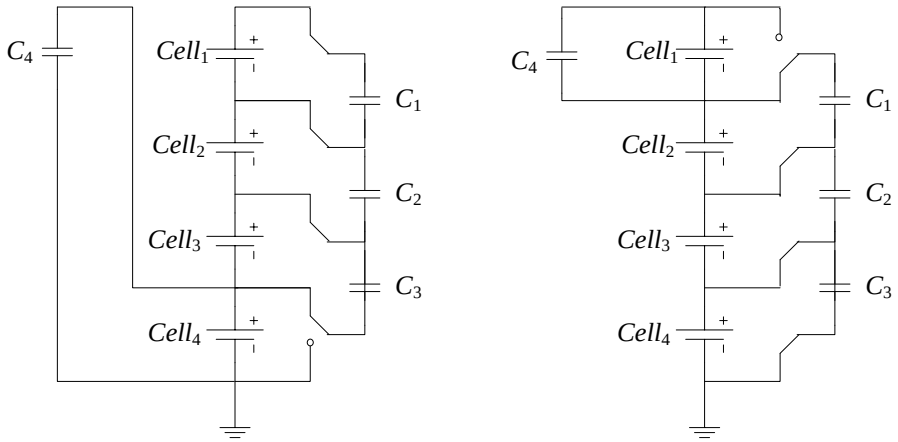

a) State up. b) State down.

Fig. 6.5. Equalization circuit schematics for switched capacitors with chain structure.

In most existing literatures about cell equalization systems, the Li-ion battery is modeled by a capacitor with a resistor, which is simple but the battery dynamic characteristics is not described accurately. In this section, the equivalent circuit model with two RC networks implemented in Chapter 4 for Li-ion batteries is applied to simulate the battery behavior, which is closer to practical applications. The initial SOC of the four cells are set as 0.5, 0.3, 0.2, and 0.1, which is with obvious imbalance phenomenon. To show the equalization effect more efficiently in simulation, the battery's capacity is reduced to one thousandth of the nominal capacity at 9.36 *coulomb*. The cells' SOC can be obtained by the methods introduced in the previous chapters, which is not described in this chapter. The switched capacitors are set at 0.01 F with the switching frequency of 10 Hz considering the simulation speed. The duty ratio is set to 49%. The switched capacitor method can achieve battery equalization regardless the battery's operation status. The battery string is tested under charging, discharging and resting operations. All the equalization results including SOC and voltages of the cells for the two switched capacitor structures are shown in Fig. 6.6 to Fig. 6.11.

The results indicate that cell equalization is achieved by adding equalization capacitors. Both SOC and voltages of the cells tend to be the same during operation. The equalization results also show obvious improvement brought by the chain structure switched capacitors. The equalization time is decreased for the chain structure switched capacitor topology. When the battery string is charged, the equalization time in Fig. 6.6 is nearly one third of the time in Fig. 6.9. Similar results are obtained for battery operations of resting and discharging.

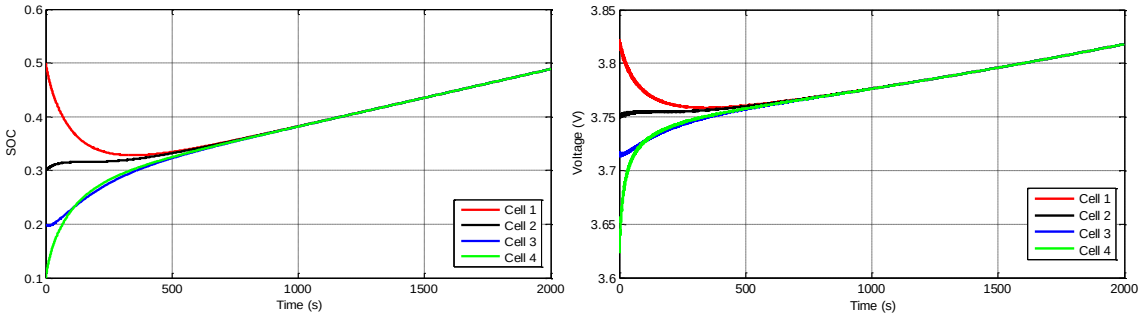

a) SOC for cells. b) Voltages for cells.

Fig. 6.6. Equalization results for chain switched capacitor circuit (charging).

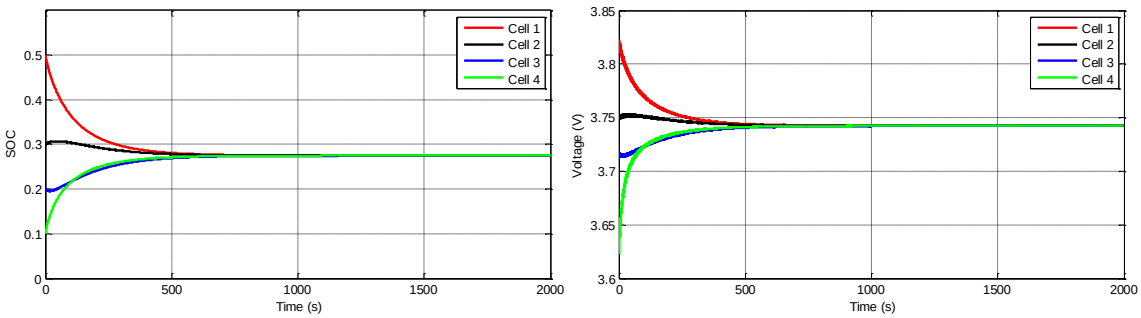

a) SOC for cells. b) Voltages for cells.

Fig. 6.7. Equalization results for chain switched capacitor circuit (resting).

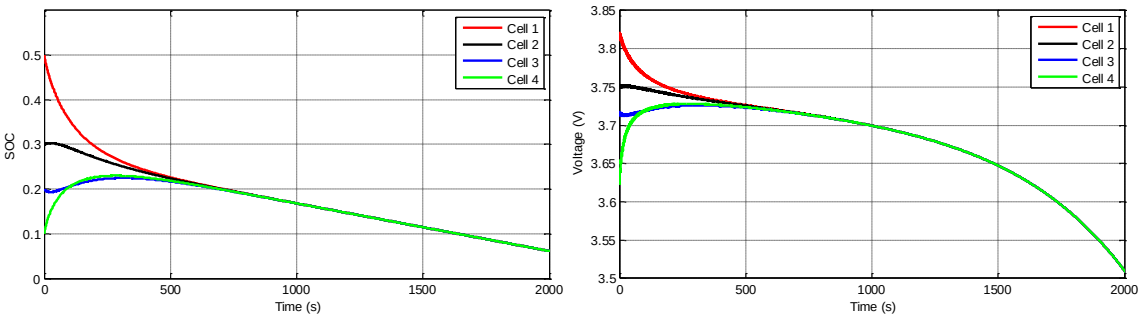

a) SOC for cells. b) Voltages for cells.

Fig. 6.8. Equalization results for chain switched capacitor circuit (discharging).

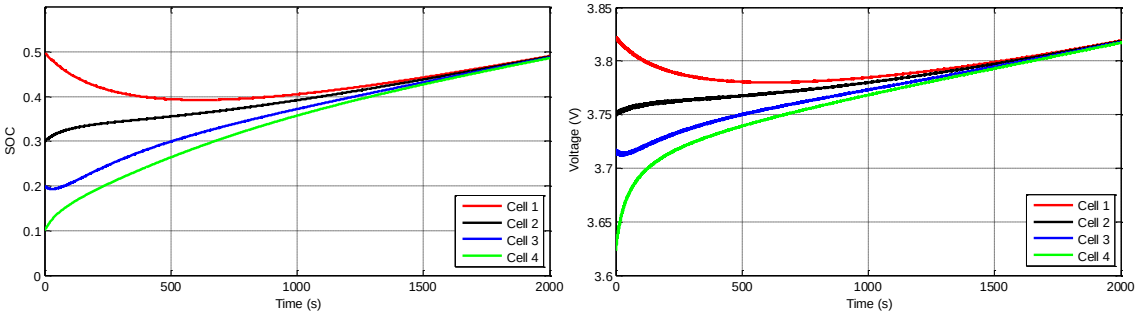

a) SOC for cells. b) Voltages for cells.

Fig. 6.9. Equalization results for adjacent switched capacitor circuit (charging).

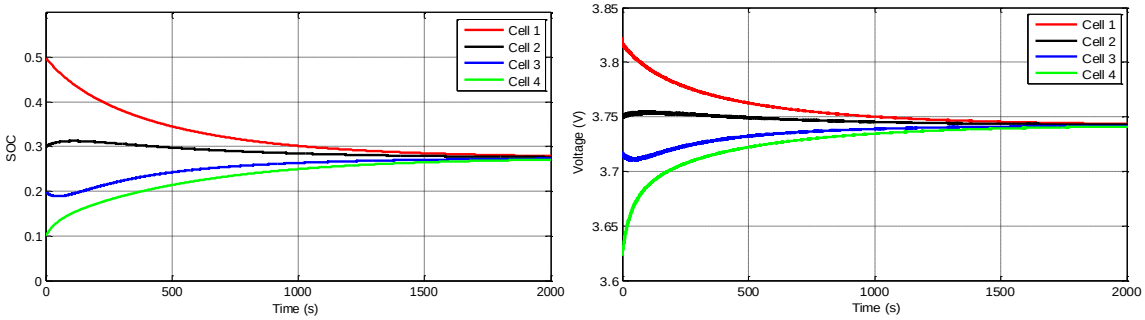

a) SOC for cells. b) Voltages for cells.

Fig. 6.10. Equalization results for adjacent switched capacitor circuit (resting).

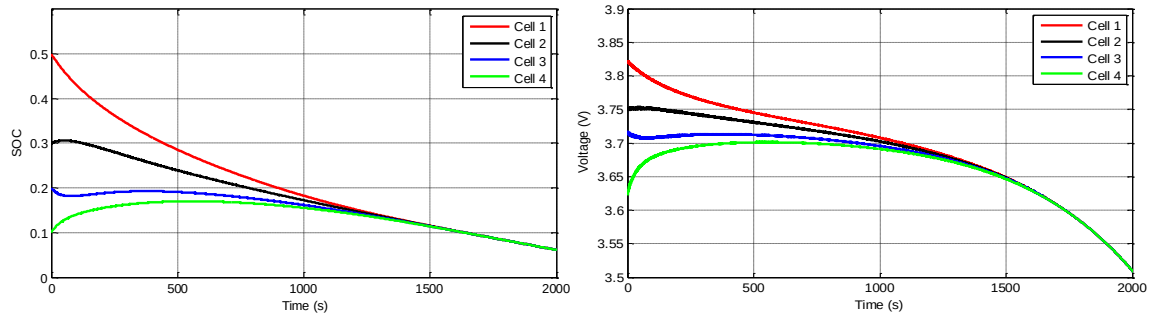

a) SOC for cells. b) Voltages for cells.

Fig. 6.11. Equalization results for adjacent switched capacitor circuit (discharging).

6.2.3 Cell Equalization by Modules with Chain Structure Switched Capacitors

In the EV's battery pack, the battery string must be long to supply enough voltage. In a long string, all the series-connected batteries can be grouped by several modules. The battery string made up by modules is shown in Fig. 6.12. With the modularization concept, it is convenient to design the equalization topology. Inside one module, there are much fewer cells to consider than the whole string, bringing easy designing procedure and flexibility. Furthermore, each module can be taken as one cell with larger capacity and the equalization methods for cells can be applied to modules similarly. The possible problems caused by long string, including complex equalization circuit topology, difficult implementation, low equalization efficiency and speed [108], could be mitigated and even solved by designing cell equalization topology by modules. The voltage stress on the equalization components including capacitors and switches will be lower inside each module [108].

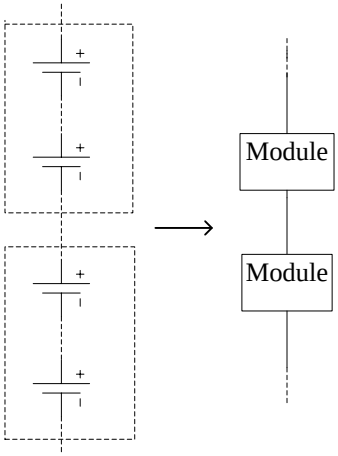

Fig. 6.12. A battery string made up by modules.

Although the equalization method using chain structure switched capacitors performs faster, the voltages on the switches for the chain capacitor are larger than one cell voltage. With *N* cells in the string, the voltages across the chain structure switches equal to the voltage sum of the other *N*-1 cells. If the cell number *N* is large, the voltages across the chain structure switches will also be large. The modularization concept can solve this problem. Whether *N* is large or not, the switches for the chain structure only need to endure the voltage of a single module.

In this section, the equalization schematic of chain structure switched capacitors combined with module concept is proposed. In each module there exist four cells with chain structure switched capacitors. Thus, the voltages on the equalization capacitors and switches will not be larger than 17 V. The equalization speed is fast inside one module and between modules because fewer steps are taken to equalize all the cells. The proposed circuit topology is shown in Fig. 6. 13. A string of eight cells grouped in two modules are tested in simulation. An equalization capacitor for adjacent modules is designed in the equalization system with the same capacity and switching frequency to other equalization capacitors.

To analyze the equalization circuit in the battery string, $Cell_1$ in Fig. 6.13 is taken as an example. Obviously, $Cell_1$ is adjacent to $Cell_2$ and $Cell_4$. Only through one equalization step the imbalance between $Cell_1$ and $Cell_2$, $Cell_1$ and $Cell_4$ could be alleviated. Inside *Module* 1, only $Cell_3$ is not adjacent to $Cell_1$. The charge transferred between $Cell_1$ and $Cell_3$ will be realized in the second step. Moreover, the two modules are equalized by the

equalization capacitor C_9 for modules. The imbalance between $Cell_1$ and the cells in the *Module* 2 will be mitigated from the first equalization step by the switched capacitor for adjacent modules. All the switches are controlled by fixed switching functions and the control signals are simple. Equalization will be achieved between cells inside one module and between modules simultaneously for the proposed topology. Thus, the equalization speed for the whole string will be increased by modularization.

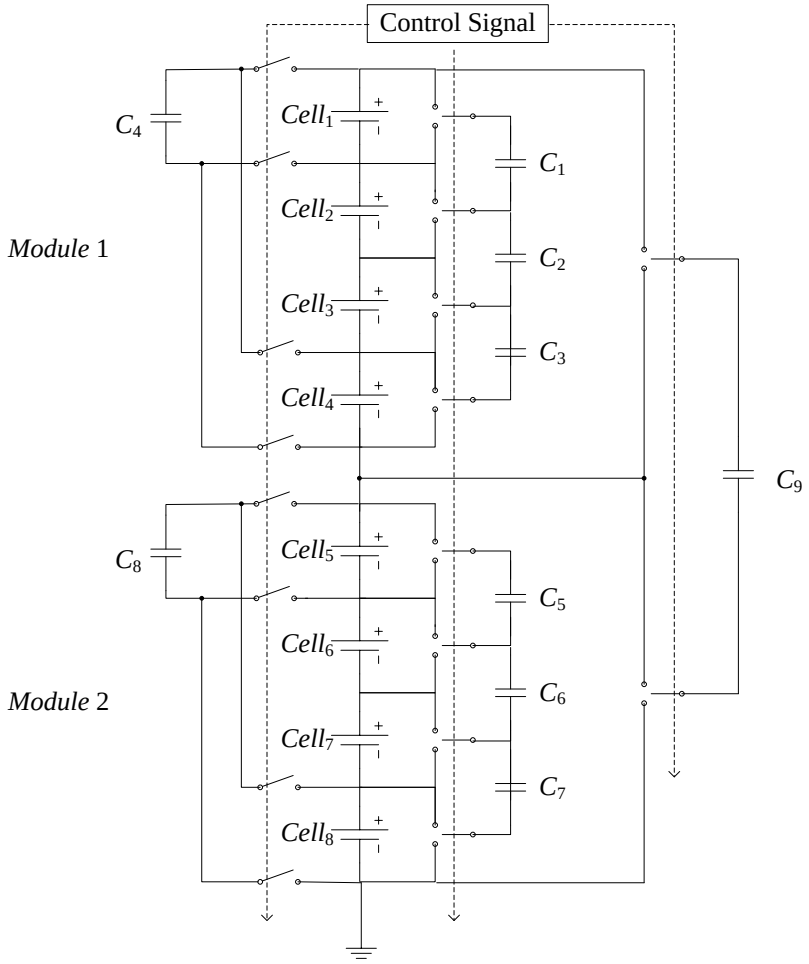

Fig. 6.13. Equalization topology by modules with chain structure switched capacitors.

The proposed equalization schematic is tested in Matlab/Simulink. Besides, the same battery string of eight cells using the chain structure capacitor equalization circuit without grouped modules is also tested as a comparison. All the circuit parameters including the Li-ion battery model and equalization components are set the same as in Section 6.2.2. The cells are set with different initial SOC as in Table 6.1:

Table 6.1. Initial SOC for the cells in the string.

Cell No.	1	2	3	4	5	6	7	8
SOC	0.8	0.7	0.5	0.3	0.5	0.3	0.2	0.1

The battery operations of charging, resting and discharging are tested separately. The results are shown in Figs. 6.14-6.19. The equalization effect is obvious for the proposed topology. For the three operation conditions, all the eight cells are equalized in around 500 s. Both SOC and voltages of the cells become nearly the same after 500 s. It also indicates that the equalization effect on cells in one module and between modules occurs simultaneously. Comparing the results from the two equalization methods, the equalization circuit by modules significantly increases the equalization speed.

Then, the initial SOC are set similar for the cells inside one module, but with larger difference between the two modules. The initial SOC are shown in Table 6.2. EV's UDDS cycle with varying current is applied in the test. The equalization results are shown in Fig. 6.20. It is obvious that the cells inside one module are equalized. Meanwhile, the two modules are also equalized.

Table 6.2. Initial SOC for the cells in the string (UDDS cycle).

Cell No.	1	2	3	4	5	6	7	8
SOC	0.82	0.87	0.89	0.8	0.98	0.96	0.95	0.99

Although the new proposed topology needs more equalization components, resulting in larger circuit size and higher cost, the equalization speed improvement is obvious and this advantage outweighs the drawback. The control mode is not more complex for the proposed topology and the performance improvement is significant compared to the method without modularization.

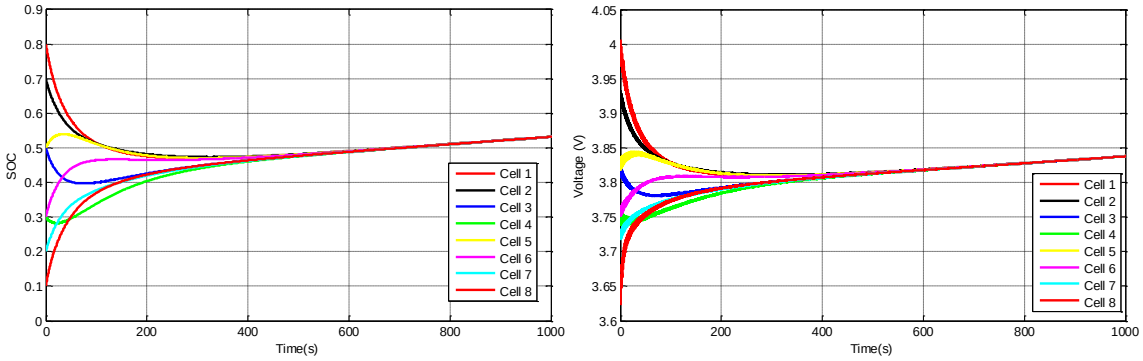

a) SOC for cells. b) Voltages for cells.

Fig. 6.14. Equalization results for chain switched capacitor circuit in modules (charging).

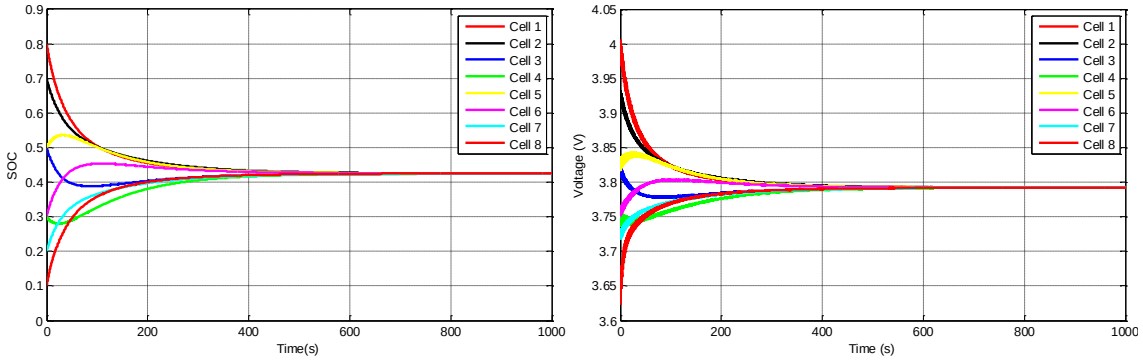

a) SOC for cells. b) Voltages for cells.

Fig. 6.15. Equalization results for chain switched capacitor circuit in modules (resting).

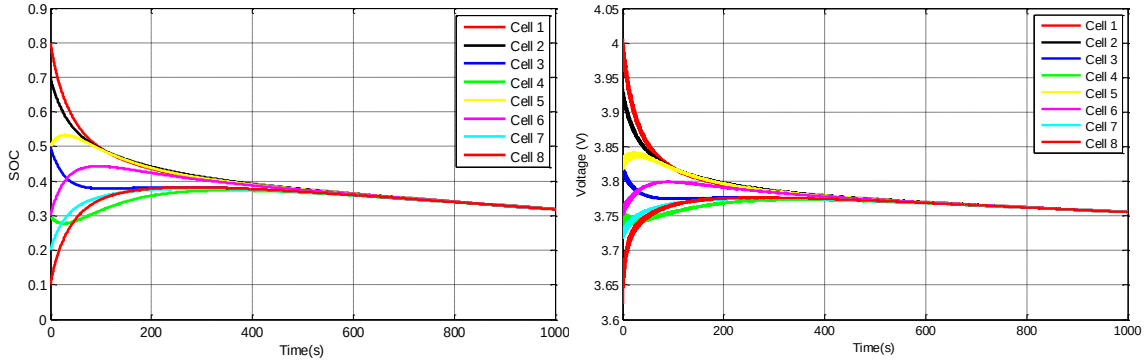

a) SOC for cells. b) Voltages for cells.

Fig. 6.16. Equalization results for chain switched capacitor circuit in modules (discharging).

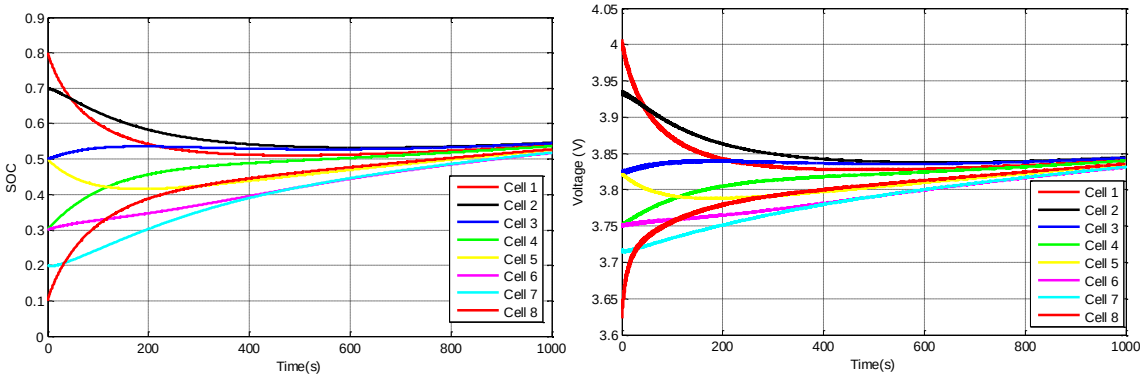

a) SOC for cells. b) Voltages for cells.

Fig. 6.17. Equalization results for chain switched capacitor circuit without modules (charging).

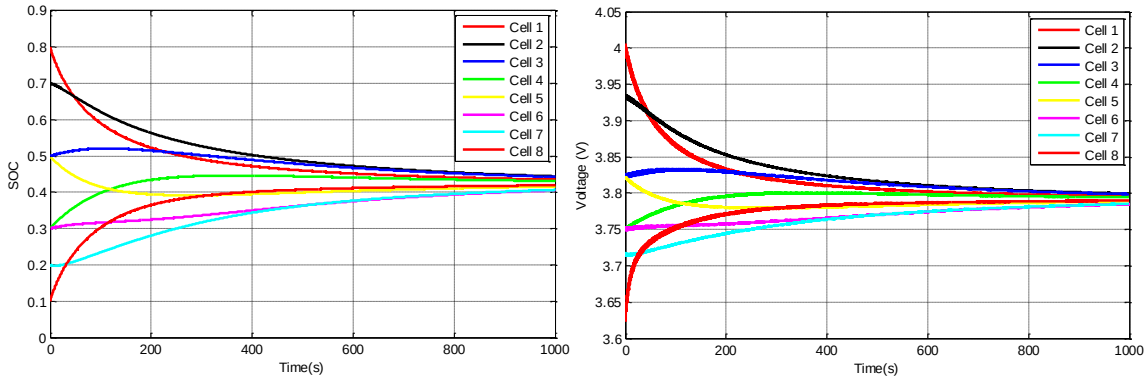

a) SOC for cells. b) Voltages for cells.

Fig. 6.18. Equalization results for chain switched capacitor circuit without modules (resting).

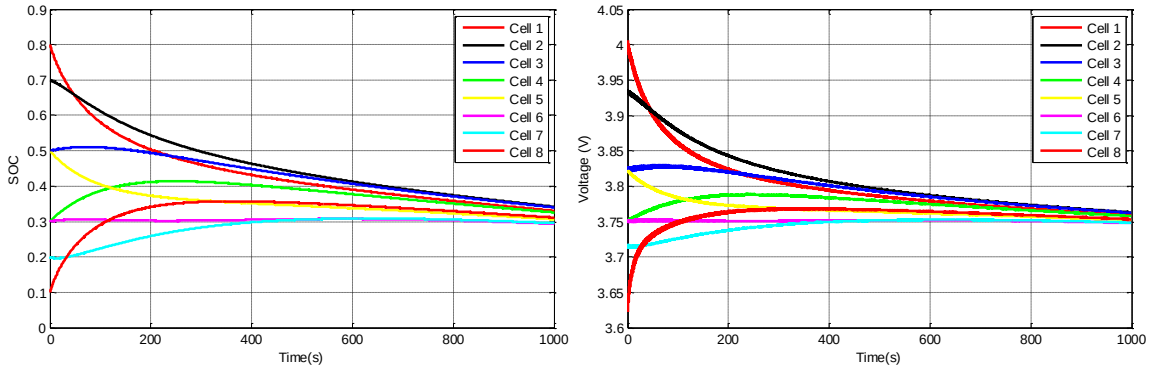

a) SOC for cells. b) Voltages for cells.

Fig. 6.19. Equalization results for chain switched capacitor circuit without modules (discharging).

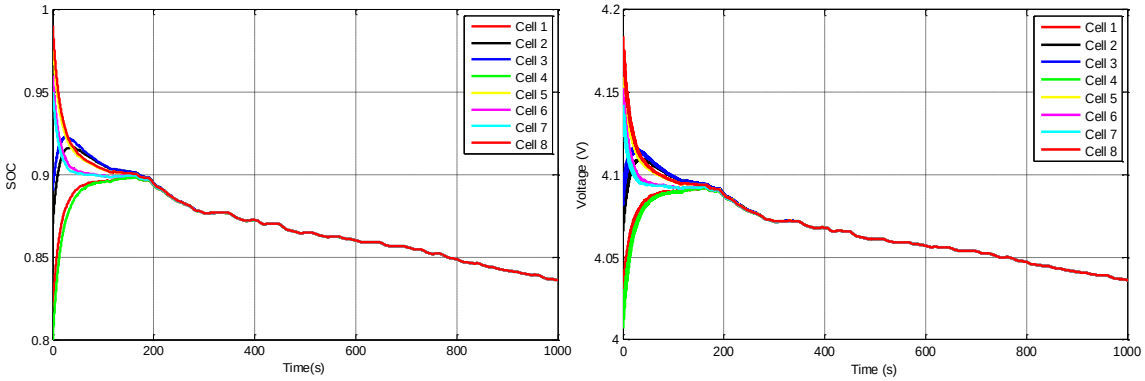

a) SOC for cells. b) Voltages for cells.

Fig. 6.20. Equalization results for chain switched capacitor circuit in modules (UDDS cycle).

6.3 Cell Equalization Combining Battery SOC and SOH Estimation

In [94, 107, 137], the equalization structure with single switched capacitor is proposed and tested. Different from the equalization circuits with multiple switched capacitors in Sections 6.2.1 and 6.2.2, only one equalization capacitor is needed for one string of N cells. This single switched circuit topology is simpler with higher efficiency and lower energy lost. It is a cell-to-cell method with more direct equalization effect. The charge is removed from the highest-energy cell and delivered to the lowest-energy cell at each equalization step. Li-ion battery SOC estimation indicating battery energy is often taken as the reference for selecting the equalizing cells. Since SOC and SOH both have effect on the Li-ion battery's behaviors, SOC and SOH estimation results are taken as the control signals for cell equalization in this section.

6.3.1 Cell Equalization with Single Switched Capacitor Combining SOC Estimation

The cell equalization schematic with a single switched capacitor topology is shown in Fig. 6.21. To determine the charge transfer path, particular control strategies identifying the cells with the highest and lowest energy and controlling switches on and off are needed. In the previous sections of this chapter, only cell voltages are concerned, whereas it has been known that Li-ion battery voltage may not reflect the real condition of cell energy. For Li-ion batteries, the voltage difference is very small when SOC is in medium range. Besides, considering the possible noise from the voltage sensor in circuit, it is not suitable to select the equalizing cells by referring to cell voltages.

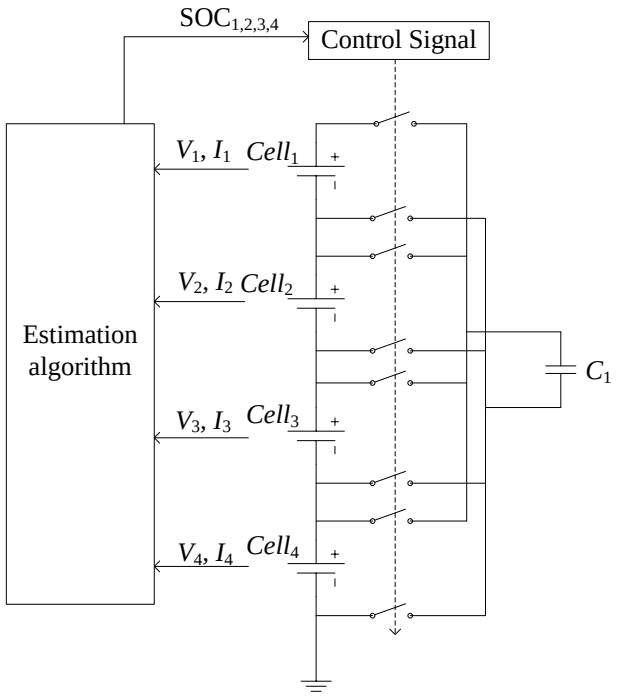

Fig. 6.21. Equalization topology for single switched capacitor.

To improve the equalization efficiency, SOC is taken as the reference. The SOC estimation can be provided by the algorithm described in previous chapters, which will not be focused in this chapter. The single switched capacitor topology is tested in simulation. All the circuit parameters are set the same as in Section 6.2.2. The initial SOC of the cells are set as 0.8, 0.7, 0.5, and 0.3, respectively. The operation conditions of resting, charging and discharging are tested for this topology. The equalization results including SOC and voltages of the cells are depicted in Figs. 6.22-6.24.

The results reveal that the single switched capacitor achieves equalization effect efficiently for different battery operations. At first, the cell with the highest SOC, $Cell_1$ transfers its charge to the cell with the lowest SOC, $Cell_4$, whereas $Cell_2$ and $Cell_3$ are not in the equalization process. In other words, only one pair of cells is being equalized at one equalization step. Some improvement will be proposed in the next section to achieve multiple efficient charge transfer paths within the same equalization step.

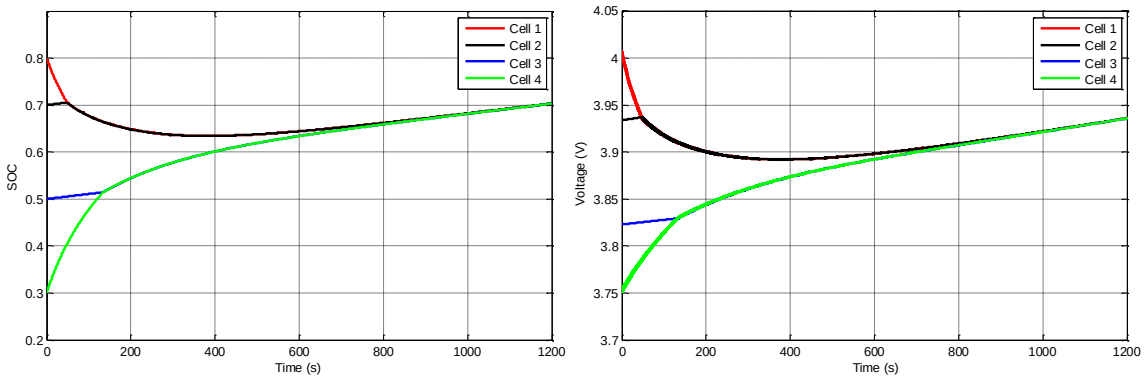

a) SOC for cells. b) Voltages for cells.

Fig. 6.22. Equalization results for single switched capacitor circuit (charging).

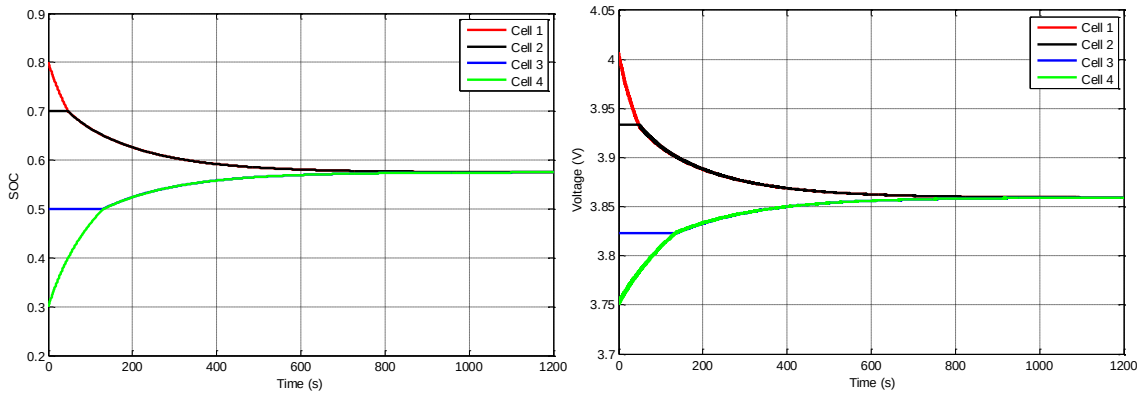

a) SOC for cells. b) Voltages for cells.

Fig. 6.23. Equalization results for single switched capacitor circuit (resting).

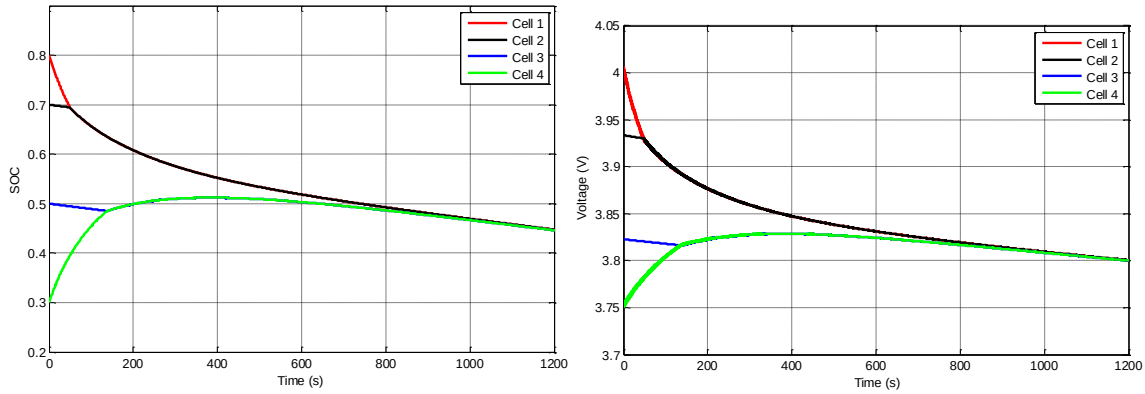

a) SOC for cells. b) Voltages for cells.

Fig. 6.24. Equalization results for single switched capacitor circuit (discharging).

6.3.2 Cell Equalization by Modules with Double Switched Capacitors Combining SOC and SOH Estimation

To improve the equalization speed, multiple cell-to-cell paths are established by adding another equalization capacitor to the circuit described in Fig. 6.21. A proposed double switched capacitor equalization schematic is shown in Fig. 6.25. The two cells with higher SOC are equalized with the two cells with lower SOC at the same step. Therefore, the equalization speed will be improved. The SOC of the cells are also taken as the reference for switch control.

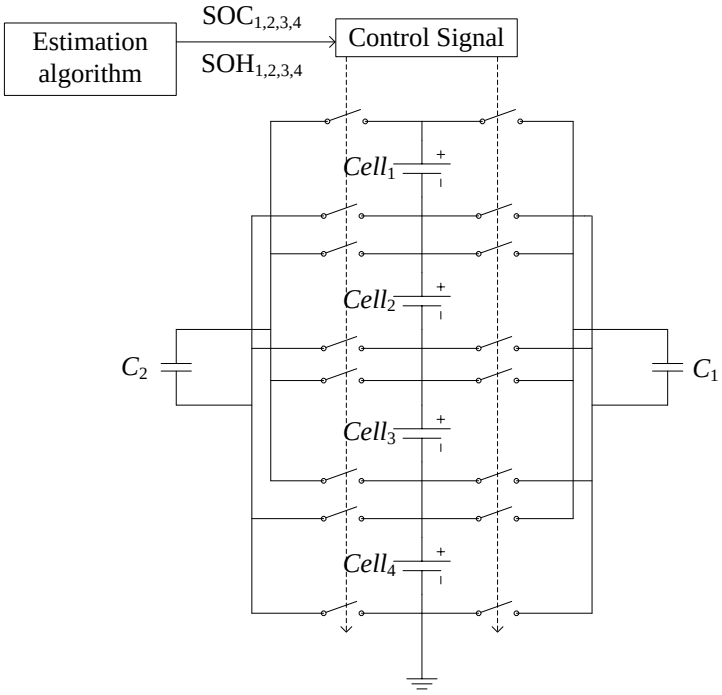

Fig. 6.25. Equalization circuit for double switched capacitor.

The proposed double switched capacitor topology is tested via simulation. All the circuit parameters are set the same as in Section 6.2.2. The initial SOC of the four cells are also set as 0.8, 0.7, 0.5, and 0.3, respectively. The equalization results including the cell SOC and voltages for different battery operations are shown in Figs. 6.26-6.28.

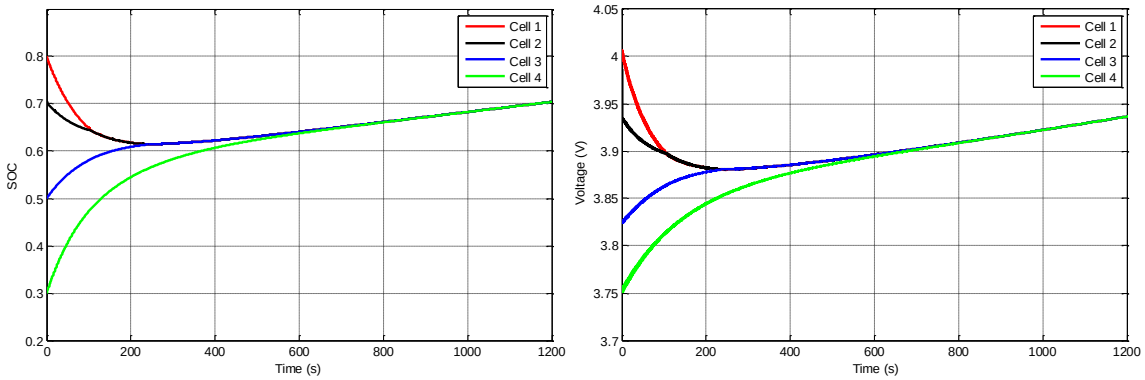

a) SOC for cells. b) Voltages for cells.

Fig. 6.26. Equalization results for double switched capacitor circuit (charging).

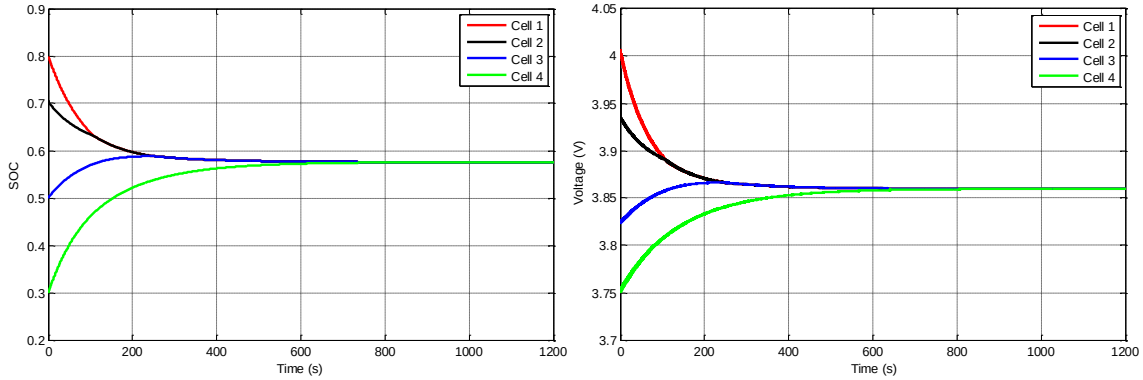

a) SOC for cells. b) Voltages for cells.

Fig. 6.27. Equalization results for double switched capacitor circuit (resting).

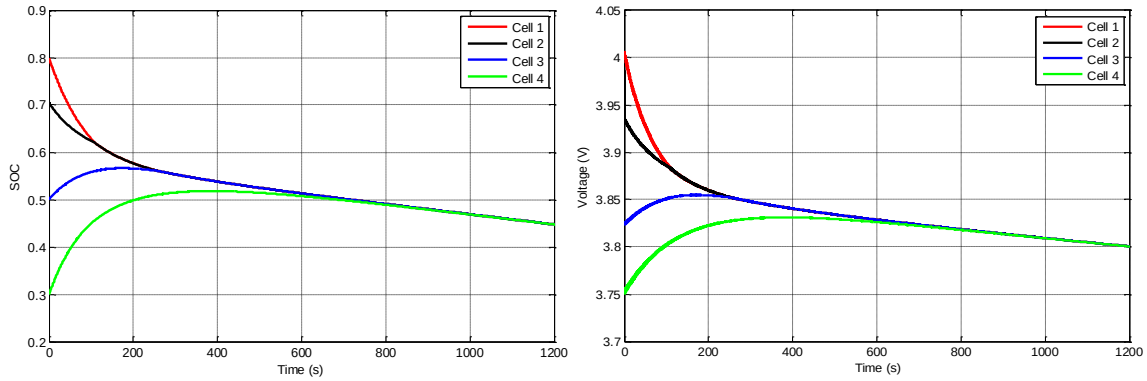

a) SOC for cells. b) Voltages for cells.

Fig. 6.28. Equalization results for double switched capacitor circuit (discharging).

Comparing the equalization results from a single switched capacitor and double switched capacitors proposed in this section, it is shown that the equalization speed is faster for the proposed method. Both SOC and voltage differences between the higher-SOC cells and lower-SOC cells are smaller for the double switched capacitors than a single capacitor after the same equalization time. In addition, it is obvious that all the four cells' imbalance is alleviated at the same equalization step for the proposed method. Three cells achieve equalization in about 200 s, which indicates that the proposed topology alleviates cells imbalance with a better efficiency. To summarize, the proposed equalization method using double switched capacitors has a faster speed and better equalization effect than single switched capacitor topology.

Based on the proposed equalization structure, the module concept is also considered. Taking four cells as one module, the equalization capacitor for adjacent modules is also applied. The UDDS cycle is used to test the modularized equalization schematic using double switched capacitors. The initial SOC for the cells are given in Table 6.3. The equalization results from simulation are shown in Fig. 6.29. All the cells' voltages and SOC settle to the same value quickly using the proposed equalization method.

Table 6.3. Initial cell SOC in the proposed topology.

Cell No.	1	2	3	4	5	6	7	8
SOC	0.8	0.3	0.7	0.5	1	0.5	0.9	0.7

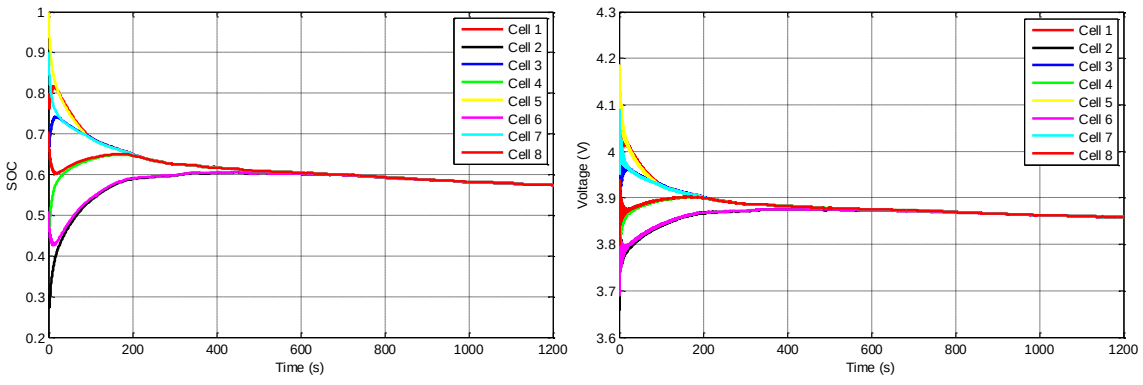

a) SOC for cells.

b) Voltage for cells.

Fig. 6.29. Equalization results for double switched capacitor circuit in modules (UDDS cycle).

The equalization schemes studied in this section rely on the estimated battery SOC, whereas errors may occur from the estimation results. The double switched capacitors method can reduce the inaccurate SOC estimation's effect to some extent. In Chapter 5, it has been verified that the SOC error provided by the estimation algorithms is smaller than 2%~3% in most cases. Hence, when the actual SOC difference among cells is larger than 5%, the SOC estimation error may not affect the equalization results. When the actual SOC difference is smaller, the equalization process does not stop, even the selection of cell pairs is not the most suitable. The charge is still transferred through pairs of cells in the string. The only defect is that the cell-to-cell equalization efficiency is decreased by the inaccurate SOC estimation. If the real SOC difference is small and the estimated SOC has large errors, the equalization speed will be similar to the conventional adjacent switched capacitor circuit. However, for this case with light cell imbalance phenomenon, a low equalization speed is not so effective because light imbalance leads to light damage to battery string.

Sometimes, the voltage of higher SOC cell may be lower than that of the lower SOC cell caused by battery aging or manufacture process. As instructed in Chapter 5, the battery internal resistance increases with battery aging. A larger resistance results in larger charging or discharging voltage that affects the cell terminal voltage. The phenomenon of the battery with a large resistance getting a lower voltage but with a larger SOC is possible. To prevent the possibility of charge transferred from a lower SOC cell to a higher SOC cell through the equalization capacitors, the equalization circuit will be suspended if such condition is tested. If a SOC difference larger than 5% occurs with sensed higher terminal voltage for lower SOC cell, the corresponding path's switches will be off and no equalization process is taken. Here, cell voltage measurements are also considered. Hence, the phenomenon of SOC cell charging higher SOC cell will be avoided. The battery inner resistance is estimated as an indication for SOH in Chapter 5. Thus, cell SOH estimation is taken as an auxiliary reference to determine the suspension steps during the equalization process. SOH will also be a compensation for inaccurate measured voltage. When SOC difference is larger than 5% and the larger SOC cell also achieves larger SOH, the equalization process is also suspended. If the estimated SOH is larger than some preset value, the corresponding cell will be excluded in the equalization

process to avoid transferring charge to other cells. Thus, the proposed strategy is intelligent with a simple structure and a direct control method. SOC and SOH estimation is combined to improve the reliability of the equalization process.

More capacitors and switches are needed in the equalization circuit for double switched capacitors compared with a single capacitor. The cost and equalization speed need a trade-off when implementing the circuit. Comparing with the methods in Section 6.2, less capacitors and switches are needed for single or double capacitor methods, but the battery estimation results are needed as the reference.

6.4 Summary

In this chapter, cell equalization using a switched capacitor schematic with the simple topology and control method is studied and improved. A chain structure capacitor circuit using module concept equalization topology is proposed. Simulation results perform at a fast equalization speed. Then, a modularized double switched capacitor equalization method based on the single switched capacitor method is proposed. This method takes SOC and SOH of Li-ion batteries as control signals. With the proposed topology, the equalization speed is fast and the battery energy condition is considered, improving the system efficiency and reliability.

After solving the cell imbalance problem inside Li-ion battery pack, the batteries in the EV will be taken as a whole energy source. In the next chapter, the Li-ion battery pack's operation and power contribution will be determined and supervised by a proposed power management strategy. This topic will be relevant to EV's performance directly.

Chapter 7 Fuzzy Logic Power Management Strategy for EVs Considering Li-ion Battery Aging

In this chapter, Li-ion battery pack in electric vehicles (EVs) will be taken as a whole to design the power management strategy in energy management system (EMS). Besides, the device of ultracapacitor is also considered. The organization of Chapter 7 is described as follows. Section 7.1 states the significance of combining ultracapacitors with Li-ion batteries as EV power sources and the objectives for designing a power management strategy in EMS. The schematic for power management strategy is also given. In Section 7.2, the required power in EVs is modeled. Section 7.3 gives the model of the ultracapacitor and compensates the aging effect to the Li-ion battery model. The parameters for the Li-ion battery pack and ultracapacitor pack are also introduced in this section. In Section 7.4, a power management strategy considering Li-ion battery aging level based on fuzzy control is designed. The fuzzy logic controllers' structure, membership functions and fuzzy rules are designed according to different EV driving actions. In Section 7.5, the power management results are presented to verify the performance of the designed strategy and the discussion on these results is given. Section 7.6 concludes this chapter.

7.1 Introduction

In EVs, the battery pack composed of Li-ion batteries supplies energy for the whole system. Except the Li-ion battery pack, some other sources, such as fuel cells and ultracapacitors [112, 113, 138], can be added as the energy supply sources. In the EV's energy system, the function of energy management is specified in the power management strategy design for all the sources in EVs. The power management strategy determines the contributed power for each source and supervises the power source's operation status. With a well-designed control strategy, EV's required power for specific driving actions will be supplied and each power source will operate at its optimal operation point simultaneously.

In this thesis, the schematic for the power management strategy in EMS is designed in Fig. 7.1. Two power sources including Li-ion battery packs and ultracapacitors are used as the

system power sources. As the major power source in EVs, the Li-ion battery pack has high energy density that meets the EV's need. In EVs, it is usual for the power source to provide large, abrupt power with great fluctuation when the EV is starting or accelerating. However, Li-ion batteries should avoid fast peak current and current variation in high frequency. Li-ion batteries encounter lifetime reduction or even permanent damage when large current or current with drastic fluctuation applies. To avoid accelerated degradation or damage to the battery pack, the power source composed of ultracapacitors is considered in the EV's energy system.

Ultracapacitors have been commonly-used in EVs for their high power density and fast dynamic response [113]. Ultracapacitors do not have memory effect and perform much longer lifetime. Compared with batteries, ultracapacitors endure much more charging and discharging cycles and tolerate much harsher current, including large current and current with great fluctuation in high frequency. In batteries, the energy conversion from chemical to electrical energy is realized in a slow electrochemical process [112]. Ultracapacitors have much faster dynamics than batteries and improve the time response of the energy system significantly. Thus, ultracapacitors can provide timely large power when a load increase happens suddenly. On the other hand, the power sources in EVs should be able to absorb the regenerative power. The charging current of Li-ion batteries has low limited range. This feature will bring strict limitation for the energy system's energy harvest function when the EV is decelerating or braking, reducing the energy efficiency of EVs. Ultracapacitors with much higher enduring current can absorb large charging current when regenerative braking happens, improving the energy efficiency. With ultracapacitors as the power source in EVs, the energy system will be able to expand the battery pack's lifetime by reducing the battery's current fluctuation as well as charging and discharging cycles during operation. The system will also achieve regenerative energy store and utilization through the ultracapacitor by designing corresponding power management strategy.

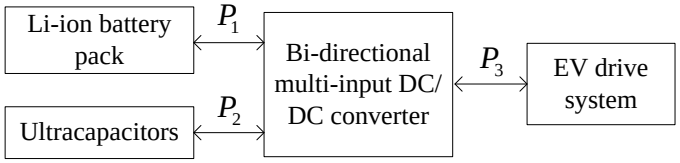

Fig. 7.1. The schematic for power management strategy in EMS.

In Fig. 7.1, the supplied power of Li-ion battery pack is P_1 and the power of ultracapacitors is P_2. The EV drive system consumes the power of P_3. A bi-directional multi-input DC/DC converter can be used in EVs to control the power flow in the energy system.

7.2 EV Power Requirement Modeling

Considering the major factors affecting EV's driving conditions, including road condition, aerodynamic drag, hill climbing and acceleration [139], the vehicle dynamic model is given as [140]:

$$F = sign(v)\mu_{rr} mg\cos\theta + 0.5\rho AC_d v^2 + mg\sin\theta + m\frac{dv}{dt} \tag{7.1}$$

where

F — total tractive force;

$sign(v)\mu_{rr} mg\cos\theta$ — rolling resistance force;

$0.5\rho AC_d v^2$ — aerodynamic drag force;

$mg\sin\theta$ — hill climbing force;

$m\frac{dv}{dt}$ — acceleration force.

All the symbols in (7.1) and their values taken in this chapter are shown in Table 7.1. All the values are provided by the software of Advisor. The hill climbing angle θ is assumed to be 0. The driving velocity v of the vehicle is obtained from the EV's driving conditions. Thus, the EV's required power for a particular driving cycle can be computed using (7.1).

The EV's driving cycle is an established model as a stochastic process predicting the distribution of future power demands using a discrete-time Markov chain [141, 142]. It is a speed-time sequence representing specific driving behaviors including cruise, acceleration and deceleration [143]. In this chapter, the urban dynamometer driving schedule (UDDS) cycle is applied to test the designed power management strategy. Thus, the UDDS cycle data is used to compute the EV's required power during driving. The speed file for the UDDS cycle is also extracted from Advisor as Fig. 7.2 shows.

Table 7.1. The parameters for EV dynamic model.

m (Vehicle mass)	1000 kg
A (Frontal surface)	1 m^2
ρ (Air density)	1.2 kg/m^3
C_d (Drag coefficient)	0.4
μ_{rr} (Rolling coefficient)	0.015
g (Gravity acceleration)	9.81 m/s^2

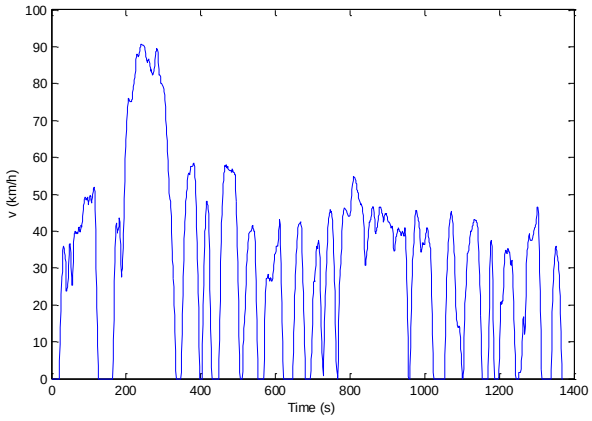

Fig. 7.2. EV speed-time data for the UDDS cycle.

Then, the EV required power is computed by multiplying the tractive force and the vehicle speed:

$$P_3 = F \cdot v \tag{7.2}$$

The required power during the UDDS cycle is shown in Fig. 7.3. The positive power represents the EV consumed power. The negative power represents the regeneration mode. The maximum consumed power is $P_{3\max} = 36.45\,kW$ and the maximum regenerative power is $P_{3\min} = 11.09\,kW$. The average required power during the whole cycle is $P_{3avg} = 5.064\,kW$.

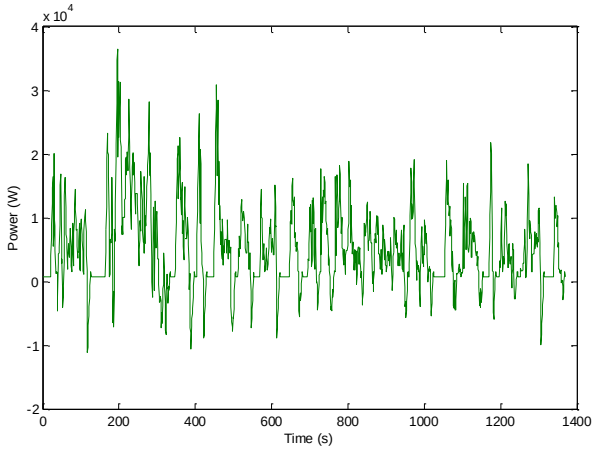

Fig. 7.3. EV required power for the UDDS cycle.

7.3 Models of Power Sources

Before designing the power management strategy, the models for the two power sources are presented in this section. Both models are represented by the equivalent circuit describing the characteristics.

7.3.1 Model of Ultracapacitors

The equivalent circuit model for ultracapacitors is shown in Fig. 7.4. It is a simple circuit composed of a large capacity capacitor *C* with a series-connected resistor *R*. V_o represents the voltage across the capacitor. V_c represents the terminal voltage. *i* is the discharging current. An ultracapacitor has smaller internal resistance than the Li-ion battery. Unlike the Li-ion battery's nonlinear voltage response to current, an ultracapacitor has approximately linear charging and discharging characteristics.

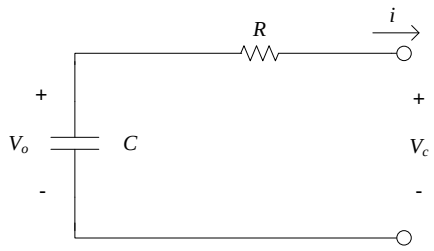

Fig. 7.4. Equivalent circuit model for ultracapacitors [112].

The equation describing the ultracapacitor's terminal voltage based on the equivalent circuit model is derived as:

$$V_c = V_o - \frac{1}{C}\int_0^t i(t)dt - i \cdot R \tag{7.3}$$

Similar to the battery, an ultracapacitor also takes SOC as the indication of remaining charge. Its SOC is defined as the ratio between the remaining charge Q_{remain} and the fully charge Q_{full}:

$$SOC = \frac{Q_{remain}}{Q_{full}} \tag{7.4}$$

Then, (7.4) is transformed with R eliminated as [114]:

$$SOC = \frac{V_c - V_{\min}}{V_{full} - V_{\min}} \tag{7.5}$$

where V_{full} is the ultracapacitor voltage with full charge and $V_{\min}$ is the voltage with the preset deepest discharge. In most conditions, $V_{\min}$ is set in a limited range. $V_{\min}$ is defined as $\frac{1}{3}V_{full}$ here. Thus, the ultracapacitor state of charge (SOC) can be obtained from (7.5) with its terminal voltage.

To provide enough power during EV operation, individual ultracapacitors are also connected in series and parallel to make up a pack.

7.3.2 Li-ion Battery Model Considering Battery Aging

In most studies on power management strategy, the simple Li-ion battery circuit model composed of a series-connected bulk capacitor and an inner resistance is used in the

system to simulate the battery pack. It has been stated in Chapter 2 that the simple model could not describe the battery behavior accurately, especially in the EV's drastic working conditions. In this chapter, the established battery equivalent circuit model with two RC networks is applied. To protect the battery pack by avoiding over-charging and over-discharging in the EV's working environment, Li-ion battery SOC is restricted in the range [0.2, 0.9], whereas in practice this range may be restricted in [0.3, 0.9]. Thus, the battery model in Chapter 5 with constant circuit parameters is reasonable to be used here for its simplicity and accuracy in the range of $SOC \in [0.2,1]$.

An important objective to design the power management strategy in EMS is to protect Li-ion battery pack and extend its life. Then, the mechanism of the Li-ion battery aging must be modeled here to design and test the proposed strategy. The battery pack in EVs works in long term with hundreds of cycles. Li-ion battery degradation phenomenon including capacity fade and delivering power reduction occurs during cyclic operation [74]. To compensate the lack of battery aging data from experimental test, the battery aging level is evaluated and modeled using the method proposed in [75-78] based on the concept of Ah-throughput. Hence, Li-ion battery aging is also modeled and added to the equivalent circuit model.

The concept of Ah-throughput is first introduced in [144]. It is defined as the accumulated current amount during cycling that describes the battery degradation level [69]. It is defined that the battery has a constant total Ah-throughput magnitude for various operation conditions. In [75], the total Ah-throughput A is computed by a nominal discharging cycle with 1C current to the deepest discharge grade under room temperature until end-of-life (EOL) is reached. It is computed as:

$$A = \int_0^{t(EOL)} 1\mathrm{C}dt \tag{7.6}$$

It is defined that when the battery capacity decreases to its 0.8 nominal capacity C_n, EOL is reached. Thus,

$$C_{EOL} = 0.8C_n \tag{7.7}$$

According to the assumption in [75], the battery aging degradation could be calculated by the ratio between the total Ah-throughput and the battery consumed Ah-throughput. The consumed Ah-throughput is not a simple integral of the battery current. It is the effective Ah-throughput converted from the accumulated current with an aging factor named severity factor [78]. Thus, EOL is reached when the effective Ah-throughput reaches *A* [75]. The affecting factors that accelerate battery aging are considered to determine the severity factor represented by μ here.

It has been known that the depth of discharge (DOD, indicating by the alternate representation of SOC here) of Li-ion batteries, temperature, calendar and current rate are the effective factors on battery aging [69, 71, 73, 145]. Here, the temperature effect is not considered as the EV is assumed to work in normal ambient temperature and with ideal thermal management system as stated in the previous chapters. The calendar-life effect during storage is also not considered since the focal point is the power management strategy during EV traction applications, not stationary applications. On the other hand, reference [69] investigates that DOD has very little effect on the battery capacity fade and excludes DOD from the battery aging model. In EVs, the battery pack has preset SOC range during all cycles. Therefore, DOD's effect on battery aging trends to be uniform with different cycle conditions, and this effect could be eliminated. Thus, only the current rate effect on the Ah-throughput is considered in this section.

In [75], a severity factor map is proposed and depicted. In this section, a map considering the relationship between the current rate and μ is shown in Fig. 7.5. In [76, 145], it has been investigated that a larger current accelerates battery aging. The greater influence on effective Ah-throughput is represented by a larger μ. It is deduced that with the higher current rate, a larger μ should be obtained. So μ increases monotonously according to the current rate. In Fig. 7.5, the relationship is approximated by a linear function. The slope is supposed to be a large value to make the battery aging phenomenon more obvious within fewer cycles. The largest current rate is set as 2C, which is the largest discharging current for the Li-ion battery model used.

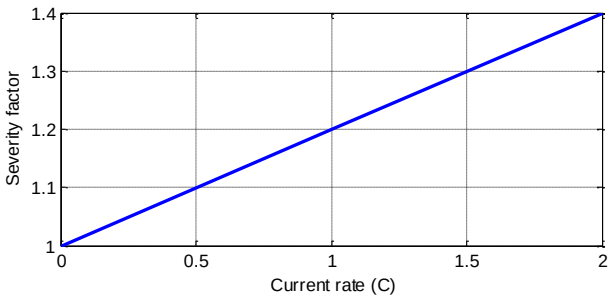

Fig. 7.5. Severity factor map.

When the battery current pattern is composed of different discharging currents, the applied current is converted to the current multiplied by μ, representing the same battery aging level achieved by nominal current accumulation. Thus, the battery effective Ah-throughput $A(\mu,t)$ is obtained by:

$$A(\mu,t) = \int_0^{t(EOL)} (\mu(i)\cdot i(t))dt \tag{7.8}$$

After determining $A(\mu,t)$, the battery aging level could be expressed by $A(\mu,t)/A$. Next, the state of health (SOH) can be calculated by the Ah-throughput fade scale directly. The SOH equation is derived from the battery aging model as in [76]:

$$\dot{SOH} = -\frac{\mu(i)\cdot i(t)}{A} \tag{7.9}$$

$$SOH(t) = SOH(0) - \frac{A(\mu,t)}{A} \tag{7.10}$$

It is assumed that a fresh Li-ion battery will experience a fixed number of discharging cycles with the nominal current before EOL. Thus,

$$A \approx C_n \cdot N_n \tag{7.11}$$

where N_n represents the nominal total cycle number under nominal current cycles. Considering the battery capacity fade from fresh to EOL, SOH_{min} is set to 0.1.

It has been stated in Chapter 5 that Li-ion battery aging has an impact on its model parameters. The degradation causes increases in both capacity fade and internal resistance [71, 74, 146]. To describe the battery degradation phenomenon in the battery model, the

expressions for the aging affected parameters including the changing capacity C_b and series resistance R_s, should be added in the circuit model. It has been proposed that C_b and R_s's variation to aging could be approximated as linear functions of the cycle number N. The capacity fade is expressed in terms of a specific percentage capacity loss per cycle [72]. R_s is also investigated that it increases linearly with the cycle number [55].

A concept of equivalent cycle number is used here to describe the battery model parameter variations as functions of the battery aging level. Unlike adding up the number of consumed cycles of the battery, a cycle number converted from $A(\mu,t)$ named equivalent cycle number is proposed here. The equivalent circuit number $N(\mu,t)$ represents the number of normal current cycles with the same degradation level for the consumed cycles. Thus, $N(\mu,t)$ is calculated as:

$$N(\mu,t)=\frac{\int_0^{t(EOL)}(\mu(I)\cdot I(t))dt}{C_n} \tag{7.12}$$

Then, the functions describing C_b's and R_s's variations to the battery aging level are determined by:

$$C_b(t)=C_n+k_1\cdot N(\mu,t) \tag{7.13}$$

$$R_s(t)=R_{BOL}+k_2\cdot N(\mu,t) \tag{7.14}$$

where k_1 and k_2 are the coefficients both with very small absolute value. It is assumed in this section that after 500 nominal cycles EOL is reached. Then C_{EOL} = 0.8C_n and R_{EOL} = 2R_s(0). Hence, k_1 and k_2 can be computed. Fig. 7.6 shows the relationships between the equivalent cycle number and C_b, R_s.

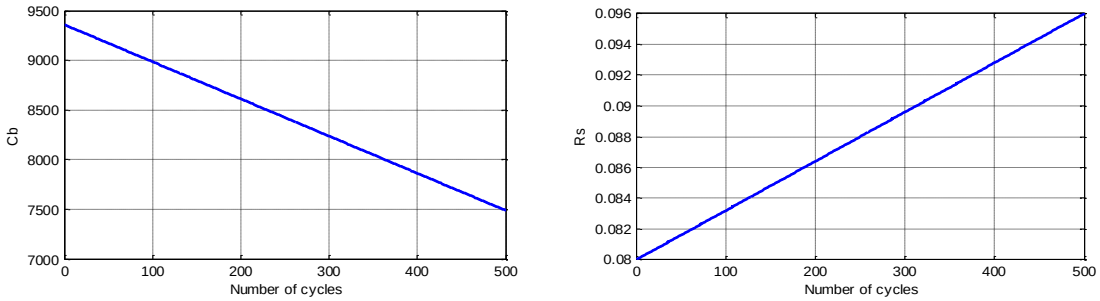

a) C_b b) R_s

Fig. 7.6. C_b and R_s variations to cycle number.

Thus, a Li-ion battery model including battery aging mechanism is established. The battery SOC can be obtained online by the algorithms introduced in the previous chapters, which is not repeated here.

7.3.3 Parameters for the Power Sources

It has been described that individual Li-ion battery cells make up battery pack as the power source in EVs. Similarly, the ultracapacitor cells also make up the ultracapacitor pack to supply or absorb power to EVs. Based on efficient cell and module equalization schematics proposed in Chapter 6, the EV's Li-ion battery pack parameters are redesigned to meet the power requirement of practical driving cycles. It is assumed that cell equalization is also realized in the ultracapacitor pack. The parameters of the battery pack and ultracapcitor pack including model parameters for the Li-ion battery and ultracapacitor packs are shown in Table 7.2. The parameters for the ultracapacitor model are from manufacturer's datasheet by referring to their websites.

Table 7.2. Parameters for the power sources.

a) Li-ion battery pack.

Number of cells in series	60
Number of branches in parallel	50
Nominal capacity	2.6 Ah
Nominal voltage	3.7 V
Series resistance	0.08 Ω

b) Ultracapacitor pack.

Number of cells in series	110
Number of branches in parallel	5
Capacity	500 F
Nominal voltage	2.7 V
Series resistance	0.01 Ω

7.4 Fuzzy Logic Power Management Strategy Considering Battery SOH

The elementary function of power management strategy in EMS should be to supply the required power and absorb the regenerative power during EV driving. A series of equations describing this function are derived using the expressions in Fig. 7.1.

$$P_3 = P_1 + P_2 \tag{7.15}$$

$$P_1 = K_1 P_3 \tag{7.16}$$

$$P_2 = K_2 P_3 \tag{7.17}$$

where K_1, K_2 are the coefficients representing the proportion of the two sources' contributed power and K_1+K_2 is 1.

The proposed control strategy should distribute the EV power requirement and supervise the power source's operations. Based on above functions, the designed power management strategy should also focus on Li-ion battery protection and life extension. In the last section, Li-ion battery pack aging mechanism has been modeled and expressed by SOH. Thus, a fuzzy logic controller scheme considering SOH of Li-ion batteries is designed to manage the power distribution of the battery pack and ultracapacitor pack, supervise their situations and extend Li-ion battery's service life.

7.4.1 Fuzzy Logic Controller Scheme

Combined by Li-ion battery pack and ultracapacitors, the energy system has nonlinear characteristics with several variables. A controller is needed to perform the functions of power distribution and exchange as well as maintaining the two sources' operation status. However, to obtain a proper mathematical model for the overall system is difficult. The overall system is with uncertainties and imprecise knowledge. As the controller dealing with complex nonlinear systems, a fuzzy logic controller is appropriate to do power management in different systems [112-114, 139, 143]. Fuzzy logic provides an approximated but effective description for the systems with complex behaviors [147]. Based on the fuzzy set theory, a fuzzy controller is formed by fuzzy rules with "IF…, THEN…" structure designed by experts from knowledge and experience. These fuzzy rules are intuitive to design and comprehend and can approximate the control input

according to different preconditions. Fuzzy logic control is suitable for highly nonlinear and complex control system, performing flexibility and robustness for imprecise model and data. Besides, this type of controllers does not require heavy online computation load and it is practical. Fuzzy logic strategy also supervises each power source to operate within high and proper energy regions.

Considering the two power sources' operation status in EVs, two fuzzy logic controllers including the EV power distribution controller and source power exchange controller are designed as follows.

(1) Controller 1: EV power distribution controller

The fuzzy logic controller 1 is designed to perform power distribution for the EV. It has four inputs and one output. The Mamdani type controller is used here. The EV required power P_3 computed from particular driving actions is taken as the controller's input. To supervise the two sources' real-time status and ensure the sources work in good situation, the battery and ultracapacitor's real-time SOC expressed by SOC_{BT} and SOC_{UC}, are also taken as the inputs to the fuzzy controller. Unlike previous studies on the EV power management strategy, the controller designed in this chapter adds Li-ion battery's SOH, SOH_{BT}, as another control input in the control process. Thus, the battery aging phenomenon during EV driving is directly considered. The Li-ion battery lifetime will be prolonged by proposing particular fuzzy rules including the premise of SOH. The controller output is the power distribution coefficient for the Li-ion battery pack, K_1. It should be stated that in this chapter, the focus is on the power management strategy design. Hence, the two power sources' SOC and SOH will be directly obtained from their models in simulation. In practice, Li-ion battery SOC and SOH could be accurately estimated online based on experimental measured variables using the algorithms proposed in Chapter 5. The ultracapacitor SOC could be obtained more easily than the Li-ion battery since its characteristics is nearly linear and its model is much simpler. The fuzzy controller 1's structure is shown in Fig. 7.7.

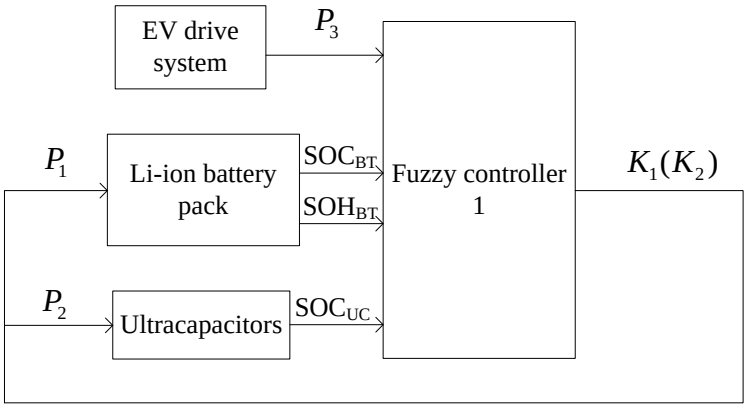

Fig. 7.7. Fuzzy controller 1's structure.

(2) Controller 2: Source power exchange controller

The fuzzy logic controller 2 is designed to determine the power exchange between power sources. Besides the mode that the power sources supply EV required power together, power flow exists between the sources to manage the two sources' operation points. Compared to the Li-ion battery, the ultracapacitor has much lower energy density. When supplying or absorbing high power, the ultracapacitors may get low or high energy in a short time. Thus, when SOC_{UC} becomes high or low, fuzzy controller 2 is applied to control the power exchange between the battery pack and the ultracaptiors. The controller's inputs are designed as EV's power P_3, SOC_{BT} and SOH_{BT}. The output is the power exchange coefficient K_3 which determines the power flow between the battery pack and ultracapacitors. Controller 2 has two patterns including the battery charging the ultracapacitor and the ultracapacitor charging the battery. The controller's structure is shown in Fig. 7.8, where P_T represents the exchange power. To limit P_T in a safe range, it is determined that:

$$P_T = K_3 \cdot P_{3avg} \tag{7.18}$$

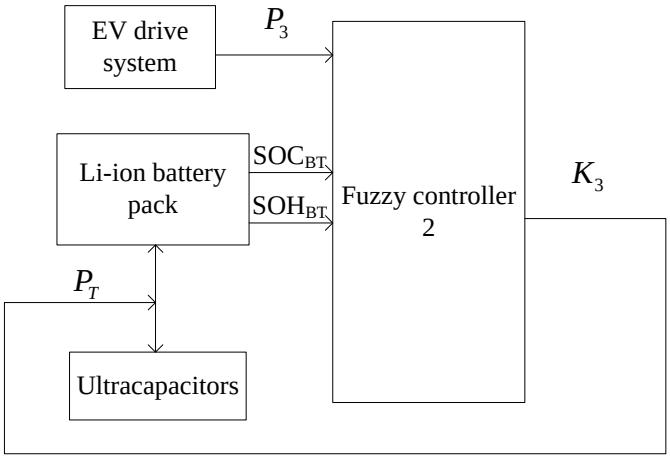

Fig. 7.8. Fuzzy controller 2's structure.

(3) Mode 1 of Controller

To meet the EV's power requirement, it is assured that the fuzzy logic controller 1 works all the time during driving. Mode 1 of the controller represents the situation that only controller 1 works. For this mode, no power exchange exists between the two sources. If the system is in this mode, the battery pack and ultracapacitors will supply power to the EV together.

(4) Mode 2 of Controller

In this section, it is designed that when $SOC_{UC} < 0.3$ during driving, the battery pack begins to charge the ultracapacitors till $SOC_{UC} > 0.7$. If $SOC_{UC} > 0.9$, the ultracapcitors will provide energy to the battery pack. Thus, the fuzzy controller 2 starts or stops working according to SOC_{UC}. When mode 2 is applied, the two fuzzy controllers are working together. The battery pack supplies both the EV's power and the charge or discharge of the ultracapacitors. The battery pack's contributed power $\tilde{P}_1$ will be the sum of the two controllers' outputs as shown in Fig. 7.9.

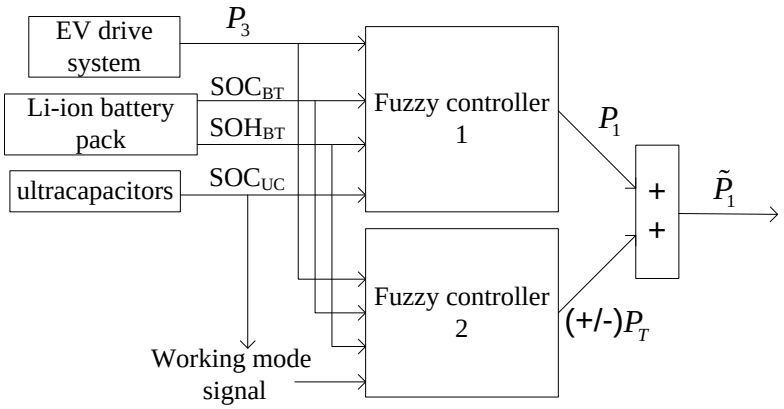

Fig. 7.9. Battery pack's power P_{1a}.

7.4.2 Fuzzy Logic Control Strategy

In this section, the fuzzy control strategy is proposed for different driving actions and the two power sources' operation points. Based on the prior knowledge about the traction and energy supply system in EVs, a well-designed control strategy will guarantee the power management scheme's performance, robustness and reliability for various situations.

(1) EV cruising

When cruising, the EV is in the normal driving condition with a constant velocity. In this condition, the acceleration is zero. Equation (7.1) indicates that the EV power requirement is steady with EV cruising and the required power is low. This low and steady power can be continuously supplied only by the battery pack if the battery is in appropriate SOC and SOH situations. The ultracapcitor pack will be resting during this interval if no charge is needed to it. If SOC_{BT} or SOH_{BT} is rather low, the ultracapacitors will also supply a small steady power to the EV. If SOC_{UC} is low, the battery pack will charge the ultracapacitors with nearly constant power.

(2) EV accelerating or starting

When the accelerating action occurs, the EV required power increases instantaneously. If the accelerated velocity is high, this increase will be both drastic and large. Especially during the moment of EV starting, an abruptly pulsing power is required from the sources. This abrupt high power should not be supplied only by the battery pack because it may do damage to the Li-ion battery. Thus, the control strategy will tend to make the

ultracapacitors supply the violent current variation in a short interval. If SOC_{UC} is high or medium, the ultracapacitors will also partially share the large required power so that the battery pack's power load is alleviated.

(3) EV decelerating or braking

When the EV is decelerating, the regenerative power may exist. When braking happens, the electric motor in the EV will operate as a generator and bring regenerative power. It has been stated that $P_3 < 0$ in this situation. Heavy braking generates significant peak power in a short time for the power sources. The more power absorbed by the power sources, the higher the energy efficiency is. It would be best for the power sources to absorb and store the regenerative power completely. Thus, the regenerative mode must be considered when designing the control strategy. The Li-ion battery's charging current is even smaller than its discharging current. Abrupt high charging current from regeneration will do inevitable damage to the battery pack. Therefore, the ultracapacitor pack is taken as the major power regeneration device except for the condition that SOC_{UC} is very high.

(4) Source power exchange

Although with low energy density, the ultracapacitors take the major responsibility of supplying high fluctuation power and absorbing regenerative power. Thus, the ultracapacitor pack must be charged or discharged by the battery pack to maintain the appropriate operation point. If SOC_{UC} is low, the battery pack will prefer to charge the ultracapcitor pack during EV cruising because the required power from the battery is not very large at this time. If acceleration occurs, the charge to the ultracapacitor pack will be rather small to protect the battery pack from supplying too large a power. When the regeneration mode occurs, the exchange process will be stopped and the ultracapacitors will be charged by the regenerative power only. If SOC_{UC} is high, the ultracapacitor will charge the battery pack. To simplify controller 2 and the corresponding control strategy, it is designed that ultracapacitors charge batteries only when the regeneration mode occurs.

(5) SOC and SOH effect

It has been stated that Li-ion battery's SOC and SOH, and ultracapacitor SOC should be supervised by the proposed power management strategy. Thus, the control strategy needs

to consider these variables and ensures both the battery pack and ultracapacitors work in good performance. When SOC_{BT} is low, the controller tends to decrease the battery pack's supplied power. When SOC_{UC} is low, the controller makes the ultracapacitor pack charged and decreases its supplying power when the severe power requirement variation occurs. If SOH_{BT} is low, the designed strategy will adjust the battery supplying current according to the Li-ion battery aging mechanism to extend the battery pack's service life.

7.4.3 Membership Functions, Rule Base and Defuzzification

The membership functions for fuzzy logic controller 1 are shown in Fig. 7.10 a)-e). All the membership functions are set with triangular and trapezoidal shapes.

The membership function names in Fig. 7.10 are explained as follows:

Negative (N); Positive small (PS); Positive medium (PM); Positive big (PB); Low (L); High (H); Medium (M); Low medium (LM); High medium (HM); Little (LE); Medium low (MEL); Medium high (MEH); and Great (GE).

The meanings of the function names corresponding to EV driving actions are: N: EV decelerating or braking, $P_3 < 0$; PS: Cruising with light power demand; PM: Accelerating; and PB: Starting or accelerating with large power demand. It should be noticed that P_3 has been scaled into the range [-1, 1].

The membership functions for fuzzy logic controller 2 are shown in Fig. 7.11 a)-f) for two different working patterns: battery charging ultracapacitor (BT to UC) and ultracapacitor charging battery (UC to BT). The membership functions are also set with triangular and trapezoidal shapes. Only the positive EV power is considered for the BT to UC pattern. Only the negative EV power is considered for the UC to BT pattern. The names of the membership functions for the EV regenerative power are determined as:

Negative small (NS); Negative medium (NM); and Negative big (NB).

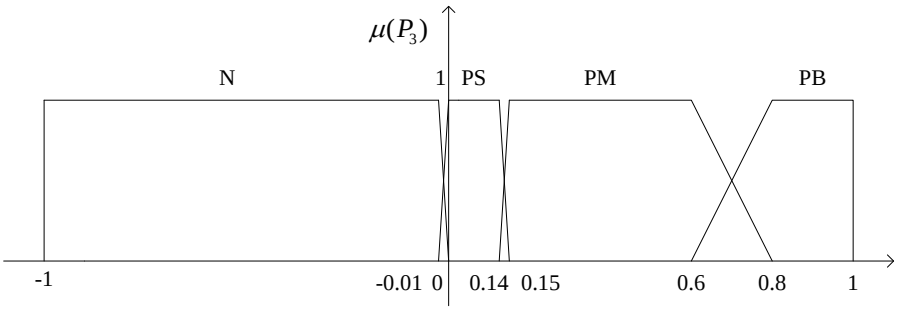

a) EV required power.

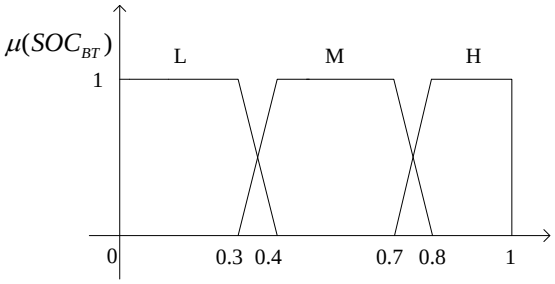

b) Li-ion battery SOC.

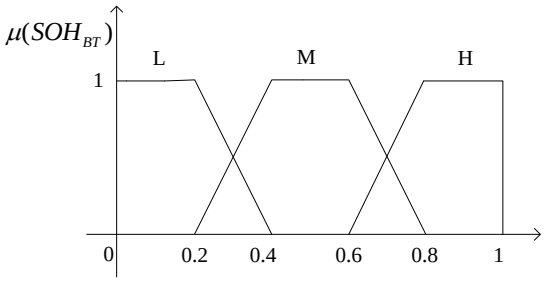

c) Li-ion battery SOH.

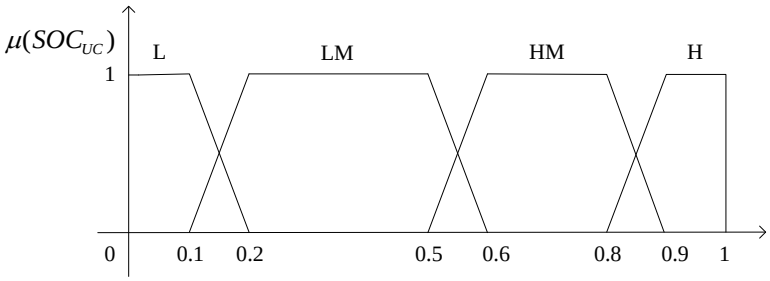

d) Ultracapacitor SOC.

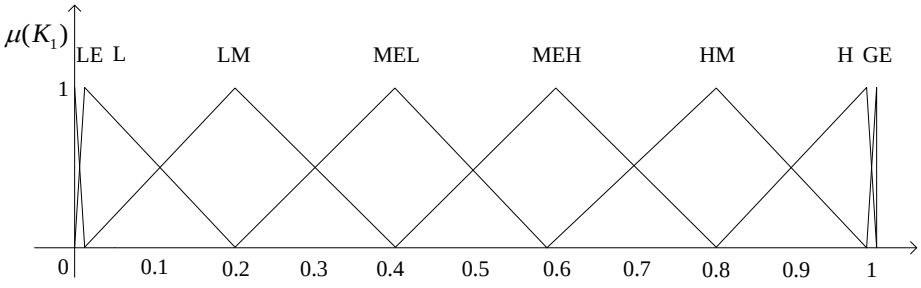

e) Power distribution coefficient K_1.

Fig. 7.10. Membership functions for fuzzy controller 1.

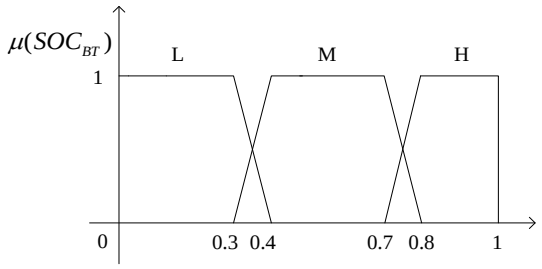

a) Li-ion battery SOC.

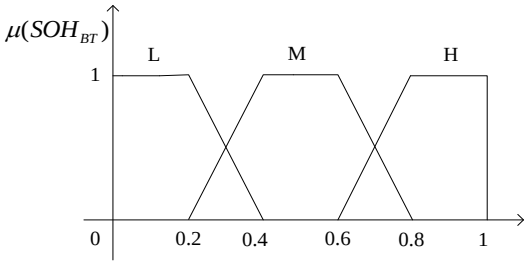

b) Li-ion battery SOH.

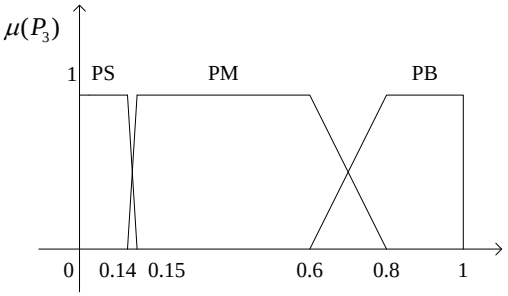

c) EV consumed power (BT to UC).

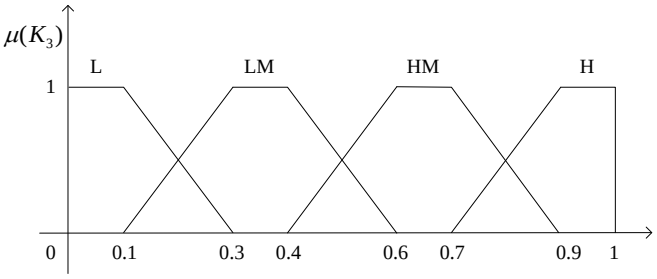

d) Power exchange efficient K_3 (BT to UC).

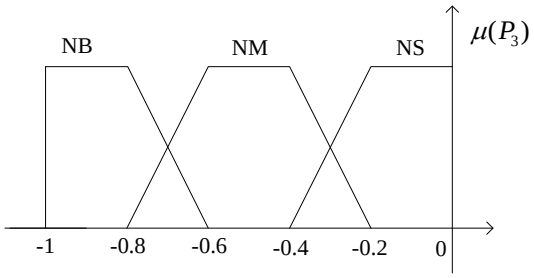

e) EV regenerated power (UC to BT).

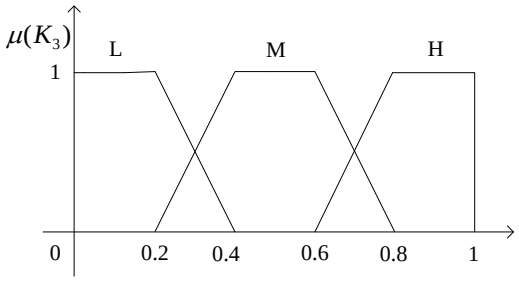

f) Power exchange efficient K_3 (UC to BT).

Fig. 7.11. Membership functions for fuzzy controller 2.

The fuzzy rule base is determined according to the principles for designing the control strategy described in Section 7.4.2. For fuzzy controller 1, the rules have the following structure:

IF P_3 is a, AND SOC_{BT} is b, AND SOH_{BT} is c, AND SOC_{UC} is d, THEN K_1 is e, where a, b, c, d, and e are the membership functions corresponding to each variable as described in Fig. 7.10.

All the 144 fuzzy rules are shown in Table 7.3.

Table 7.3. Fuzzy rule base for fuzzy controller 1.

P_3 = N

	SOH_{BT} = H			SOH_{BT} = M			SOH_{BT} = L		
SOC_{UC} \ SOC_{BT}	H	M	L	H	M	L	H	M	L
L	LE	LE	L	LE	LE	L	LE	LE	LE
LM	LE	LE	L	LE	LE	L	LE	LE	LE
HM	LE	LE	MEH	LE	LE	L	LE	LE	LE
H	LE	MEH	HM	LE	MEH	MEH	LE	MEH	MEH

P_3 = PS

	SOH_{BT} = H			SOH_{BT} = M			SOH_{BT} = L		
SOC_{UC} \ SOC_{BT}	H	M	L	H	M	L	H	M	L
L	GE	GE	GE	GE	GE	GE	GE	GE	GE
LM	GE	GE	GE	GE	GE	GE	GE	GE	H
HM	GE	GE	H	GE	GE	H	GE	H	H
H	GE	GE	H	GE	GE	H	H	H	HM

P_3 = PM

	SOH_{BT} = H			SOH_{BT} = M			SOH_{BT} = L		
SOC_{UC} \ SOC_{BT}	H	M	L	H	M	L	H	M	L
L	HM	HM	HM	HM	HM	HM	HM	HM	HM
LM	HM	HM	HM	HM	HM	HM	HM	MEH	MEH
HM	HM	HM	HM	HM	HM	MEH	MEH	MEH	MEH
H	HM	HM	MEH	MEH	MEH	MEL	MEL	MEL	MEL

P_3 = PB

	SOH_{BT} = H			SOH_{BT} = M			SOH_{BT} = L		
SOC_{BT} / SOC_{UC}	H	M	L	H	M	L	H	M	L
L	MEH	MEH	MEH	MEH	MEH	MEH	MEH	MEH	MEH
LM	MEH	MEH	MEH	MEH	MEH	MEH	MEH	MEH	MEL
HM	MEH	MEH	MEH	MEH	MEH	MEL	MEH	MEL	MEL
H	MEL	MEL	MEL	MEL	MEL	MEL	MEL	MEL	MEL

The fuzzy rules for fuzzy controller 2 have similar structures as:

IF P_3 is a, AND SOC_{BT} is b, AND SOH_{BT} is c, THEN K_3 is e, where a, b, c, and e are the membership functions of each variable as shown in Fig. 7.11.

The fuzzy rule base for controller 2 is shown in Table 7.4.

Table 7.4. Fuzzy rule base for fuzzy controller 2.

a) BT to UC.

	P_3 = PS			P_3 = PM			P_3 = PB		
SOC_{BT} / SOH_{BT}	H	M	L	H	M	L	H	M	L
H	H	H	HM	HM	HM	LM	LM	LM	L
M	HM	HM	LM	LM	LM	L	LM	L	L
L	LM	LM	L	L	L	L	L	L	L

b) UC to BT.

	P_3 = NS			P_3 = NM			P_3 = NB		
SOC_{BT} / SOH_{BT}	H	M	L	H	M	L	H	M	L
H	1	H	H	L	M	H	M	L	L
M	1	H	H	L	M	H	L	L	L
L	1	M	M	L	L	M	L	L	L

The defuzzification method is centroid that is described in [114, 143].

The EV's power is distributed by the fuzzy controllers according to corresponding fuzzy rules. Since P_3 fluctuates drastically, it is possible that the control output sum $\tilde{P}_1$ still contains high frequency variation. To avoid this high frequency component applied on the Li-ion battery, a low pass filter (LPF) is used to exclude fast variation and smooth the battery pack's power [112, 114] as shown in Fig. 7.12. The DSP toolbox in Matlab/Simulink is used to design the LPF in simulation. The battery's power after filtering is expressed by P_{1a}.

Fig. 7.12. LPF smoothing battery power.

Then, the ultracapacitors' actual power is computed as:

$$P_{2a} = P_3 - P_{1a} . \tag{7.19}$$

7.5 Results and Discussion

The power management strategy considering aging of Li-ion batteries based on fuzzy control system is implemented and simulated in Matlab/Simulink. The UDDS cycle is used to test the designed strategy. All the results are described and discussed in this section. First, the initial SOC_{BT}, SOH_{BT}, and SOC_{UC} are set as 0.9, 1, and 1. The power management results are shown in Figs. 7.13-7.19. The EV power, battery pack power and ultracapacitor power represented by P_3, P_{1a}, and P_{2a} are depicted in Figs. 7.13-7.15. It displays the power distribution performance. Fig. 7.14 gives a clear display of the two sources' power. Compared to the ultracapacitors, the battery pack provides much smoother power with less variation as shown in Fig. 7.14 b) and c). It also indicates that the ultracapacitors absorb most of the regenerative power during driving.

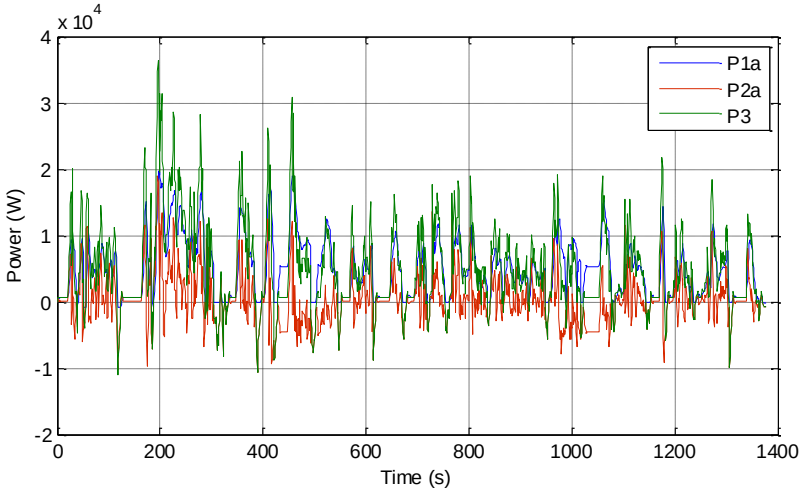

Fig. 7.13. Power distribution results.

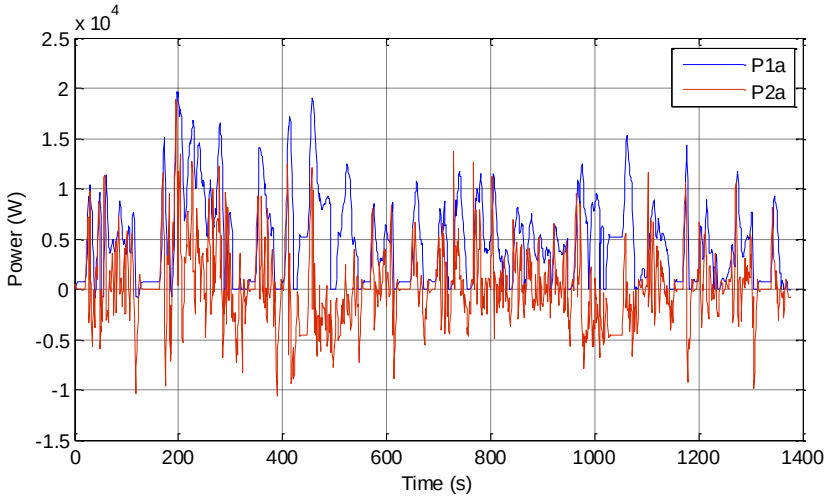

a) Battery pack power and ultracapacitor power during UDDS cycle.

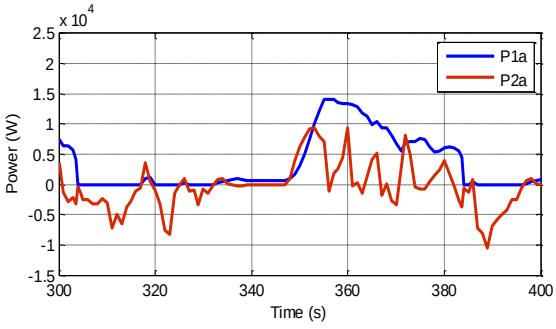

b) Source power comparison 1.

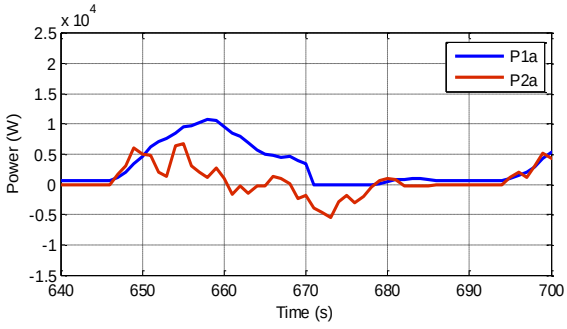

c) Source power comparison 2.

Fig. 7.14. Battery pack power and ultracapacitor power.

To perform the power management results more clearly, some time intervals corresponding to different driving actions are described in Fig. 7.15. The latter part in Fig 7.15 a) and the former part in d) verify that the battery pack supplies most of the required power when the EV is cruising with the designed fuzzy control strategy. At the time when the EV power fluctuates frequently, the battery pack's power is more steady and smoother as b) shows. The power fluctuation is mostly taken by the ultracapcitors in b). Fig. 7.15 a) c) and d) verify that the ultracapacitors provide the abrupt increasing power for acceleration in a short time and the battery pack's power increases much slower to avoid drastic current impulse on Li-ion batteries. Then, the battery pack tends to provide the fundamental power requirement and the ultracapacitors tend to endure the power variation. Fig. 7.15 e) and f) describe the power regeneration mode during EV decelerating and braking. It clearly indicates that the ultracapacitors absorb most regenerative power. The battery pack absorbs steady and small regenerative power or even no power, which is decided by SOC_{BT}, SOH_{BT} and SOC_{UC}. In the time range of e), SOC_{UC} is very high. To avoid overcharging the ultracapacitors, a small part of the regenerative power is allocated to the battery pack. In f), SOC_{UC} is not in the high range anymore. Therefore, the ultracapacitors take all the regenerative power.

The two sources' currents are shown and compared in Fig. 7.16. Both currents are extracted from a single cell. From 7.16 c), it is obvious that the Li-ion battery current is much smaller and with much less variation than the ultracapacitor current. When the EV is starting and cruising as shown in a), the ultracapacitor current increases drastically to provide enough power, whereas the battery current increases slowly and provides steady current. A clear comparison for current variation is described in b).

The variables of SOC_{BT}, SOH_{BT} and SOC_{UC} during the UDDS cycle are shown in Figs. 7.17-7.19. It reveals that SOH_{BT} decreases slowly. SOC_{UC} fluctuates drastically because the ultracapacitor pack endures much larger current and it is charged and discharged for many times. Although changing in a wide range during the driving cycle, SOC_{UC} is restricted within the operation range with good performance. Compared with SOC_{UC}, SOC_{BT} varies more slowly and smoothly. The supervision function of the designed control strategy is verified.

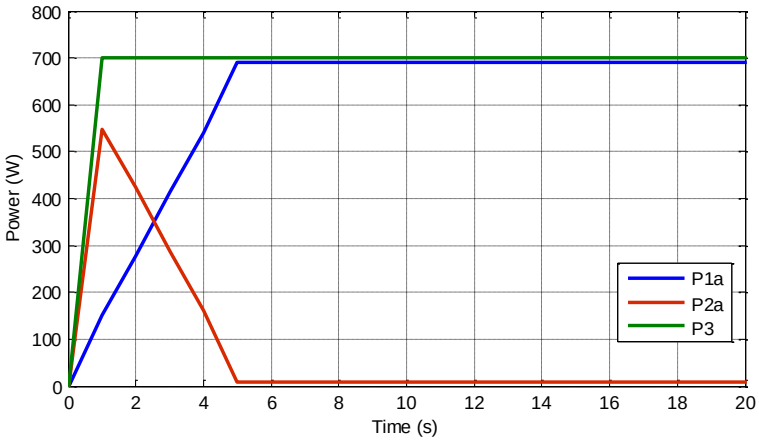

a) Sources power during starting and cruising.

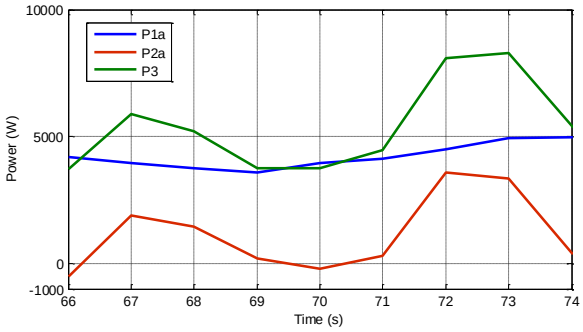

b) Sources power with EV power fluctuation.

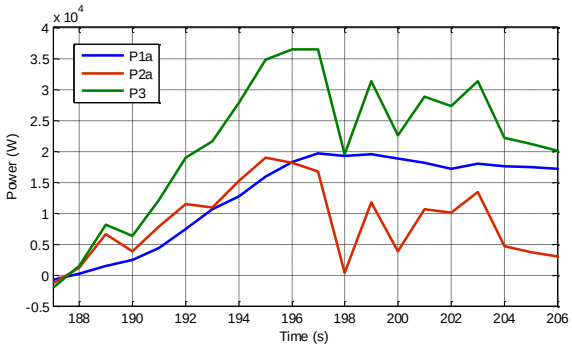

c) Sources power during accelerating.

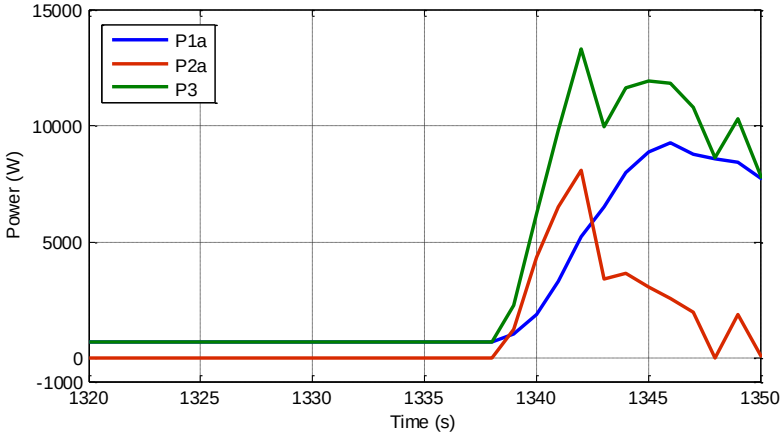

d) Sources power during cruising and accelerating.

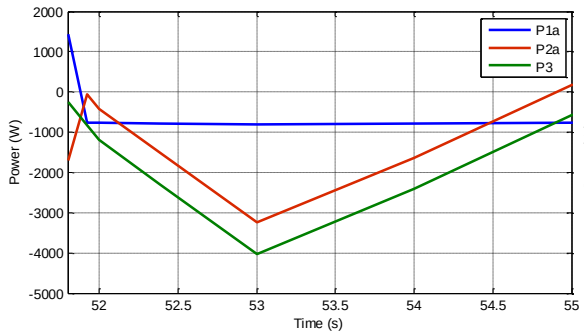

e) Sources power during decelerating.

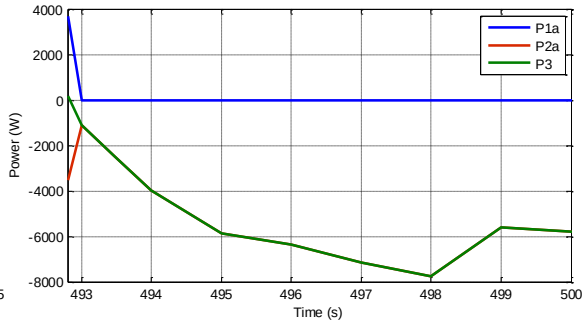

f) Sources power during braking.

Fig. 7.15. Battery power and ultracapacitor power for various EV driving actions.

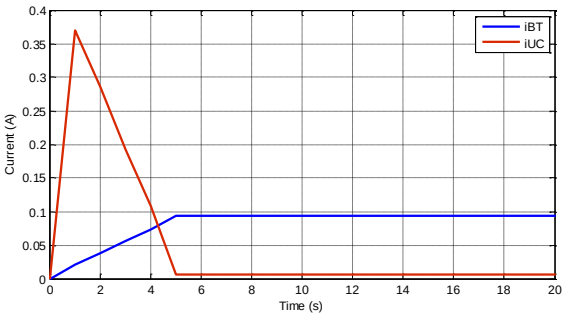

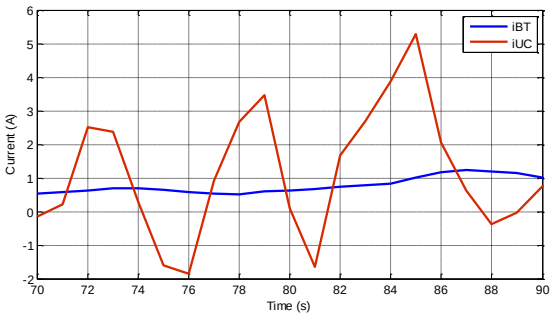

a) Sources currents during starting and cruising. b) Battery current compared with ultracapacitor current.

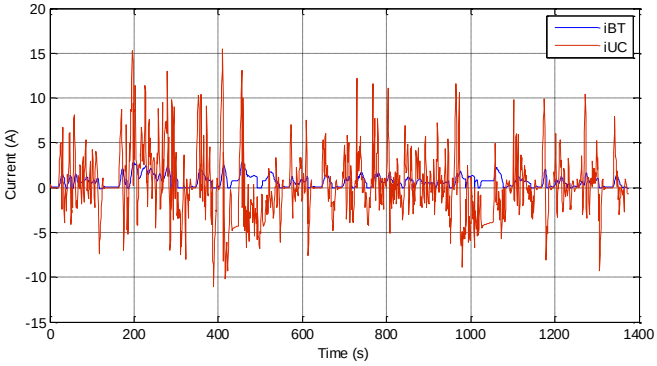

c) Sources current comparison.

Fig. 7.16. Battery and ultracapacitor current comparison.

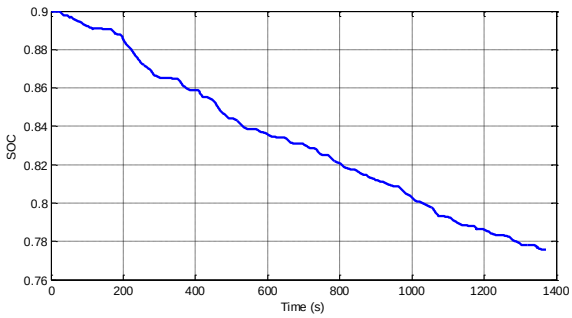

Fig. 7.17. Battery SOC during the UDDS cycle.

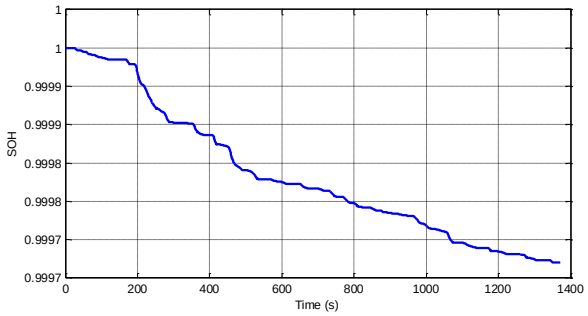

Fig. 7.18. Battery SOH during the UDDS cycle.

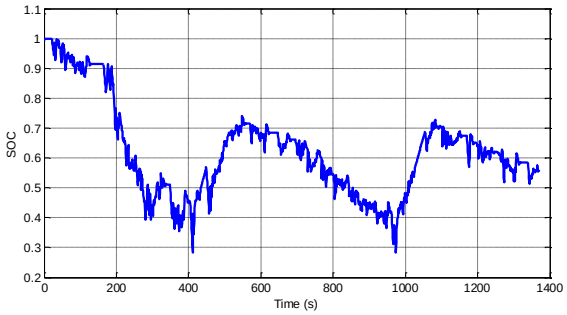

Fig. 7.19. Ultracapacitor SOC during the UDDS cycle.

Then, the initial SOH_{BT}, $SOH_{BT}(0)$, is changed to 0.6 and 0.2, representing the Li-ion battery with different aging levels. The results including power distribution results, SOC_{BT}, SOH_{BT} and SOC_{UC} during the UDDS driving cycle are shown in Figs. 7.20-7.27. Comparing Fig. 7.20 and Fig. 7.24, the EV power distribution has different results for different battery SOH by the proposed power management strategy. With the designed control strategy, the battery pack with a lower SOH would charge ultracapacitors when supplying a steady power. The difference of SOC_{BT} variation during the same driving cycle shown in Figs. 7.21 and 7.25 is also due to the proposed control strategy. Compare the difference between Fig. 7.23 and Fig. 7.27. If SOC_{UC} has been charged to the range that is able to provide good performance on both supplying and absorbing power, the BT to UC process will be postponed by the strategy when SOH_{BT} is lower. This measure avoids the phenomenon that too large battery current accelerates low SOH battery's aging progress when supplying both the EV power and ultracapacitor charge.

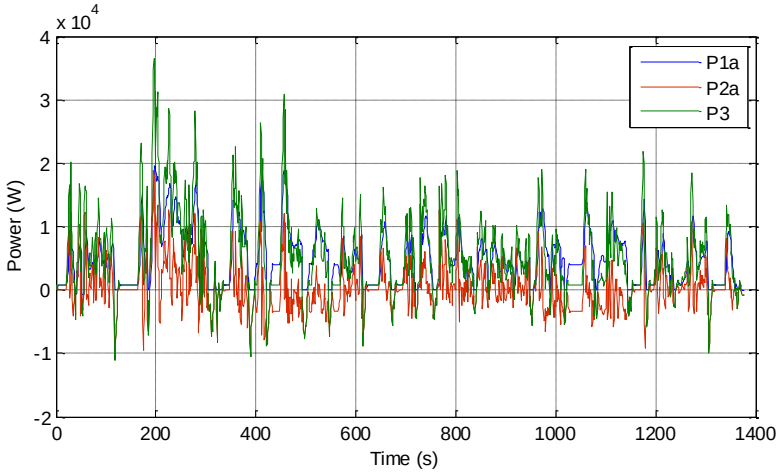

Fig. 7.20. Power distribution results ($SOH_{BT}(0) = 0.6$).

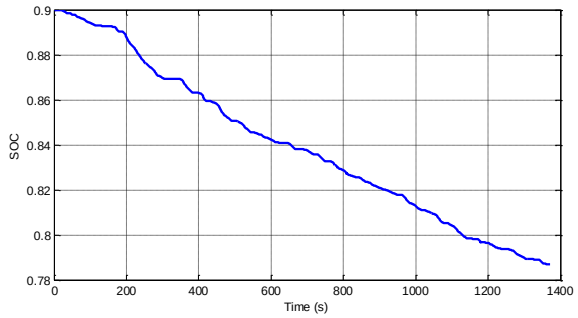

Fig.7.21. SOC_{BT} ($SOH_{BT}(0) = 0.6$).

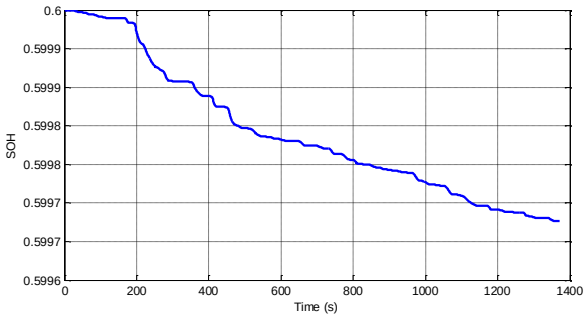

Fig. 7.22. SOH_{BT} ($SOH_{BT}(0) = 0.6$).

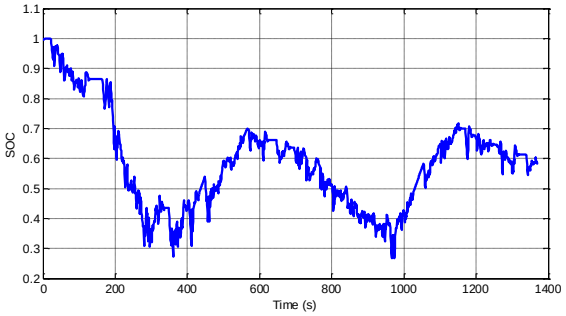

Fig. 7.23. SOC_{UC} ($SOH_{BT}(0) = 0.6$).

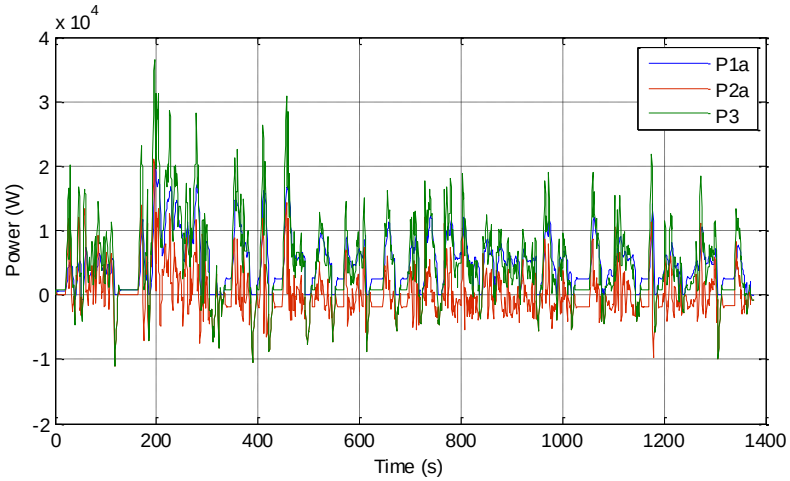

Fig. 7.24. Power distribution results ($SOH_{BT}(0) = 0.2$).

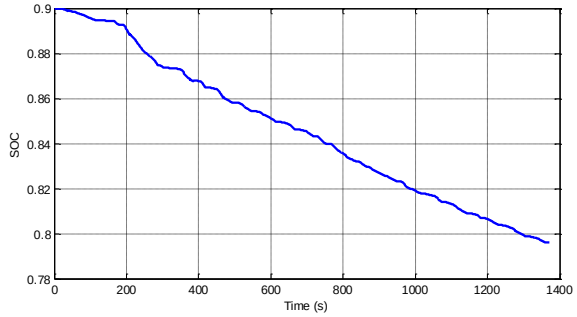

Fig. 7.25. SOC_{BT} ($SOH_{BT}(0) = 0.2$).

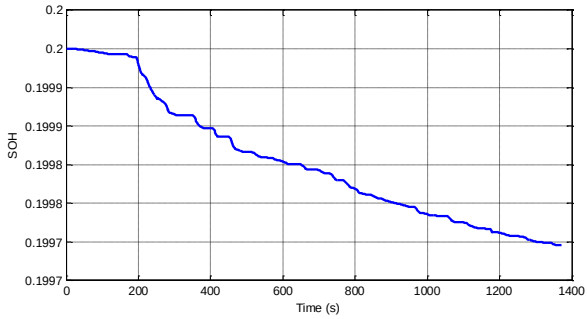

Fig. 7.26. SOH_{BT} ($SOH_{BT}(0) = 0.2$).

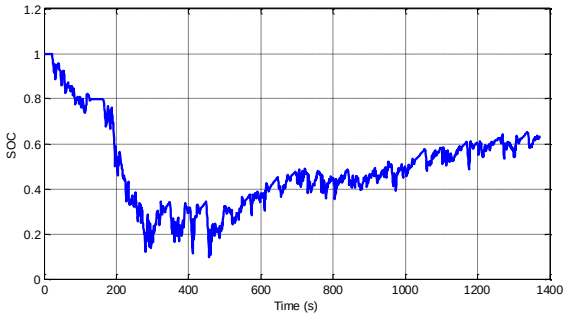

Fig. 7.27. SOC_{UC} ($SOH_{BT}(0) = 0.2$).

The three SOH results after the same driving cycle for different initial SOH_{BT} are compared in Table 7.5. It reveals that the battery SOH decreases less for lower $SOH_{BT}(0)$. When the SOH_{BT} is lower, the fuzzy logic control strategy decelerates the battery aging progress by considering Li-ion battery's aging mechanism in the control process. Thus, the proposed power management strategy intelligently controls the power sources' operation and extends the Li-ion battery service life based on the EV required power and the two power sources' information.

Table 7.5. SOH_{BT} result comparison for different $SOH_{BT}(0)$.

Initial SOH	Resultant final SOH	Δ SOH
1	0.999719994722063	2.800052779370343e-04
0.6	0.599727019774915	2.729802250849289e-04
0.2	0.199746078634055	2.539213659450146e-04

To verify the proposed power management strategy' performance on battery life extension more clearly, another control strategy excluding the effect of SOH_{BT} are tested as a comparison. The fuzzy controllers with the same structures of controller 1 and 2 lacking the SOH input are used. All the other control inputs, outputs and their membership functions are the same as Figs. 7.10 and 7.11. Without considering SOH_{BT}, the logistical variables for SOH_{BT} are removed from the fuzzy rules in Tables 7.3 and 7.4. Moreover, all the rules not considering SOH_{BT} are designed as the same rules with SOH_{BT} = H because low SOH is not considered in the strategy here. Then, the UDDS cycle is also taken for both kinds of power management strategy considering or not considering Li-ion battery SOH. It is explicit that they have similar results for high SOH range. Thus, the comparison is done for $SOH_{BT}(0)$ = 0.7, 0.6 and 0.2. The SOH results after the UDDS driving cycle are shown in Table 7.6. It indicates that the power management strategy considering Li-ion battery SOH remains higher SOH_{BT} than the strategy not considering SOH_{BT} after the same EV driving actions, especially for the battery with low SOH. Not only supplying the EV required power, the fuzzy controllers considering SOH_{BT} also make Li-ion battery aging progress decelerated in EMS. It is verified that the proposed

power management strategy considering Li-ion battery SOH extends the battery service life by reducing Li-ion battery's aging rate during EV driving.

Table 7.6. SOH result comparison between control strategy with/without considering SOH.

Initial SOH	Resultant final SOH with fuzzy controller considering SOH	Resultant final SOH with fuzzy controller not considering SOH
0.7	0.699725867101298	0.699722525282266
0.6	0.599727019774915	0.599722896528944
0.2	0.199746078634055	0.199725069742181

7.6 Summary

In this chapter, the fuzzy logic power management strategy considering Li-ion battery aging mechanism is designed for EMS in EVs. With the EV power sources including Li-ion battery packs and ultracapacitors, the designed power management strategy distributes the EV required power to both sources. Besides achieving the function of supplying enough power to the traction system, the power management strategy also considers the power sources' operation conditions and performance. The two power sources' characteristics including dynamic behaviors, power density and energy density are considered in the control process.

As the Li-ion battery is the focal point in this study, its aging mechanism is also considered in the battery model. Then, a fuzzy logic controller scheme and corresponding control strategy are designed to do power management in EMS. Battery SOH is used in the fuzzy control strategy to decelerate the battery aging progress and extend battery life during EV driving. Comparing SOH results after the same driving cycle for batteries with different aging levels, the designed fuzzy control strategy decreases the battery aging rate in lower SOH condition. Another fuzzy controller scheme without considering battery SOH is also tested. It indicates that slower aging progress is achieved by the proposed control strategy compared with the strategy not considering SOH. In conclusion, the proposed power management strategy using fuzzy logic control achieves the functions of distributing power and extending Li-ion battery service life during EV driving. It is

verified that the proposed power management strategy is able to achieve good performance for EMS in EVs.

Chapter 8 Conclusions and Future Works

8.1 Conclusions

To improve electric vehicle (EV)'s operation performance and reliability, the research on developing an intelligent energy management system (EMS) in EVs is performed. Some relevant topics in EMS are researched by placing emphasis on the EV's major energy source, Li-ion batteries. Some improved results for these topics are presented in this thesis.

To provide an accurate model simulating Li-ion batteries in EMS, the topic of battery modeling is researched in this thesis. Series and parallel equivalent circuit models for Li-ion batteries are established from experiments and their results are compared. It is obtained that the series circuit model with two resistor-capacitor (RC) networks has the best accuracy and good simplicity. Based on the equivalent circuit model, a fuzzy logic model considering temperature effect is proposed. The method to extract and describe the model parameters is proposed. The neural network (NN) model trained by the extreme learning machine (ELM) algorithm is also proposed for a simple current pattern condition in experiment. Good accuracy and a simple training process are achieved by ELM compared with those of conventional NN method, radial basis function NN (RBF NN).

In EMS, it is important to master the Li-ion battery's operation status. Based on the proposed and existing models, Li-ion battery state of charge (SOC) estimation is executed in this thesis. The Kalman filter (KF) methods including extended Kalman filter (EKF), unscented Kalman filter (UKF), adaptive EKF (AEKF) and adaptive UKF (AUKF) are applied on the proposed ELM model to estimate battery SOC. The estimation results show that the AUKF algorithm obtains the best estimation accuracy and robustness for the ELM model. It also verifies that the ELM model is superior than the RBF NN model when doing SOC estimation. To overcome the KF method's defect and apply the proposed Li-ion battery SOC estimation methods in practice, the particle filter (PF) algorithm with no demand for system noise and model structure is applied on an accurate Li-ion battery equivalent model considering SOC's nonlinear effect on model parameters. It indicates that the improved PF method, unscented particle filter (UPF), provides better SOC estimation results although the computational load is heavy. Thus, to alleviate the

computational load during battery SOC estimation in applications, an adaptive observer using the sliding mode technique is proposed and applied on a simple Li-ion battery equivalent circuit model with the severe nonlinearity and modeling errors represented by model uncertainties. This combination of model and estimation algorithm is applicable. It is verified the adaptive observer has better SOC estimation results than the constant gain sliding mode observer. Then, Li-ion battery's SOC and state of health (SOH) are estimated simultaneously by the proposed adaptive observer based on the sliding mode scheme. The observer is intuitive to design and achieves good estimation performance. SOC and SOH estimation results with high accuracy and robustness are obtained by the proposed adaptive observer.

Then, Li-ion battery pack's performance is considered and the topic of cell equalization in battery string is researched. Considering the topology and control method's simplicity and system cost, the equalization method using switched capacitors is established and improved in this thesis. Using the modularization concept, a chain structure switched capacitor schematic is proposed with obviously improved equalizing speed and reduced switch voltage. Besides, a modularized double switched capacitor equalization schematic considering Li-ion battery SOC and SOH is proposed and good equalization performance and better reliability are achieved.

Finally, the power management strategy in EMS is designed using fuzzy logic control. The designed strategy determines the contributed power from the Li-ion battery pack and the ultracapacitor pack in EVs. The proposed power management strategy also supervises the power source's operation status of Li-ion battery SOC and ultracapacitor SOC. Compared with existing power management strategies in EMS, the proposed fuzzy control strategy in this thesis takes Li-ion battery SOH in consideration. The power management results show good performance on EV's various driving conditions. Moreover, the useful life for Li-ion battery is extended by reducing the aging speed for the battery in low SOH range.

8.2 Recommendations for Future Works

Based on the conclusions of this research, some more relevant topics in EV's EMS are recommended here as future works, including:

In this thesis, the Li-ion battery model considering temperature effect on model parameters is proposed. Some more details of the temperature effect and high current rate effect on Li-ion battery behavior will also be studied to make its model more comprehensive. For the fuzzy logic model considering different affecting factors, specific state and parameter estimation algorithms will be designed. Limited by experimental condition, only experiment data at room temperature are used to estimate and supervise Li-ion battery in this research. Li-ion battery SOC and SOH estimation considering different temperature conditions should be done for the battery model considering temperature, especially in high temperature range, whereas this topic still needs more research. On the other hand, battery overheating and cell thermal imbalance in Li-ion battery pack will bring damage to the batteries. Thus, suitable cooling strategies and cell thermal equalization schematics considering Li-ion battery inner thermal characteristics should also be realized in Li-ion battery packs in EVs.

As a random weight NN learning algorithm, the ELM algorithm's learning performance is satisfactory, but it is dependent on the randomly initialized input weights and biases. To improve the reliability of the ELM training process for Li-ion battery modeling is a meaningful topic to be studied. In addition, the performance of Li-ion battery online modeling using NNs still needs improvement in future works.

Battery aging mechanism is another important topic. The aging experiment for Li-ion battery is still needed to obtain the detailed effect caused by battery aging on battery model parameters including capacity and inner resistance. In this research, the battery aging function is represented by an assumed but meaningful factor when designing power management strategy. Actually, the function for the aging progress of Li-ion battery could be obtained by battery cycling experiments in long term. Different types of cycling processes should be tested to verify the affecting factors of Li-ion battery aging. With tested aging mechanism from battery cycling experiments, Li-ion battery SOH would have more accurate expression and some more SOH estimation methods based on the accurate expression could be proposed. Then, the power management strategy performance could be improved by considering real-world SOH expression and adding corresponding rules.

In future works, experimental verification should be conducted for the entire EMS. To implement EMS, some other necessary and interesting topics still need research. For example, the DC-DC converter topology and control algorithm need to be designed to adjust and maintain the power source's voltages in EV's power supply systems. The system efficiency, including power electronics part and mechanical traction part, should also be considered and improved when designing the entire system.

Author's Publications

1. J. Du, Z. Liu, and Y. Wang, "State of charge estimation for Li-ion battery based on model from extreme learning machine," *Control Engineering Practice*, vol. 26, pp. 11-19, 2014.

2. J. Du, Z. Liu, Y. Wang, and C. Wen, "An adaptive sliding mode observer for Li-ion battery SOC and SOH estimation," *Control Engineering Practice*, submitted.

3. J. Du, Z. Liu, Y. Wang, and C. Wen, "SOC estimation for Li-ion battery based on the nonlinear equivalent model using unscented particle filter," *Journal of Power Sources*, to be submitted.

4. J. Du, Z. Liu, Y. Wang, and C. Wen, "A fuzzy logic-based model for Li-ion battery with SOC and temperature effect," in *Control & Automation (ICCA), 11th IEEE International Conference on*, 2014, pp. 1333-1338.

5. J. Du, Y. Wang, and C. Wen, "Li-ion battery SOC estimation using particle filter based on an equivalent circuit model," in *Control and Automation (ICCA), 2013 10th IEEE International Conference on*, 2013, pp. 580-585

6. J. Du, Z. Liu, C. Chen, and Y. Wang, "Li-ion battery SOC estimation using EKF based on a model proposed by extreme learning machine," in *Industrial Electronics and Applications (ICIEA), 2012 7th IEEE Conference on*, 2012, pp. 1651-1656.

7. Z. Liu, J. Du, U. Stimming, and Y. Wang, "Adaptive passivity-based control for speed regulation of permanent magnet synchronous motor," in *Industrial Electronics and Applications (ICIEA), 2014 IEEE 9th Conference on*, 2014, pp. 645-649.

8. Z. Liu, J. Du, U. Stimming, and Y. Wang, "Adaptive observer design for the cell temperature estimation in battery packs in electric vehicles," in *Industrial Electronics and Applications (ICIEA), 2014 IEEE 9th Conference on*, 2014, pp. 348-353.

References

[1] J. Larminie and J. Lowry, *Electric vehicle technology explained*: John Wiley & Sons, 2004.

[2] W. Chen, W.-T. Chen, M. Saif, M.-F. Li, and H. Wu, "Simultaneous fault isolation and estimation of lithium-ion batteries via synthesized design of luenberger and learning observers," *Control Systems Technology, IEEE Transactions on,* vol. 22, pp. 290-298, 2014.

[3] H.-S. Park, C.-E. Kim, C.-H. Kim, G.-W. Moon, and J.-H. Lee, "A modularized charge equalizer for an HEV lithium-ion battery string," *Industrial Electronics, IEEE Transactions on,* vol. 56, pp. 1464-1476, 2009.

[4] M. Sitterly, L. Y. Wang, G. G. Yin, and C. Wang, "Enhanced identification of battery models for real-time battery management," *Sustainable Energy, IEEE Transactions on,* vol. 2, pp. 300-308, 2011.

[5] J. Alzieu, P. Gagnol, and H. Smimite, "Development of an on-board charge and discharge management system for electric-vehicle batteries," *Journal of Power Sources,* vol. 53, pp. 327-333, 1995.

[6] B. Schweighofer, K. M. Raab, and G. Brasseur, "Modeling of high power automotive batteries by the use of an automated test system," *Instrumentation and Measurement, IEEE Transactions on,* vol. 52, pp. 1087-1091, 2003.

[7] H. He, R. Xiong, H. Guo, and S. Li, "Comparison study on the battery models used for the energy management of batteries in electric vehicles," *Energy Conversion and Management,* vol. 64, pp. 113-121, 2012.

[8] K. A. Smith, C. D. Rahn, and C.-Y. Wang, "Control oriented 1D electrochemical model of lithium ion battery," *Energy Conversion and Management,* vol. 48, pp. 2565-2578, 2007.

[9] X. Hu, S. Li, and H. Peng, "A comparative study of equivalent circuit models for Li-ion batteries," *Journal of Power Sources,* vol. 198, pp. 359-367, 2012.

[10] K. A. Smith, C. D. Rahn, and C. Y. Wang, "Model-based electrochemical estimation and constraint management for pulse operation of lithium ion batteries," *Control Systems Technology, IEEE Transactions on,* vol. 18, pp. 654-663, 2010.

[11] P. Arora, M. Doyle, A. S. Gozdz, R. E. White, and J. Newman, "Comparison between computer simulations and experimental data for high-rate discharges of plastic lithium-ion batteries," *Journal of Power Sources,* vol. 88, pp. 219-231, 2000.

[12] P. M. Gomadam, J. W. Weidner, R. A. Dougal, and R. E. White, "Mathematical modeling of lithium-ion and nickel battery systems," *Journal of Power Sources,* vol. 110, pp. 267-284, 2002.

[13] N. A. Chaturvedi, R. Klein, J. Christensen, J. Ahmed, and A. Kojic, "Algorithms for advanced battery-management systems," *Control Systems Magazine, IEEE,* vol. 30, pp. 49-68, 2010.

[14] Y. Hu, S. Yurkovich, Y. Guezennec, and B. Yurkovich, "Electro-thermal battery model identification for automotive applications," *Journal of Power Sources,* vol. 196, pp. 449-457, 2011.

[15] G. L. Plett, "Extended Kalman filtering for battery management systems of LiPB-based HEV battery packs: Part 2. Modeling and identification," *Journal of Power Sources,* vol. 134, pp. 262-276, 2004.

[16] L. Gao, S. Liu, and R. A. Dougal, "Dynamic lithium-ion battery model for system simulation," *Components and Packaging Technologies, IEEE Transactions on,* vol. 25, pp. 495-505, 2002.

[17] M. Chen and G. A. Rincon-Mora, "Accurate electrical battery model capable of predicting runtime and IV performance," *Energy Conversion, IEEE Transactions on,* vol. 21, pp. 504-511, 2006.

[18] I.-S. Kim, "Nonlinear state of charge estimator for hybrid electric vehicle battery," *Power Electronics, IEEE Transactions on,* vol. 23, pp. 2027-2034, 2008.

[19] J. Kim, S. Lee, and B. Cho, "The state of charge estimation employing empirical parameters measurements for various temperatures," in *Power Electronics and Motion Control Conference, 2009. IPEMC'09. IEEE 6th International*, 2009, pp. 939-944.

[20] J. Gomez, R. Nelson, E. E. Kalu, M. H. Weatherspoon, and J. P. Zheng, "Equivalent circuit model parameters of a high-power Li-ion battery: thermal and state of charge effects," *Journal of Power Sources,* vol. 196, pp. 4826-4831, 2011.

[21] S. Cho, H. Jeong, C. Han, S. Jin, J. H. Lim, and J. Oh, "State-of-charge estimation for lithium-ion batteries under various operating conditions using an equivalent circuit model," *Computers & Chemical Engineering,* vol. 41, pp. 1-9, 2012.

[22] B. Sun and L. Wang, "The SOC estimation of NIMH battery pack for HEV based on BP neural network," in *Intelligent Systems and Applications, 2009. ISA 2009. International Workshop on*, 2009, pp. 1-4.

[23] Y. Morita, S. Yamamoto, S. H. Lee, and N. Mizuno, "On line detection of state of charge in lead acid battery using radial basis function neural network," *Asian Journal of Control,* vol. 8, pp. 268-273, 2006.

[24] Z. Liu, Y. Wang, J. Du, and C. Chen, "RBF network-aided adaptive unscented kalman filter for lithium-ion battery SOC estimation in electric vehicles," in *Industrial Electronics and Applications (ICIEA), 2012 7th IEEE Conference on*, 2012, pp. 1673-1677.

[25] M. Charkhgard and M. Farrokhi, "State-of-charge estimation for lithium-ion batteries using neural networks and EKF," *Industrial Electronics, IEEE Transactions on,* vol. 57, pp. 4178-4187, 2010.

[26] Y. Shen, "Adaptive online state-of-charge determination based on neuro-controller and neural network," *Energy Conversion and Management,* vol. 51, pp. 1093-1098, 2010.

[27] Y. Liu, K. Zhao, X. Huang, and F. Pei, "A new method based on RBFNN in SOC estimation of HEV battery," in *Control Conference (CCC), 2010 29th Chinese*, 2010, pp. 4923-4927.

[28] L. Xu, J. Wang, and Q. Chen, "Kalman filtering state of charge estimation for battery management system based on a stochastic fuzzy neural network battery model," *Energy Conversion and Management*, vol. 53, pp. 33-39, 2012.

[29] G.-B. Huang, Q.-Y. Zhu, and C.-K. Siew, "Extreme learning machine: theory and applications," *Neurocomputing*, vol. 70, pp. 489-501, 2006.

[30] G. L. Plett, "Extended Kalman filtering for battery management systems of LiPB-based HEV battery packs: Part 1. Background," *Journal of Power Sources*, vol. 134, pp. 252-261, 2004.

[31] S. Piller, M. Perrin, and A. Jossen, "Methods for state-of-charge determination and their applications," *Journal of Power Sources*, vol. 96, pp. 113-120, 2001.

[32] J. Lee, O. Nam, and B. Cho, "Li-ion battery SOC estimation method based on the reduced order extended Kalman filtering," *Journal of Power Sources*, vol. 174, pp. 9-15, 2007.

[33] M. Coleman, L. Chi Kwan, Z. Chunbo, and W. G. Hurley, "State-of-Charge Determination From EMF Voltage Estimation: Using Impedance, Terminal Voltage, and Current for Lead-Acid and Lithium-Ion Batteries," *Industrial Electronics, IEEE Transactions on*, vol. 54, pp. 2550-2557, 2007.

[34] D. Dinh Vinh, C. Forgez, K. El Kadri Benkara, and G. Friedrich, "Impedance Observer for a Li-Ion Battery Using Kalman Filter," *Vehicular Technology, IEEE Transactions on*, vol. 58, pp. 3930-3937, 2009.

[35] A. Zenati, P. Desprez, and H. Razik, "Estimation of the SOC and the SOH of li-ion batteries, by combining impedance measurements with the fuzzy logic inference," in *IECON 2010 - 36th Annual Conference on IEEE Industrial Electronics Society*, 2010, pp. 1773-1778.

[36] D. Simon, *Optimal state estimation: Kalman, H infinity, and nonlinear approaches*: John Wiley & Sons, 2006.

[37] H. He, R. Xiong, and H. Guo, "Online estimation of model parameters and state-of-charge of $LiFePO_4$ batteries in electric vehicles," *Applied Energy*, vol. 89, pp. 413-420, 2012.

[38] G. L. Plett, "Kalman-filter SOC estimation for LiPB HEV cells," in *Proceedings of the 19th International Battery, Hybrid and Fuel Cell Electric Vehicle Symposium & Exhibition (EVS19). Busan, Korea*, 2002, pp. 527-538.

[39] Z. Chen, Y. Fu, and C. C. Mi, "State of charge estimation of lithium-ion batteries in electric drive vehicles using extended Kalman filtering," *Vehicular Technology, IEEE Transactions on*, vol. 62, pp. 1020-1030, 2013.

[40] D. Lerro and Y. Bar-Shalom, "Tracking with debiased consistent converted measurements versus EKF," *Aerospace and Electronic Systems, IEEE Transactions on*, vol. 29, pp. 1015-1022, 1993.

[41] H. He, R. Xiong, X. Zhang, F. Sun, and J. Fan, "State-of-charge estimation of the lithium-ion battery using an adaptive extended Kalman filter based on an improved Thevenin model," *Vehicular Technology, IEEE Transactions on*, vol. 60, pp. 1461-1469, 2011.

[42] G. L. Plett, "Sigma-point Kalman filtering for battery management systems of LiPB-based HEV Battery packs: Part 2: Simultaneous state and parameter estimation," *Journal of Power Sources*, vol. 161, pp. 1369-1384, 2006.

[43] G. L. Plett, "Extended Kalman filtering for battery management systems of LiPB-based HEV battery packs: Part 3. State and parameter estimation," *Journal of Power sources*, vol. 134, pp. 277-292, 2004.

[44] C. Hu, B. D. Youn, and J. Chung, "A multiscale framework with extended Kalman filter for lithium-ion battery SOC and capacity estimation," *Applied Energy*, vol. 92, pp. 694-704, 2012.

[45] A. Vasebi, S. Bathaee, and M. Partovibakhsh, "Predicting state of charge of lead-acid batteries for hybrid electric vehicles by extended Kalman filter," *Energy Conversion and Management*, vol. 49, pp. 75-82, 2008.

[46] N. Watrin, R. Roche, H. Ostermann, B. Blunier, and A. Miraoui, "Multiphysical lithium-based battery model for use in state-of-charge determination," *Vehicular Technology, IEEE Transactions on*, vol. 61, pp. 3420-3429, 2012.

[47] C. Hametner and S. Jakubek, "State of charge estimation for Lithium Ion cells: Design of experiments, nonlinear identification and fuzzy observer design," *Journal of Power Sources,* vol. 238, pp. 413-421, 2013.

[48] M. Partovibakhsh and G. Liu, "Online estimation of model parameters and state-of-charge of Lithium-Ion battery using unscented Kalman Filter," in *American Control Conference (ACC), 2012*, 2012, pp. 3962-3967.

[49] J. Wang, J. Guo, and L. Ding, "An adaptive Kalman filtering based State of Charge combined estimator for electric vehicle battery pack," *Energy Conversion and Management,* vol. 50, pp. 3182-3186, 2009.

[50] F. Sun, X. Hu, Y. Zou, and S. Li, "Adaptive unscented Kalman filtering for state of charge estimation of a lithium-ion battery for electric vehicles," *Energy,* vol. 36, pp. 3531-3540, 2011.

[51] N. Boizot, E. Busvelle, J.-P. Gauthier, and J. Sachau, "Adaptive-gain extended kalman filter: Application to a series connected dc motor," in *Conference on Systems and Control, Marrakech, Morocco*, 2007, pp. 16-18.

[52] A. Mohamed and K. Schwarz, "Adaptive Kalman filtering for INS/GPS," *Journal of Geodesy,* vol. 73, pp. 193-203, 1999.

[53] K. Xiong, H. Zhang, and L. Liu, "Adaptive robust extended Kalman filter for nonlinear stochastic systems," *IET Control Theory & Applications,* vol. 2, pp. 239-250, 2008.

[54] X. Hu, F. Sun, and Y. Zou, "Estimation of state of charge of a lithium-ion battery pack for electric vehicles using an adaptive Luenberger observer," *Energies,* vol. 3, pp. 1586-1603, 2010.

[55] F. Zhang, G. Liu, L. Fang, and H. Wang, "Estimation of battery state of charge with observer: Applied to a robot for inspecting power transmission lines," *Industrial Electronics, IEEE Transactions on,* vol. 59, pp. 1086-1095, 2012.

[56] R. Van Der Merwe, A. Doucet, N. De Freitas, and E. Wan, "The unscented particle filter," in *NIPS*, 2000, pp. 584-590.

[57] M. Gao, Y. Liu, and Z. He, "Battery state of charge online estimation based on particle filter," in *Image and Signal Processing (CISP), 2011 4th International Congress on*, 2011, pp. 2233-2236.

[58] Y. He, X. Liu, C. Zhang, and Z. Chen, "A new model for State-of-Charge (SOC) estimation for high-power Li-ion batteries," *Applied Energy*, vol. 101, pp. 808-814, 2013.

[59] M. Gholizadeh and F. R. Salmasi, "Estimation of State-of-Charge, Unknown Nonlinearities, and State-of-Health of a Lithium-Ion Battery Based on a Comprehensive Unobservable Model," *Industrial Electronics, IEEE Transactions on*, vol. 61, pp. 1335-1344, 2014.

[60] X. Chen, W. Shen, Z. Cao, and A. Kapoor, "A novel approach for state of charge estimation based on adaptive switching gain sliding mode observer in electric vehicles," *Journal of Power Sources*, vol. 246, pp. 667-678, 2014.

[61] F. Zhang, G. Liu, and L. Fang, "A battery state of charge estimation method using sliding mode observer," in *Intelligent Control and Automation, 2008. WCICA 2008. 7th World Congress on*, 2008, pp. 989-994.

[62] I. Park and S. Kim, "A sliding mode observer design for fuel cell electric vehicles," *Journal of Power Electronics*, vol. 6, pp. 172-177, 2006.

[63] V. I. Utkin, *Sliding modes in control and optimization* vol. 116: Springer, 1992.

[64] S. Drakunov and V. Utkin, "Sliding mode observers. Tutorial," in *Decision and Control, 1995., Proceedings of the 34th IEEE Conference on*, 1995, pp. 3376-3378.

[65] J. Y. Hung, W. Gao, and J. C. Hung, "Variable structure control: a survey," *Industrial Electronics, IEEE Transactions on*, vol. 40, pp. 2-22, 1993.

[66] S. V. Drakunov, "Sliding-mode observers based on equivalent control method," in *Proceedings of the 31st IEEE Conference on Decision and Control*, 1992, pp. 2368-2369.

[67] X. Chen and H. Kano, "State observer for a class of nonlinear systems and its application to machine vision," *Automatic Control, IEEE Transactions on,* vol. 49, pp. 2085-2091, 2004.

[68] Y. Zhang, C.-Y. Wang, and X. Tang, "Cycling degradation of an automotive $LiFePO_4$ lithium-ion battery," *Journal of Power Sources,* vol. 196, pp. 1513-1520, 2011.

[69] J. Wang, P. Liu, J. Hicks-Garner, E. Sherman, S. Soukiazian, M. Verbrugge, *et al.*, "Cycle-life model for graphite-$LiFePO_4$ cells," *Journal of Power Sources,* vol. 196, pp. 3942-3948, 2011.

[70] I. Bloom, B. Cole, J. Sohn, S. Jones, E. Polzin, V. Battaglia, *et al.*, "An accelerated calendar and cycle life study of Li-ion cells," *Journal of Power Sources,* vol. 101, pp. 238-247, 2001.

[71] B. Y. Liaw, R. G. Jungst, G. Nagasubramanian, H. L. Case, and D. H. Doughty, "Modeling capacity fade in lithium-ion cells," *Journal of power sources,* vol. 140, pp. 157-161, 2005.

[72] R. Spotnitz, "Simulation of capacity fade in lithium-ion batteries," *Journal of Power Sources,* vol. 113, pp. 72-80, 2003.

[73] P. Ramadass, B. Haran, R. White, and B. N. Popov, "Mathematical modeling of the capacity fade of Li-ion cells," *Journal of Power Sources,* vol. 123, pp. 230-240, 2003.

[74] A. P. Schmidt, M. Bitzer, Á. W. Imre, and L. Guzzella, "Model-based distinction and quantification of capacity loss and rate capability fade in Li-ion batteries," *Journal of Power Sources,* vol. 195, pp. 7634-7638, 2010.

[75] L. Serrao, S. Onori, A. Sciarretta, Y. Guezennec, and G. Rizzoni, "Optimal energy management of hybrid electric vehicles including battery aging," in *American Control Conference (ACC), 2011*, 2011, pp. 2125-2130.

[76] S. Ebbesen, P. Elbert, and L. Guzzella, "Battery state-of-health perceptive energy management for hybrid electric vehicles," *Vehicular Technology, IEEE Transactions on,* vol. 61, pp. 2893-2900, 2012.

[77] A. Di Filippi, S. Stockar, S. Onori, M. Canova, and Y. Guezennec, "Model-based life estimation of Li-ion batteries in PHEVs using large scale vehicle simulations: An introductory study," in *Vehicle Power and Propulsion Conference (VPPC), 2010 IEEE*, 2010, pp. 1-6.

[78] V. Marano, S. Onori, Y. Guezennec, G. Rizzoni, and N. Madella, "Lithium-ion batteries life estimation for plug-in hybrid electric vehicles," in *Vehicle Power and Propulsion Conference, 2009. VPPC'09. IEEE*, 2009, pp. 536-543.

[79] Y.-H. Chiang, W.-Y. Sean, and J.-C. Ke, "Online estimation of internal resistance and open-circuit voltage of lithium-ion batteries in electric vehicles," *Journal of Power Sources*, vol. 196, pp. 3921-3932, 2011.

[80] J. Kim, S. Lee, and B. Cho, "Complementary cooperation algorithm based on DEKF combined with pattern recognition for SOC/capacity estimation and SOH prediction," *Power Electronics, IEEE Transactions on*, vol. 27, pp. 436-451, 2012.

[81] J. Remmlinger, M. Buchholz, M. Meiler, P. Bernreuter, and K. Dietmayer, "State-of-health monitoring of lithium-ion batteries in electric vehicles by on-board internal resistance estimation," *Journal of Power Sources*, vol. 196, pp. 5357-5363, 2011.

[82] Y.-H. Chiang and W.-Y. Sean, "Dynamical estimation of state-of-health of batteries by using adaptive observer," in *Power Electronics and Intelligent Transportation System (PEITS), 2009 2nd International Conference on*, 2009, pp. 110-115.

[83] G. K. Prasad and C. D. Rahn, "Model based identification of aging parameters in lithium ion batteries," *Journal of Power Sources*, vol. 232, pp. 79-85, 2013.

[84] A. J. Salkind, C. Fennie, P. Singh, T. Atwater, and D. E. Reisner, "Determination of state-of-charge and state-of-health of batteries by fuzzy logic methodology," *Journal of Power Sources*, vol. 80, pp. 293-300, 1999.

[85] A. Zenati, P. Desprez, and H. Razik, "Estimation of the SOC and the SOH of Li-ion batteries, by combining impedance measurements with the fuzzy logic

inference," in *IECON 2010-36th Annual Conference on IEEE Industrial Electronics Society*, 2010, pp. 1773-1778.

[86] H.-T. Lin, T.-J. Liang, and S.-M. Chen, "Estimation of battery state of health using probabilistic neural network," *Industrial Informatics, IEEE Transactions on,* vol. 9, pp. 679-685, 2013.

[87] K. S. Ng, C. S. Moo, Y. P. Chen, and Y. C. Hsieh, "Enhanced coulomb counting method for estimating state-of-charge and state-of-health of lithium-ion batteries," *Applied Energy,* vol. 86, pp. 1506-1511, 2009.

[88] G. L. Plett, "Dual and joint EKF for simultaneous SOC and SOH estimation," in *CD-ROM Proceedings of the 21st Electric Vehicle Symposium (EVS21),(Monaco: April 2005)*, 2005.

[89] S. Lee, J. Kim, J. Lee, and B. Cho, "State-of-charge and capacity estimation of lithium-ion battery using a new open-circuit voltage versus state-of-charge," *Journal of Power Sources,* vol. 185, pp. 1367-1373, 2008.

[90] D. Andre, C. Appel, T. Soczka-Guth, and D. U. Sauer, "Advanced mathematical methods of SOC and SOH estimation for lithium-ion batteries," *Journal of Power Sources,* vol. 224, pp. 20-27, 2013.

[91] I.-S. Kim, "A technique for estimating the state of health of lithium batteries through a dual-sliding-mode observer," *Power Electronics, IEEE Transactions on,* vol. 25, pp. 1013-1022, 2010.

[92] M. Daowd, N. Omar, P. Van Den Bossche, and J. Van Mierlo, "Passive and active battery balancing comparison based on MATLAB simulation," in *Vehicle Power and Propulsion Conference (VPPC), 2011 IEEE*, 2011, pp. 1-7.

[93] Y.-S. Lee and M.-W. Cheng, "Intelligent control battery equalization for series connected lithium-ion battery strings," *Industrial Electronics, IEEE Transactions on,* vol. 52, pp. 1297-1307, 2005.

[94] S. W. Moore and P. J. Schneider, "A review of cell equalization methods for lithium ion and lithium polymer battery systems," SAE Technical Paper, 2001.

[95] X. Wei and B. Zhu, "The research of vehicle power li-ion battery pack balancing method," in *2009 9th International Conference on Electronic Measurement&Instruments*, 2009.

[96] D. C. Hopkins, C. R. Mosling, and S. T. Hung, "Dynamic equalization during charging of serial energy storage elements," *Industry Applications, IEEE Transactions on,* vol. 29, pp. 363-368, 1993.

[97] K. Nishijima, H. Sakamoto, and K. Harada, "A PWM controlled simple and high performance battery balancing system," in *Power Electronics Specialists Conference, 2000. PESC 00. 2000 IEEE 31st Annual*, 2000, pp. 517-520.

[98] T. H. Phung, J.-C. Crebier, A. Chureau, A. Collet, and T. Van Nguyen, "Optimized structure for next-to-next balancing of series-connected lithium-ion cells," in *Applied Power Electronics Conference and Exposition (APEC), 2011 Twenty-Sixth Annual IEEE*, 2011, pp. 1374-1381.

[99] J.-W. Shin, G.-S. Seo, C.-Y. Chun, and B.-H. Cho, "Selective flyback balancing circuit with improved balancing speed for series connected lithium-ion batteries," in *Power Electronics Conference (IPEC), 2010 International*, 2010, pp. 1180-1184.

[100] N. H. Kutkut, H. L. Wiegman, D. M. Divan, and D. W. Novotny, "Charge equalization for an electric vehicle battery system," *Aerospace and Electronic Systems, IEEE Transactions on,* vol. 34, pp. 235-246, 1998.

[101] C. Moo, Y. Hsieh, I. Tsai, and J. Cheng, "Dynamic charge equalisation for series-connected batteries," *IEE Proceedings-Electric Power Applications,* vol. 150, pp. 501-505, 2003.

[102] M. Uno and K. Tanaka, "Single-switch cell voltage equalizer using multistacked buck-boost converters operating in discontinuous conduction mode for series-connected energy storage cells," *Vehicular Technology, IEEE Transactions on,* vol. 60, pp. 3635-3645, 2011.

[103] C. Pascual and P. T. Krein, "Switched capacitor system for automatic series battery equalization," in *Applied Power Electronics Conference and Exposition,*

1997. APEC'97 Conference Proceedings 1997., Twelfth Annual, 1997, pp. 848-854.

[104] M.-Y. Kim, C.-H. Kim, K. Jun-Ho, and G.-W. Moon, "A chain structure of switched capacitor for improved cell balancing speed of lithium-ion batteries," *Industrial Electronics, IEEE Transactions on,* vol. 61, pp. 3989-3999, 2014.

[105] A. C. Baughman and M. Ferdowsi, "Double-tiered switched-capacitor battery charge equalization technique," *Industrial Electronics, IEEE Transactions on,* vol. 55, pp. 2277-2285, 2008.

[106] R. Fukui and H. Koizumi, "Double-tiered switched capacitor battery charge equalizer with chain structure," in *Industrial Electronics Society, IECON 2013-39th Annual Conference of the IEEE,* 2013, pp. 6715-6720.

[107] C. Speltino, A. Stefanopoulou, and G. Fiengo, "Cell equalization in battery stacks through state of charge estimation polling," in *American Control Conference (ACC), 2010*, 2010, pp. 5050-5055.

[108] H.-S. Park, C.-H. Kim, K.-B. Park, G.-W. Moon, and J.-H. Lee, "Design of a charge equalizer based on battery modularization," *Vehicular Technology, IEEE Transactions on*, vol. 58, pp. 3216-3223, 2009.

[109] C.-H. Kim, M.-Y. Kim, and G.-W. Moon, "A modularized charge equalizer using a battery monitoring IC for series-connected Li-ion battery strings in electric vehicles," *Power Electronics, IEEE Transactions on*, vol. 28, pp. 3779-3787, 2013.

[110] S. Teleke, M. E. Baran, S. Bhattacharya, and A. Q. Huang, "Optimal control of battery energy storage for wind farm dispatching," *Energy Conversion, IEEE Transactions on*, vol. 25, pp. 787-794, 2010.

[111] H. Chaoui and P. Sicard, "Fuzzy logic based supervisory energy management for multisource electric vehicles," in *Vehicle Power and Propulsion Conference (VPPC), 2011 IEEE*, 2011, pp. 1-5.

[112] A. A. Ferreira, J. A. Pomilio, G. Spiazzi, and L. de Araujo Silva, "Energy management fuzzy logic supervisory for electric vehicle power supplies system," *Power Electronics, IEEE Transactions on*, vol. 23, pp. 107-115, 2008.

[113] A. Melero-Pérez, W. Gao, and J. J. Fernández-Lozano, "Fuzzy logic energy management strategy for fuel cell/ultracapacitor/battery hybrid vehicle with multiple-input DC/DC converter," in *Vehicle Power and Propulsion Conference, 2009. VPPC'09. IEEE*, 2009, pp. 199-206.

[114] F. Xue, H. B. Gooi, and S. X. Chen, "Hybrid energy storage with multimode fuzzy power allocator for PV systems," *Sustainable Energy, IEEE Transactions on,* vol. 5, pp. 389-397, 2014.

[115] M. Einhorn, F. V. Conte, C. Kral, and J. Fleig, "Comparison, selection, and parameterization of electrical battery models for automotive applications," *Power Electronics, IEEE Transactions on,* vol. 28, pp. 1429-1437, 2013.

[116] M. Knauff, C. J. Dafis, D. Niebur, H. G. Kwatny, and C. Nwankpa, "Simulink model for hybrid power system test-bed," in *Electric Ship Technologies Symposium, 2007. ESTS'07. IEEE,* 2007, pp. 421-427.

[117] H. Zhang and D. Liu, *Fuzzy modeling and fuzzy control*: Springer, 2006.

[118] N.-Y. Liang, G.-B. Huang, P. Saratchandran, and N. Sundararajan, "A fast and accurate online sequential learning algorithm for feedforward networks," *Neural Networks, IEEE Transactions on,* vol. 17, pp. 1411-1423, 2006.

[119] G.-B. Huang, L. Chen, and C.-K. Siew, "Universal approximation using incremental constructive feedforward networks with random hidden nodes," *Neural Networks, IEEE Transactions on,* vol. 17, pp. 879-892, 2006.

[120] G.-B. Huang, "Learning capability and storage capacity of two-hidden-layer feedforward networks," *Neural Networks, IEEE Transactions on,* vol. 14, pp. 274-281, 2003.

[121] G.-B. Huang, Q.-Y. Zhu, K. Mao, C.-K. Siew, P. Saratchandran, and N. Sundararajan, "Can threshold networks be trained directly?," *Circuits and Systems II: Express Briefs, IEEE Transactions on,* vol. 53, pp. 187-191, 2006.

[122] C. R. Rao and S. K. Mitra, *Generalized inverse of matrices and its applications* vol. 7: Wiley New York, 1971.

[123] R. E. Kalman, "A new approach to linear filtering and prediction problems," *Journal of basic Engineering,* vol. 82, pp. 35-45, 1960.

[124] G. Welch and G. Bishop. (1995, An introduction to the Kalman filter. Available: http://www.cs.unc.edu/~welch/media/pdf/kalman_intro.pdf

[125] S. J. Julier and J. K. Uhlmann, "Unscented filtering and nonlinear estimation," *Proceedings of the IEEE,* vol. 92, pp. 401-422, 2004.

[126] S. Julier, J. Uhlmann, and H. F. Durrant-Whyte, "A new method for the nonlinear transformation of means and covariances in filters and estimators," *Automatic Control, IEEE Transactions on,* vol. 45, pp. 477-482, 2000.

[127] S. J. Julier and J. K. Uhlmann, "A general method for approximating nonlinear transformations of probability distributions," Technical report, Robotics Research Group, Department of Engineering Science, University of Oxford, 1996.

[128] H. G. de Marina, F. J. Pereda, J. M. Giron-Sierra, and F. Espinosa, "UAV Attitude Estimation Using Unscented Kalman Filter and TRIAD," *Industrial Electronics, IEEE Transactions on,* vol. 59, pp. 4465-4474, 2012.

[129] R. Mehra, "On the identification of variances and adaptive Kalman filtering," *Automatic Control, IEEE Transactions on,* vol. 15, pp. 175-184, 1970.

[130] V. Fathabadi, M. Shahbazian, K. Salahshour, and L. Jargani, "Comparison of adaptive Kalman filter methods in state estimation of a nonlinear system using asynchronous measurements," in *Proc., World Congress on Engineering and Computer Science,* 2009, pp. 1-8.

[131] P. S. Maybeck, *Stochastic models, estimation, and control* vol. 3: Academic press, 1982.

[132] A. Almagbile, J. Wang, and W. Ding, "Evaluating the Performances of Adaptive Kalman Filter Methods in GPS/INS Integration," *Journal of Global Positioning Systems,* vol. 9, pp. 33-40, 2010.

[133] M. S. Arulampalam, S. Maskell, N. Gordon, and T. Clapp, "A tutorial on particle filters for online nonlinear/non-Gaussian Bayesian tracking," *Signal Processing, IEEE Transactions on*, vol. 50, pp. 174-188, 2002.

[134] H. Dai, X. Wei, and Z. Sun, "Online SOC estimation of high-power lithium-ion batteries used on HEVs," in *Vehicular Electronics and Safety, 2006. ICVES 2006. IEEE International Conference on*, 2006, pp. 342-347.

[135] X. Chen and H. Kano, "A new state observer for perspective systems," *Automatic Control, IEEE Transactions on*, vol. 47, pp. 658-663, 2002.

[136] C. Edwards and S. Spurgeon, *Sliding mode control: theory and applications*: CRC Press, 1998.

[137] J. Cao, N. Schofield, and A. Emadi, "Battery balancing methods: A comprehensive review," in *Vehicle Power and Propulsion Conference, 2008. VPPC'08. IEEE*, 2008, pp. 1-6.

[138] L. Solero, A. Lidozzi, and J. A. Pomilio, "Design of multiple-input power converter for hybrid vehicles," *Power Electronics, IEEE Transactions on*, vol. 20, pp. 1007-1016, 2005.

[139] Z. Liu, Y. Wang, and J. Du, "Fuzzy model predictive control of a permanent magnet synchronous motor in electric vehicles," in *Control and Automation (ICCA), 2013 10th IEEE International Conference on*, 2013, pp. 604-608.

[140] S. Soylu, "Electric Vehicles–Modelling and Simulations," *InTech Europe, Rijeka, Croatia*, 2011.

[141] S. J. Moura, H. K. Fathy, D. S. Callaway, and J. L. Stein, "A stochastic optimal control approach for power management in plug-in hybrid electric vehicles," *Control Systems Technology, IEEE Transactions on*, vol. 19, pp. 545-555, 2011.

[142] G. Ripaccioli, D. Bernardini, S. Di Cairano, A. Bemporad, and I. Kolmanovsky, "A stochastic model predictive control approach for series hybrid electric vehicle power management," in *American Control Conference (ACC), 2010*, 2010, pp. 5844-5849.

[143] A. Poursamad and M. Montazeri, "Design of genetic-fuzzy control strategy for parallel hybrid electric vehicles," *Control Engineering Practice*, vol. 16, pp. 861-873, 2008.

[144] L. Serrao, S. Onori, G. Rizzoni, and Y. Guezennec, "A novel model-based algorithm for battery prognosis," in *Proceedings of the Seventh IFAC Symposium on Fault Detection, Supervision and Safety of Technical Processes (SAFEPROCESS 09)*, 2009.

[145] K. Smith, G. Kim, and A. Pesaran, "Modeling of nonuniform degradation in large-format li-ion batteries," in *Advanced Automotive Battery and EC Capacitor Conference*, 2009.

[146] S. Bashash, S. J. Moura, J. C. Forman, and H. K. Fathy, "Plug-in hybrid electric vehicle charge pattern optimization for energy cost and battery longevity," *Journal of Power Sources*, vol. 196, pp. 541-549, 2011.

[147] D.-J. Jwo and S.-H. Wang, "Adaptive fuzzy strong tracking extended Kalman filtering for GPS navigation," *Sensors Journal, IEEE*, vol. 7, pp. 778-789, 2007.